Surface Plasmon Polariton Guiding along Nanostructured Surfaces

Radko, Ilya

Publication date:
2009

Document Version
Publisher's PDF, also known as Version of record

Surface Plasmon Polariton Guiding along Nanostructured Surfaces

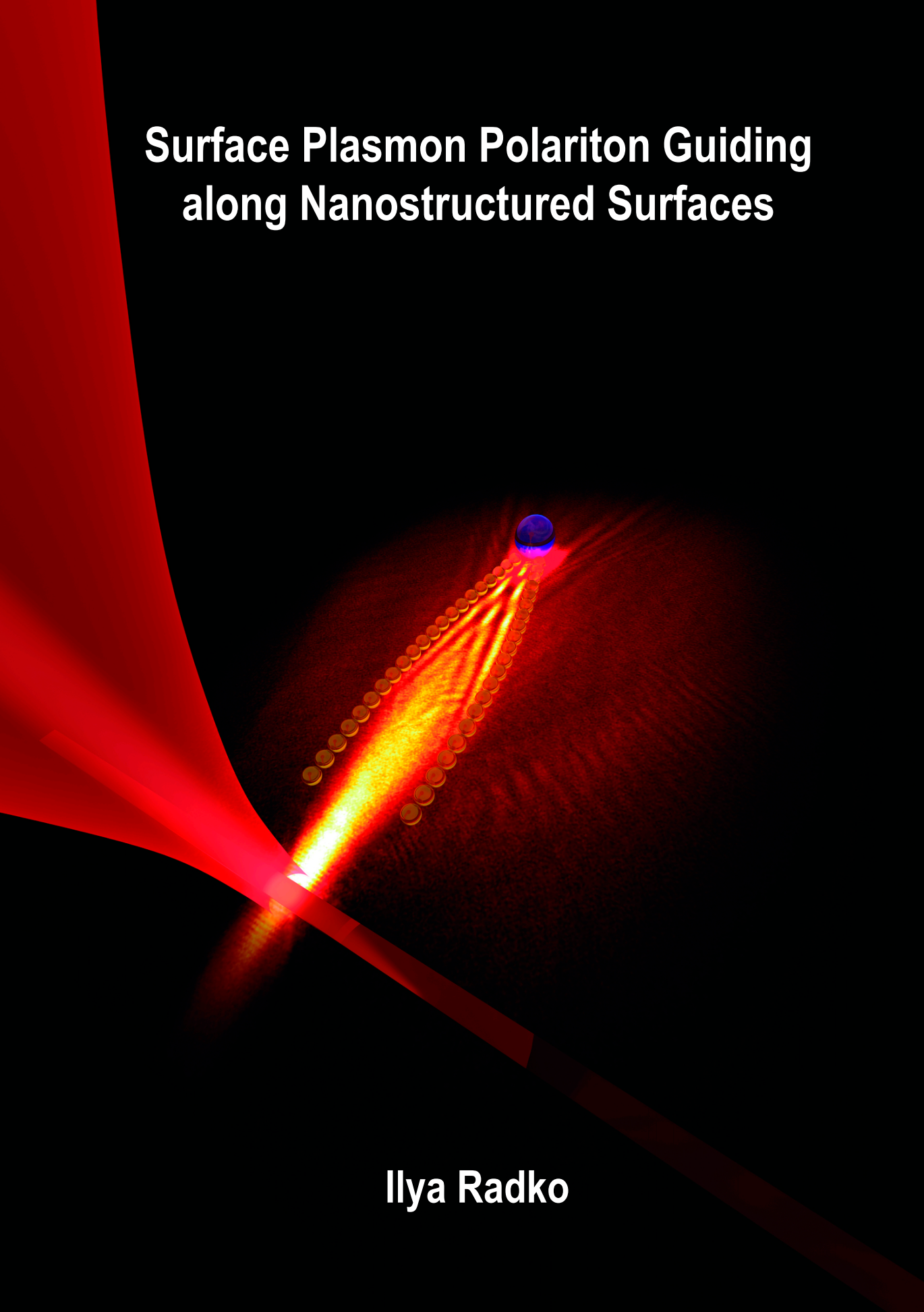

Ilya Radko

Ilya Radko

Surface Plasmon Polariton Guiding along Nanostructured Surfaces

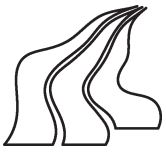

Department of Physics and Nanotechnology
Aalborg University, Denmark

Surface plasmon polariton guiding along
nanostructured surfaces

Overflade plasmon polariton styring langs
nanostrukturede overflader

Published and distributed by
Department of Physics and Nanotechnology, Aalborg University
Skjernvej 4A, DK–9220 Aalborg Øst.
Phone +45 99 40 92 15. Fax +45 98 15 65 02.

Typeset in LaTeX2$_\varepsilon$ by the author.
3D modelling of the cover image by Diana Radko.
Printed in Denmark by Syddansk Universitet Trykkeri.

ISBN 978-87-89195-18-6

Acronyms

List of used acronyms

2D:	Two-dimensional
BG:	Band gap
CCD:	Charge-coupled device
EBL:	Electron-beam lithography
ERI:	Effective refractive index
FT:	Fourier transform
FWHM:	Full width at half maximum
LR:	Leakage radiation
LRM:	Leakage-radiation microscopy/microscope
NA:	Numerical aperture
PMT:	Photomultiplier tube
SEM:	Scanning electron microscopy/microscope
SNOM:	Scanning near-field optical microscopy/microscope
SNR:	Signal-to-noise ratio
SP/SPP:	Surface plasmon/Surface plasmon polariton
SPBG:	Surface-plasmon band gap
TEM:	Transverse-electromagnetic
TF:	Transfer function

Preface

This PhD thesis is based on results obtained during my PhD study in a three-years period from July 2005 to June 2008 at the Department of Physics and Nanotechnology, Aalborg University, Denmark, under the supervision of Professor, Dr. Scient. Sergey I. Bozhevolnyi. The thesis has been submitted to the Faculty of Engineering and Science at Aalborg University in 2009.

Outline

Part I of this thesis presents an introduction to experimental techniques which I exploited in my PhD project. First chapter gives a motivation for investigation of surface plasmons (SPs), while the further two chapters introduce scanning near-field optical microscopy and leakage-radiation microscopy. The basic concepts, possibilities and limitations of the techniques, as well as the experimental setups for them are discussed.

Part II is a compilation of author's papers most relevant to the topic of the PhD thesis. Chapter 1 considers a possibility to guide SPs along channels in adiabatically rotated nanostructured areas exhibiting band-gap effect, whereas chapter 3 deals with SP manipulation and waveguiding using periodic nanostructures on the long-wavelength side of the band gap. The latter structures are shown to refract SP waves allowing hereby simple design of plasmonic lenses, prisms and waveguides. In chapter 2, parabolic nanoparticle chains are exploited to focus SP beams. Finally, in the following chapters, various possibilities to locally excite SPs are considered. Compact unidirectional nano-slit SP couplers are investigated in chapter 4. A possibility to simultaneously excite and focus SP beams is demonstrated. The goal of most efficient local light-plasmon conversion on periodic sets of metal ridges is pursued in chapters 5 and 6. While the former deals with a thorough investigation of different geometries and wavelength dependence of conversion efficiency, the latter describes a particular very

efficient configuration and shows that to be useful for applications involving field enhancement effect, such as surface enhanced Raman spectroscopy.

The bibliography, containing all cited literature and a list of author's publications and presentations, is found in the last part of the thesis.

Acknowledgments

While I was working on my PhD project, I received help and support from numerous people and had a pleasure to collaborate with good specialists in various subjects of nanotechnology. I would like to deeply thank my advisor Prof. Sergey I. Bozhevolnyi for his excellent guidance and for giving me an opportunity to participate in fascinating research. Being always full of bright ideas, he wisely supervised me so that I never had a problem of getting stuck without knowing where to move next. Now I understand how important it was. Also, I am very grateful to Dr. Alexandra Boltasseva (Purdue University, USA), a recognized expert in nanofabrication techniques, collaboration with whom was very fruitful and led to a number of results constituting the most part of this thesis. I would like to acknowledge the support with numerical data and valuable discussion of my experimental results with theoreticians Dr. Niels Gregersen (Danish Technical University), Dr. Thomas Søndergaard (Aalborg University, Denmark) and Dr. Andrey B. Evlyukhin (Kama State University, Russia). I also grateful to Prof. Luis Martín-Moreno (University of Zaragoza, Spain) for suggesting a beautiful idea of nano-slit surface plasmon excitation and Dr. José Dintinger (University of Louis Pasteur, France) who fabricated good-quality samples for this experiment to be possible. Not least important was the help of Dr. Andrey L. Stepanov who advised me during the construction of the leakage-radiation microscopy setup.

My close colleagues in Aalborg University helped me a lot in my work on this project. Thus I would like to thank Carsten Marquart who first introduced me to the area of surface plasmons and showed some basic techniques. I am grateful to Dr. Jonas Beermann who was always open for help and discussions. And most of all I am indebted to Dr. Valentyn S. Volkov, a near-field microscopy expert. Not only had he taught me how to work in optics laboratory. Having creative engineering thinking he gave me numerous valuable advices in constructing my own experimental setups and still remains the number one person to discuss experimental issues.

Finally, I thank my sister Diana for her supporting me at a distance during the whole time I have been staying in Denmark.

Odense, Denmark, 2009 **Ilya Radko**

Contents

Part I

Introduction

Chapter 1

A new technology

1.1 Nanotechnology

Manufactured products are made from atoms. The properties of those products depend on how those atoms are arranged. If we rearrange the atoms in coal we can make diamond. If we rearrange the atoms in sand (and add a few other trace elements) we can make computer chips. The control of matter at the length scale of 100 nm or less is the theme of *nanotechnology*.

Nanotechnology is a highly diverse and multidisciplinary field, ranging from novel extensions of conventional device physics, to completely new approaches based upon molecular self-assembly, to developing new materials with dimensions on the nanoscale, even to speculation on whether we can directly control matter on the atomic scale. The conceptual origin of nanotechnology is considered to be in "There's plenty of room at the bottom," a talk given by Richard Feynman at an American Physical Society meeting at Caltech on December 29, 1959 [1], though, the term itself was first defined by Norio Taniguchi of the Tokyo Science University in 1974 [2]. Feynman described a process by which the ability to manipulate individual atoms and molecules might be developed, using one set of precise tools to build and operate another proportionally smaller set, so on down to the needed scale. It was a timely talk, because the technology had already reached the level of manipulation of structures being as small as tens of microns in a reliable, reproducible way, and there was an observable potential for decreasing the length scale further. Therefore it is not a surprise that approximately at the same time a trend in the development of computer hardware has been formulated by Intel co-founder Gordon Moore [3]. Now known as Moore's law, it states that the number of transistors that can be inexpensively placed on an integrated circuit is increasing exponentially, doubling approximately every two years. Since that time the trend has continued for almost half a century and is not expected to stop for at least 10–15 years [4].

A global race to shrink physical dimensions and manufacture ever more complex integrated circuits has been forced appreciably by the paper of IBM researchers [5] where the authors discussed scaling principles of integrated circuits. They noted that as the horizontal dimensions of a transistor were scaled by a factor, speed improved by that same factor. This was the first attempt to relate a geometry shrink to the resulting power reduction and performance improvement and gave Gordon Moore's "law" a scientific foundation. The reason for the increased speed is the characteristic delay $\tau \sim RC$ associated with an element having resistance R and capacitance C. While capacitance C scales together with the size, in transistors, resistance R, rather than scaling inversely with the size (as it does for wires), stays roughly constant. So the RC delay for transistors is diminishing with miniaturization, improving the performance. Interestingly, the same year (1974) Intel designed an early microprocessor 8080, which was manufactured in a process using a minimum feature size of 6 μm, and by the present time (2009) the smallest feature size in the latest Intel's microprocessor, codenamed Westmere, is 32 nm.

Despite an increased operation speed of logical elements in a shrunk circuit, interconnects between them start to influence substantially the overall performance. Not only the resistance of interconnects is growing now, but also their mutual capacitance due to the dense packing of wires. Moreover, there are fundamental factors that will limit the development of silicon technology in the near future with the most important being electron thermal energy, tunneling leakage through gate oxide, and 2D electrostatic scale length [6–8]. According to the 2007 edition of International Technology Roadmap for Semiconductors [9], this near future will happen by the beginning of 2020th, when the transistors cannot be scaled further below the size achievable at 16-nm technological process due to quantum tunneling, regardless of the materials used [10].

Part of the upcoming problems, particularly with interconnects at increased bandwidths, can be solved by *integrated optics* — now almost a 40-years-old branch of optics whose beginning is associated with the Bell System Technical Journal's issue of 1969 where S. E. Miller introduced the basic ideas of integrated optics [11]. Light has several advantages over the electron [12]. The bandwidth of dielectric materials, such as optical fibers, is typically of the order of terahertz (the so-called dense wavelength division multiplexing allows for 160 channels of 10 Gbit/s each separated by an interval of 0.2 nm [13]) while that of copper-wire electronic interconnects is only (at best) a gigahertz. Furthermore, photons are not as strongly interacting as electrons, which helps reduce energy losses. A large number of components has been developed for the sake of realization of optical switching networks among which are suitable light sources, optical couplers, transmitters and receivers, optical filters, circulators, add-drop multiplexers and so on [14]. However, packet switches and routers in today's IP networks (even those connected with optical fibers) are sophisticated *electronic* systems, which rely heavily on advanced electronic buffering, fast switching, and powerful pro-

cessing technologies. Major obstacles for the all-optical switching have been the lack of a suitable optical memory technology and the need for reconfigurable cross-connects that can be switched in around 1 ns or less and that can accommodate the large number of ports (hundreds to thousands) required in practical applications [15]. In other words, integrated optics lacks for *compact* active components with the main reason for that being the diffraction of light, which imposes a natural limitation onto the miniaturization of optical components.

At the same time, the use of integrated optics merely at interconnects between active (electronic) components is cumbersome due to inevitable numerous optical-to-electronic and electronic-to-optical conversions. In this context, *plasmonics* is an exciting new technology that can bridge micro- or nano-electronics and integrated optics. By exploiting the unique optical properties of metallic nanostructures, it enables routing and manipulation of light at the nanoscale [16] still keeping the bandwidth at the level inherent to conventional optics.

1.2 Surface plasmons

Surface plasmon polaritons, or surface plasmons (SPs) for breviety, are electromagnetic modes bound to a metal-dielectric interface, comprising an electromagnetic field in dielectric — primarily transverse — coupled to coherent surface oscillations of free electrons in metal driving a primarily longitudinal electromagnetic field (Fig. 1.1). The existence of electromagnetic surface modes associated with the coherent electron oscillations at a metal surface has been demonstrated long time ago using electron energy-loss spectroscopy on metal films [17, 18]. However, it was not until the last decade that the interest to SPs greatly increased [19, 20] due to the development of nanofabrication techniques such as electron-beam lithography (EBL), ion-beam milling and self-assembly, together with modern nanocharacterization techniques such as dark-field and near-field optical microscopies and the emergence of quantitative electromagnetic simulation tools.

There is a variety of techniques to excite SPs, for instance, using an electric current [21, 22] or thermal excitation [23], but the most widely used ones are based on a direct coupling of propagating electromagnetic waves into SP modes using various configurations and geometries for achieving the phase-matching between the corresponding fields [24]. For the long-wavelength part of the visible spectrum and the infrared, SPs are quite close to the light line, i.e., the SP wavelength is close to that of propagating (in dielectric) radiation. However, modifying the geometry of a metal surface one can slow down the corresponding SP mode and hence decrease its wavelength. This can be done by placing two or more metal-dielectric interfaces close to each other, which introduces the coupling between the SPs of individual interfaces and modifies the appropriate resulting SP mode [25–27]. Once achieved, a large difference in the wavelengths of SP and radiation

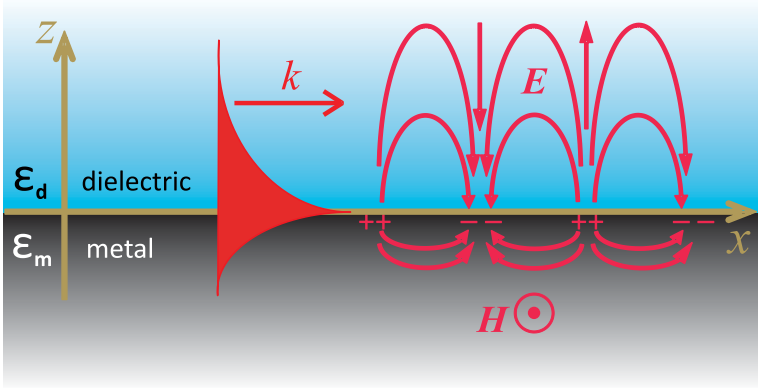

Figure 1.1: A SP wave at a metal-dielectric interface. The wave is transverse-magnetic by its nature. Due to the typical values of dielectric constants, the electric field in dielectric is primarily transverse, while that in metal is primarily longitudinal. The electromagnetic field intensity reaches its maximum at the metal surface and decays exponentially away from the interface.

modes makes accessible two very attractive phenomena, namely subwavelength (relative to the radiation) waveguiding and (local) field enhancement in nm-sized volumes with obvious applications in nano-photonics and sensing [16, 19, 28–31].

One of the main attractive features inherent to SP modes of a single metal-dielectric interface is their distinctive spatial distribution due to the fact that SP fields decay exponentially into both media and reach their maximum at the interface. This circumstance makes SP modes extremely sensitive to surface properties, in particular, to surface corrugations and heterogeneous structures. Presented in this thesis are various approaches to realization of SP excitation and guiding along nanostructured metal surfaces. Compact configurations for light-plasmon conversion with subsequent focusing of SPs and hence electric-field enhancement are investigated. These techniques constitute building blocks not only for integrated plasmonics but also for realization of the lab-on-a-chip concept.

Chapter 2

Scanning near-field optical microscopy

Since SPs are quasi-2D electromagnetic waves bound to the metal-dielectric interface [32], the most universal method for their investigation is scanning near-field optical microscopy (SNOM). By the very nature of SPs, their fields cannot be detected at a (considerable) distance from the surface unless those fields are scattered (purposefully or not) into propagating modes. The latter is achieved by a probe of a SNOM apparatus. However, let us leave for a while the ability of a SNOM to detect SP fields and consider the principles of near-field microscopy itself, since it is very valuable to optics on the nanometer scale.

We know from the classical optics that the smallest details which can be detected are always larger than a half wavelength. This limitation is imposed by the fact that until recently all observations and measures have been made far away from the object, at least a few wavelengths distant. In fact, two regions must be distinguished: the first one, a few nanometers from the surface, is called the *near-field zone* and contains both electromagnetic-field components able to propagate and components confined over the surface and damping outside. The latter, named evanescent waves, are inhomogeneous waves and exist because of the presence of matter and thus cannot exist in free space. The other region is referred to as the *far-field zone*. It extends from the near-field zone to infinity and contains only propagating waves. However, it does not mean that it is possible to separate physically those two kinds of waves. This nonseparability is a consequence of the analyticity of the electromagnetic signal. In fact, the nonpropagating components exist because the propagating components do and vice versa [33].

Evanescent waves are characterized by amplitudes that decay rapidly into at least one direction in space. The respective component(s), say k_z, of the wavevector are imaginary (more generally, complex). The residual component(s) k_x hence can be larger (in fact much larger) than $|\mathbf{k}|$ according to equation $\mathbf{k}^2 = k_x^2 + k_y^2 + k_z^2$. Therefore, from the Heisenberg's uncertainty principle with respect to position (Δx) and momentum ($p_x = hk_x/2\pi$) of a photon, $\Delta x p_x = h/2\pi$, the

resolution Δx can be much smaller than $\lambda/2\pi \approx 100$ nm. This makes the use of evanescent waves the key to nano-optics [34].

Practically, for experimentalist, the existence of non-radiating components has disastrous consequences because a part of the information contained in the object which is transferred in the non-radiating field, *will not* be transmitted to the detector. What is worse is that the non-radiating components contain the information about the subwavelength details of the object [35]. This assumes that the detector of light must be placed and driven a nanometric distance away from the object without touching it. In addition, because of local detection, no image can be directly obtained. In order to generate an image-like structure, the detector must scan the object surface. A number of different modalities of SNOM devices has been developed to realize this principle. The overwhelming majority of them, instead of using a point-like detector able to collect the light locally, exploits a probe which scatters the near field into the free space or through a suitable light guide towards a photodiode or a photomultiplier.

2.1 Transfer function

Transfer function (TF) is an important notion in any imaging technique, which allows one to relate an image and an object presuming, of course, that the process of image formation is linear. Most often, the intensity distribution of light in an image is related to the intensity distribution at the corresponding object plane. It determines the spatial resolution of an imaging instrument and also allows for consideration of the inverse problem. In conventional (far-field) microscopy, knowledge of the optical TF makes it possible to reconstruct the object structure from a recorded image [36]. The possibility of defining a single and unique TF results from the fact that the object does not interact with the collector (a microscope objective). In other words, whatever the microscope, the light emitted by the object to be imaged is not (or at least to a small extent) perturbed by the objective. In SNOM, multiple scattering in the probe-sample system usually takes place. Therefore one should consider the self-consistent field, which greatly complicates the situation. It has been shown [37], however, that the probe-sample interaction is negligible in photon-tunneling (or, in general, collection) SNOM with uncoated fiber probes. For this reason the TF is mainly discussed in relation to the collection SNOM.

The notion of TF in near-field microscopy have been implicitly assumed already in 1993 by Tsai *et al.* [38] and by Meixner *et al.* [39] in their works with experimental determination of spatial resolution of collection SNOM. Theoretical investigations, showing that the signal detected in collection SNOM is proportional to the square modulus of the electric near field [40] and suggesting accounting for a finite size of the probe by means of a TF [41], resulted in wide usage of the intensity TF while treating the experimental results [42–46]. This

intensity TF relates the Fourier transform (FT) of a near-field optical image to the FT of a corresponding intensity distribution. Nevertheless, the very existence of such function has been questioned judged on the basis of numerical results [47], experimentally in the context of probe characterization [48] and theoretically [49] using treatment of image formation developed previously by Greffet and Carminati [50]. Moreover, it has been shown that the notion of intensity TF can be used in only some particular cases, i.e., using several approximations [49]. Instead, an *amplitude-coupling function* has been suggested for the characterization of collection SNOM, which will further be referred to as TF. From the point of view of SNOM resolution, the most important characteristic is the TF magnitude or, more precisely, its decay for high spatial frequencies corresponding to evanescent field components. It is this decay that (along with the noise level) determines the spatial resolution attainable with SNOM.

We shall now try to introduce a simple expression for the TF, which is derived by assuming an effective point of (dipole-like) detection inside the SNOM probe's tip. We consider characterization of a near-field optical probe in terms of detection efficiency of different spatial frequencies associated with propagating and evanescent-field components.

Expression for transfer function

Let us consider image formation in the collection SNOM, in which a fiber tip scanned near an illuminated sample surface is used to probe an optical field formed at the surface (Fig. 2.1). This field is scattered by the tip, also inside the fiber tip itself, coupling thereby to fiber modes that are formed far from the probe tip and propagating towards the other end of the fiber to be detected [49, 50]. To relate the fiber-mode amplitudes to the plane-wave components of the probed field, it is convenient to make a plane-wave Fourier decomposition of the incident electric field $\mathbf{E}(\mathbf{r}_\parallel, z)$ in the plane $z = 0$ parallel to the surface and passing through the probe tip end:

$$\mathbf{E}(\mathbf{r}_\parallel, 0) = \frac{1}{4\pi^2} \iint \mathbf{F}(\mathbf{k}_\parallel, 0) \exp(i\mathbf{k}_\parallel \cdot \mathbf{r}_\parallel)\, d\mathbf{k}_\parallel, \tag{2.1}$$

where $\mathbf{r}_\parallel = (x, y)$ and $z = 0$ are coordinates of the tip end, $\mathbf{k}_\parallel = (k_x, k_y)$ is the in-plane projection of the wave vector, and $\mathbf{F}(\mathbf{k}_\parallel, z)$ is the vector amplitude of the corresponding plane-wave component of the incident field. Since, as already mentioned, the multiple probe-sample scattering can be disregarded in the collection SNOM, the field described by Eq. (2.1) is considered to be the only one that makes a contribution to the detected signal. In order to relate the plane-wave components to the fiber-mode amplitudes excited in the probe fiber, we further assume that the fiber used is single-mode and weakly guiding, oriented perpendicular to the surface, and terminated with a probe tip possessing axial symmetry. Note that, for weakly guiding fibers (having a very small index

difference between the fiber core and its cladding), the guided modes represent approximately transverse-electromagnetic (TEM) waves. Thus, in the considered case, any propagating-field distribution can be decomposed into two orthogonally polarized fiber modes, whose amplitudes we shall denote as A_x and A_y. It should be mentioned that the origin of the probed field [see Eq. (2.1)] is irrelevant in this consideration and that the sample surface serves merely as a reference plane surface sustaining the field with high spatial frequencies (i.e., evanescent-wave components).

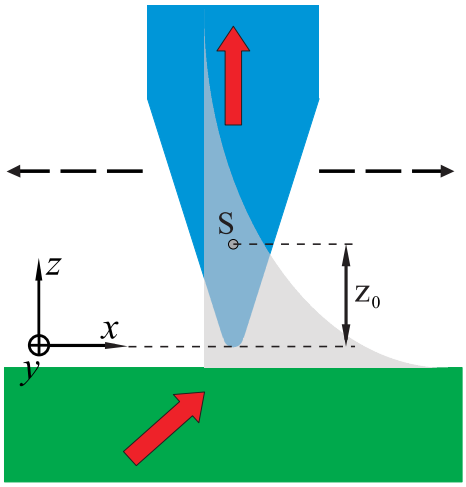

Figure 2.1: Coordinate system and schematics of near-field detection by a fiber tip. Point S situated at distance z_0 from the tip extremity represents an effective detection point at which coupling of the incident field to the fiber mode is considered to take place.

We can further reason that, in the case of s-polarized illumination, one should expect to find, for symmetry reasons, only a y-polarized component of the field in the above plane-wave decomposition and a similarly polarized fiber mode (Fig. 2.1). In the case of p polarization, one should, however, expect to find x- and z-polarized field components in the above decomposition. Again using symmetry considerations, it transpires that both components can contribute only to the x component of the fiber mode, since the z-polarized field component having the symmetric orientation with respect to the probe axis does propagate along the x axis. Taking these arguments into account we can express the mode amplitudes of a (single-mode) fiber as follows:

$$\begin{aligned} A_y(\mathbf{r}_\parallel) &= \frac{1}{4\pi^2}\iint H_{yy}(\mathbf{k}_\parallel)F_y(\mathbf{k}_\parallel,0)\exp(i\mathbf{k}_\parallel\cdot\mathbf{r}_\parallel)\,d\mathbf{k}_\parallel, \qquad (2.2)\\ A_x(\mathbf{r}_\parallel) &= \frac{1}{4\pi^2}\iint [H_{xx}(\mathbf{k}_\parallel)F_x(\mathbf{k}_\parallel,0) + \\ &\qquad + H_{xz}(\mathbf{k}_\parallel)F_z(\mathbf{k}_\parallel,0)]\exp(i\mathbf{k}_\parallel\cdot\mathbf{r}_\parallel)\,d\mathbf{k}_\parallel, \end{aligned}$$

where $H_{ij}(\mathbf{k}_\parallel)$ are the coupling coefficients that account for the contribution of

the jth plane-wave component to the ith component of the fiber-mode field. The matrix $\mathbf{H}$ composed of (amplitude-coupling) coefficients H_{ij} plays a role of TF, which represents the coupling efficiency for various spatial frequencies and, for example, determines the maximum attainable spatial resolution when imaging with the SNOM.

The exact form of the TF depends, in general, on the probe characteristics (shape, refractive-index composition, etc.) and can be rather cumbersome to determine [50]. It is clear, however, that the TF magnitude should decrease for high spatial frequencies. This is probably the most important feature of the TF that should be present in any TF approximation. We suggest a description of the TF using the following model. Let us view the detection process as radiation scattering by a point-like dipole situated inside the tip (point S in Fig. 2.1) at the distance z_0 from the tip extremity. Its scattering efficiency (into a given fiber mode) depends only on the corresponding component of the (incident) field at the site of the dipole:

$$\begin{aligned} A_y(\mathbf{r}_\parallel) &= c_\parallel E_y(\mathbf{r}_\parallel, z_0), \\ A_x(\mathbf{r}_\parallel) &= c_\parallel E_x(\mathbf{r}_\parallel, z_0) + c_\perp E_z(\mathbf{r}_\parallel, z_0). \end{aligned} \tag{2.3}$$

Making decompositions in the field expressions above that are similar to that in Eq. (2.1) but at the plane $z = z_0$ containing the detection point S, one obtains

$$\begin{aligned} H_{yy}(\mathbf{k}_\parallel)F_y(\mathbf{k}_\parallel, 0) &= c_\parallel F_y(\mathbf{k}_\parallel, z_0), \\ H_{xx}(\mathbf{k}_\parallel)F_x(\mathbf{k}_\parallel, 0) + H_{xz}(\mathbf{k}_\parallel)F_z(\mathbf{k}_\parallel, 0) &= c_\parallel F_x(\mathbf{k}_\parallel, z_0) + c_\perp F_z(\mathbf{k}_\parallel, z_0), \end{aligned} \tag{2.4}$$

Finally, taking into account that $H_{xx} = H_{yy}$ and considering only evanescent-field components, the following relations for the TF components can be written:

$$\begin{aligned} H_{xx}(k_\parallel \geq k_0) = H_{yy}(k_\parallel \geq k_0) &= c_\parallel \exp\left(-z_0\sqrt{k_\parallel^2 - k_0^2}\right), \\ H_{xz}(k_\parallel \geq k_0) &= c_\perp \exp\left(-z_0\sqrt{k_\parallel^2 - k_0^2}\right). \end{aligned} \tag{2.5}$$

where k_0 is the wavenumber in air, i.e., $k_0 = 2\pi/\lambda$ and λ is the light wavelength in air. The obtained (approximate) TF expressions [Eqs. (2.2) and (2.5)] represent the main result of our consideration. This approximation being simple and rather transparent also preserves the vectorial character of the TF [49, 50] and contains the detection roll-off for high spatial frequencies.

In the case of s polarization (containing evanescent-wave components), the first formula in Eqs. (2.5) can be applied directly. For p polarization, however, one has to consider two components, parallel and perpendicular to the surface plane ($\mathbf{E}_p = \mathbf{E}_\parallel + \mathbf{E}_\perp$), whose detection efficiencies related to the coefficients H_{xx} and H_{xz} are different. When deriving an expression for the TF in this case, one should take into account the ratio $E_z/E_x = ik_\parallel/\sqrt{k_\parallel^2 - k_0^2}$, which can be obtained

easily from the Gauss law: div$\mathbf{E} = 0$. Furthermore, one should expect that the coupling coefficients (H_{xx} and H_{xz}) are different not only in magnitude but also in phase, arriving at the following expressions:

$$\begin{aligned} H_s(k_\parallel \geq k_0) &= A \exp\left(-z_0\sqrt{k_\parallel^2 - k_0^2}\right), \\ H_p(k_\parallel \geq k_0) &= B\sqrt{1-(k_0/k_\parallel)^2}\exp\left(-z_0\sqrt{k_\parallel^2 - k_0^2}\right) + \\ &\quad + C\exp(i\varphi)\exp\left(-z_0\sqrt{k_\parallel^2 - k_0^2}\right). \end{aligned} \tag{2.6}$$

Formulas in the above equation allows for fitting of numerically simulated transmission through fiber probes with different apex angles, revealing hereby SNOM tips' main properties and showing the dependence of those on the probe geometry.

Fitting numerical data

The numerical data to be fitted with the developed earlier expression for the TF [see Eqs. (2.6)] have been produced by Niels Gregersen at the research center COM, Technical University of Denmark [51]. For an incoming plane wave with a specific value of $k_\parallel = |\mathbf{k}_\parallel|$, the amount of power coupled to the fundamental fiber mode has been determined [Fig. 2.2(a)]. Varying the value of $k_\parallel$, the (spatial) frequency-dependent transmission has been obtained, which is related to the squared magnitudes of the TF components. It has been argued elsewhere [52, 53] that the use of two-dimensional (2D) simulations simplifies considerably the computational effort without loss of the essential features of the SNOM imaging process. So a 2D fiber with uniformity along one lateral axis has been considered in simulations. The core and cladding indices of the fiber are 1.459 and 1.457, respectively; the core diameter is 4 μm, and, to increase computation speed, a reduced cladding diameter of 20 μm was chosen. The opening angles were varied from 10° to 70°.

The resulting transmission for two polarizations of the incident field and for various opening angles exhibits strong oscillations for propagating-field components, whereas it rapidly and monotonously decreases for high spatial frequencies corresponding to evanescent-field components [Fig. 2.2(b,c)]. We consider strong oscillations as the manifestation of Mie (shape) resonances that can be excited in an uncoated fiber tip by propagating waves. Perhaps a better understanding of such behavior of the registered signal can be perceived considering the image of light intensity distribution obtained with a CCD camera placed in front of the probe, with the laser radiation being coupled in the fiber from another end (Fig. 2.3). Here, one should expect to find the reciprocity between the illumination and collection SNOM modes [50].

Using Eqs. (2.6) we fitted the evanescent roll-off in the numerical data. Fitting parameters yielded as a result of the procedure are shown in Table 2.1.

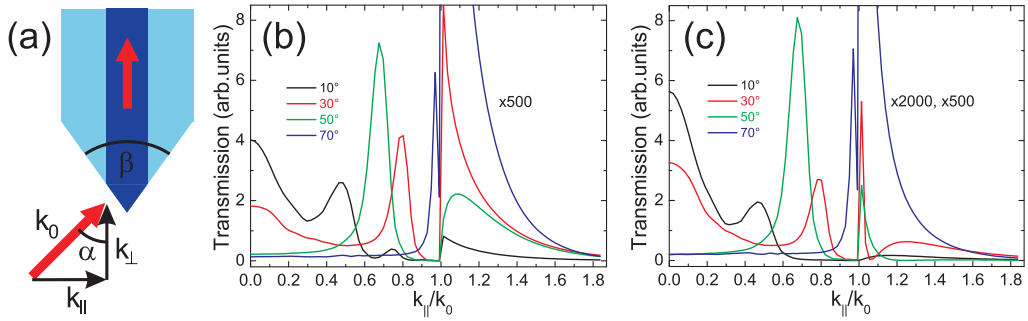

Figure 2.2: (a) Two-dimensional geometry used in numerical simulations of the coupling process. The following parameters have been used in the simulations: $\lambda = 633$ nm, core diameter of 4 μm, core index of 1.459, cladding index of 1.457. (b,c) Numerical results for the coupled (transmitted through the fiber) electric field amplitude obtained for (b) s and (b) p polarization and for different apex angles β: 10° (black curve), 30° (red), 50° (green), and 70° (blue). Note that in the evanescent field domain ($k_{\|}/k_0 > 1$) the data are multiplied by a particular factor for visibility: for s polarization (all angles) by a factor of 500, and for p polarization either by a factor of 500 (10° and 30°) or 2000 (50° and 70°).

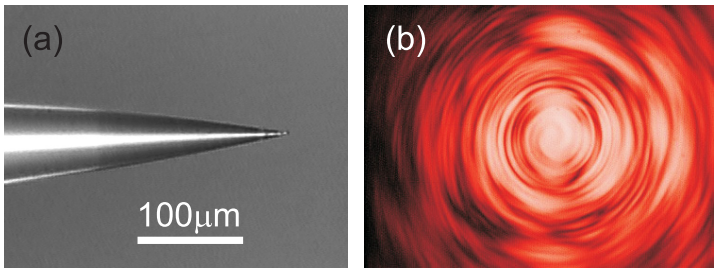

Figure 2.3: (a) Fiber probe used to obtain light-intensity distribution in front of its tip with the laser radiation being coupled into the fiber from the other end. (b) Light distribution in front of the fiber tip recorded with a CCD array.

Fitting parameters for different tip apex angles

Tip apex angle	z_0	A	B	B/C
10°	(138 ± 20) nm	0.14	0.19	24.8
20°	(141 ± 20) nm	0.25	0.29	12.1
30°	(151 ± 35) nm	0.24	0.82	3.0
40°	(146 ± 35) nm	0.31	0.50	2.1
50°	(155 ± 20) nm	0.39	0.51	1.7
60°	(160 ± 35) nm	0.49	0.47	1.2
70°	(210 ± 20) nm	1.02	1.58	1.4

Table 2.1: Parameters found from fitting the data obtained in the numerical simulations of detection efficiency for different spatial frequencies: distance z_0 – position of the effective detection point of a near-field probe; A – contribution coefficient from the incident field of the s-polarized light to the coupled field; B – contribution coefficient from the in-plane incident field component of the p-polarized light to the coupled field; B/C – ratio of the contributions from the in-plane and perpendicular to the plane incident field components of the p-polarized light to the coupled field. The values are presented for different tip apex angles of the near-field probe.

Discussions

Use of fitting parameters allows one to interpret the results of the numerical simulations revealing their connections to the features observed experimentally. Thus a good correspondence between calculated field intensity distributions at a 100-nm distance over a rough nanostructured surface and near-field intensity distributions measured with the tip–surface distance of ~ 5 nm was found [54], suggesting that the effective detection point was located inside a fiber tip at a distance of ~ 100 nm from its extremity. Measurements and simulations of field's phase and amplitude distributions over diffraction gratings also supported the concept of effective detection occurring at some distance from the tip extremity [55]. The increase of the distance z_0 with the increasing apex angle (see Table 2.1) implies that sharper tips are better suited for SNOM imaging with high spatial resolution, which has been one of the first features associated with the photon-tunneling SNOM [38–40].

On the other hand, it has been experimentally demonstrated that SNOM detection introduces polarization filtering, so that the field component perpendicular to the surface is detected (with an uncoated fiber tip) less efficiently than the parallel component [56]. In our case, the polarization filtering is seen in the fact that the ratio B/C was found to be larger than unity. Note that the ratio B/C that is very large for sharp tips decreases rapidly with the increase in the apex angle. This tendency also agrees well with the experimental results on polarization filtering [56]. Knowing this fact is essential in detection of SPs whose electric field is predominantly polarized perpendicular to the surface. The absolute increase of coefficients A and B with the increasing apex angle means that the detected signal is expected to be larger for blunter tips, a feature that has also been frequently noted (e.g., [40] and [48]).

2.2 Refractive-index profile

As in any optical microscopy, the contrast mechanism can be easily adapted for SNOM to study different properties, such as refractive-index and optical-phase profile, linear and nonlinear absorption, chemical structure and local stress. Here we demonstrate the use of reflection mode of SNOM for imaging refractive-index profile of a single-mode optical fiber with step-index profile.

The basic idea of the considered technique is as follows. The illumination of the surface is provided by an etched optical fiber, which is scanned along the surface at a distance d, acting as a source of incident light and as a detector [Fig. 2.4(a)]. The fiber tip acts as a small-sized scatterer reflecting (partially) light back into the fiber and collecting (partially) radiation reflected by the surface. These two field contributions propagate in the fiber and are (coherently) detected by a detector, whose signal contains also a constant incoherent component of noise background. The detected optical signal can thus be presented as

$S \sim I = A^2 + B^2 + C^2 + 2AB\cos(\Delta\varphi)$, where A and B are amplitudes of the light waves reflected by the fiber tip and the surface, respectively, $\Delta\varphi = \Delta\varphi_0 + 4\pi d/\lambda$ is the phase difference between the two waves, and C is the noise amplitude. The surface refractive index is encoded in the reflected wave amplitude via the Fresnel relation: $B = rB_0 = \frac{n-1}{n+1}B_0$, so that the signal variation along the scanning coordinate x can be expressed as follows:

$$\Delta S(x) \sim 2B \cdot \Delta B + 2A\cos(\Delta\varphi)\Delta B = 4B\frac{\Delta n}{n^2-1}(B + A\cos(\Delta\varphi)) \qquad (2.7)$$

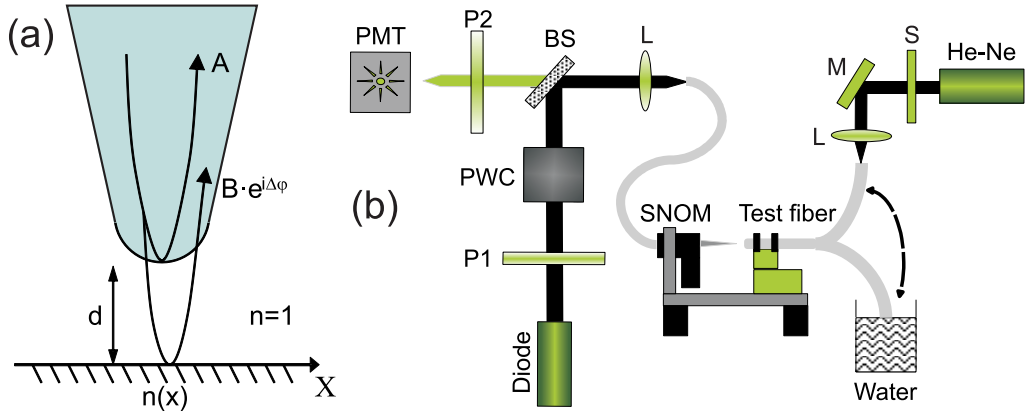

Figure 2.4: (a) Schematics of the detection process: x axis is the scanning coordinate in the surface plane, A – amplitude of the field reflected by the fiber tip, $B\exp(i\Delta\varphi)$ – field reflected from the surface being scanned and captured by the tip, d is the tip-surface distance. (b) Schematic layout of the experimental setup: diode laser (λ = 670 nm and $P \sim$ 1.5 mW), He-Ne laser (λ = 633 nm and $P \sim$ 3 mW), P1 and P2 – polarizers, L – lens, M – mirror, BS – beam splitter, PWC – power controller maintaining a constant level of the radiation power, PMT – photo-multiplying tube.

Denoting the noise related signal by N so that $(S-N) \sim A^2+B^2+2AB\cos(\Delta\varphi)$, one obtains the following expression for the ratio of signal variation to signal:

$$\frac{\Delta S(x)}{S-N} = \frac{4\Delta n}{n^2-1} \cdot \frac{1 + k\cos(\Delta\varphi)}{1 + 2k\cos(\Delta\varphi) + k^2} \qquad (2.8)$$

where $k = A/B$. It is seen that the ratio $\Delta S/(S-N)$, which determines the sensitivity of this method, is strongly influenced by the amplitude ratio k and the phase difference $\Delta\varphi$. For a given tip-surface distance, the tip itself determines the phase difference and amplitude ratio by its geometrical and physical properties. For example, in our experiments, we found that the amplitude ratio is close to 0.5 and that the phase difference is close to but larger than π. Note that, depending on the detection configuration, the sensitivity of this technique can be made extremely large, e.g., for $k = 1$ and $\Delta\varphi = \pi$, or extremely small, e.g., for $k = 2$ and $\Delta\varphi = 2\pi/3$.

The experimental setup [Fig. 2.4(b)] consists of a stand-alone SNOM apparatus whose uncoated sharp fiber tip was scanned along the fiber surface at a constant distance (a few nanometers) maintained by the shear-force feedback. The radiation coupled into the SNOM fiber was reflected back into the fiber by the investigated surface (with the shutter S being closed) and detected at the fiber output with a photomultiplier. In order to avoid light reflection from the opposite edge of the fiber under investigation, that fiber edge was put into the water. In order to increase the signal-to-noise ratio (SNR), we used cross-polarized detection, in which the polarization of the detected light is perpendicular to that of the light coupled in to the fiber [57]. The reason for the high SNR would be that the polarization conversion is most efficient near the end of the fiber tip, where multiple reflections of light take place, and the influence of propagating field components, especially those emitted by the outer part of the tip, should be strongly decreased (increasing thereby the SNR).

The typical SNOM images (Fig. 2.5) exhibit the expected ring-shape structure with the bright circle representing the fiber core and the dark spot in the middle corresponding to the Ge depletion index-dip at the core center [58]. Quantitative description of the signal variation across the core region can be obtained by taking an average of several radial cross-cuts of the optical image decreasing the influence of noise. The resulting average cross-section [Fig. 2.6(a)] indicates also the two main signal variations.

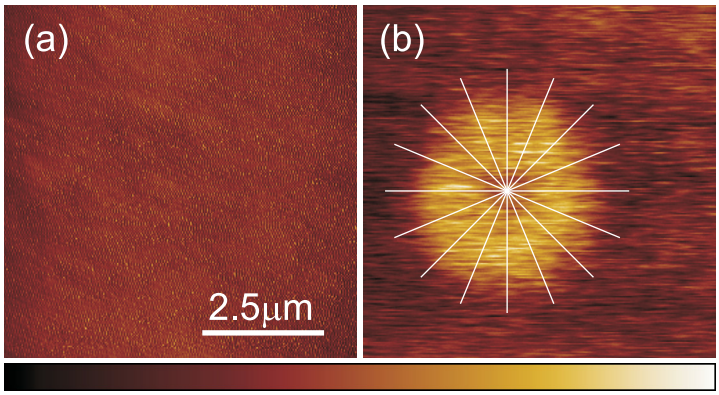

Figure 2.5: (a) Topographical and (b) near-field optical images (7.2×7.2 μm^2) of the cleaved output edge of the fiber under investigation obtained at a wavelength $\lambda = 670$ nm (diode laser).

In order to find the corresponding refractive-index variations, one should determine the amplitude ratio k and the phase difference $\Delta\varphi$ [see Eq. (2.8)]. We used a technique, which is similar to that suggested for the tip-surface distance control [59]. It is based on the signal detection while approaching a surface with the fiber tip. The corresponding signal dependence exhibited oscillations with the period of $\sim \lambda/2$ [Fig. 2.6(b)] as expected. Approximating the field B by a diverging spherical wave we fitted the experimentally obtained signal dependence

with that given by $S \sim A^2 + B^2 + C^2 + 2AB\cos(\Delta\varphi_0 + 4\pi d/\lambda)$, trying to match maxima and minima of these dependences. The following interference parameters have been found: $k = A/B \approx 0.41$, $\Delta\varphi \approx 1.17\pi$. For these parameters, the refractive-index difference between the fiber core and cladding was calculated to be ~ 0.018, a value which is twice larger than that (0.009) known from the fiber producer.

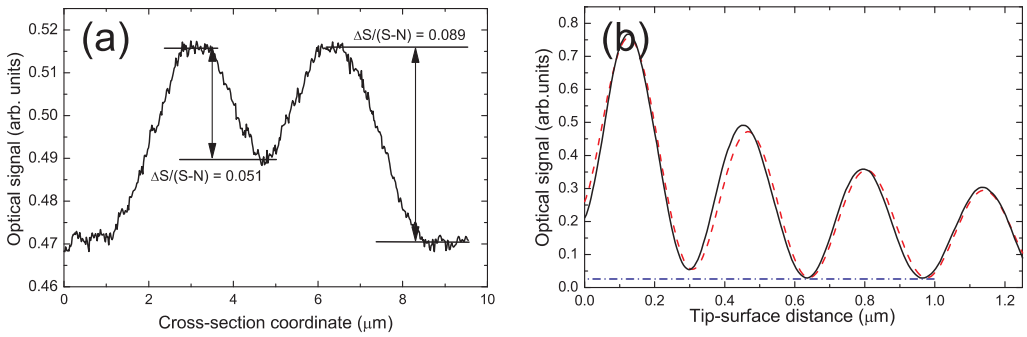

Figure 2.6: (a) SNOM image profile taken across the center of the fiber obtained by averaging the corresponding cross-cuts made along the white lines in Fig. 2.5(b). (b) Detected optical signal as a function of the tip-surface distance (solid curve), and the corresponding fitted dependence (dashed curve). Dash-dotted line shows the noise level.

It appears that it is very difficult to achieve high accuracy of the developed technique, at least for small variations of the surface refractive index. We believe that the main reasons for the observed inaccuracy are related to the relatively low contrast in the optical images obtained (and therefore large contribution from the noise background) and the accuracy in determination of the main parameters, i.e., the amplitude ratio and phase difference, that exert strong influence on the relation between the observed image contrast and the refractive-index difference.

Chapter 3

Leakage-radiation microscopy

SNOM is an excellent and often the only tool for study SPs due to their evanescent nature. However, the technique itself is very time consuming, and treatment of various features in SNOM images requires much attention and practical experience of experimentalist to avoid disappointing mistakes since, as shown in Sec. 2.1, the relation between an object and its image is much more complicated than in classical microscopy.

In some cases it is possible to map SP waves in real time (without scanning) by collecting secondary radiation emerging as a consequence of SP fields and being in (usually strict) qualitative or quantitative relationship with that. As any far-field microscopy, it is diffraction-limited. Nevertheless, by not requiring to accomplish surface scans with a probe it provides researcher with a quick and handy preview of the processes going on at the surface. Two examples of the technique could be fluorescence imaging of SP fields [60] or imaging of SPs by detecting the light scattered out-of-plane due to surface roughness (see, e.g., [61]). Although it is possible to relate quantitatively the intensity of light detected in far-field, when using those methods, with the strength of the SP field, the procedure is rather cumbersome and gives very approximate values.

There is more precise far-field technique that is called leakage-radiation microscopy (LRM). First suggested by Hecht *et al.* [62] and further quantitatively developed by Ditlbacher *et al.* [63], it employs the inverted Kretschmann configuration for SP excitation as a detection part (Fig. 3.1). Thus it uses evanescent tunneling of SP fields through the supporting metal film into the dielectric substrate and decoupling of those into propagating light due to k-vector matching or momentum conservation. This (elastically) decoupled light is called leakage radiation (LR). Obviously, the extent of tunneling, and hence the intensity of LR that is to be detected, depends on the metal-film thickness. This imposes natural limitations on the applicability of the technique: it can only map SPs sustained by thin metal films.

If the film thickness is large enough to prevent LR (for gold at visible wave-

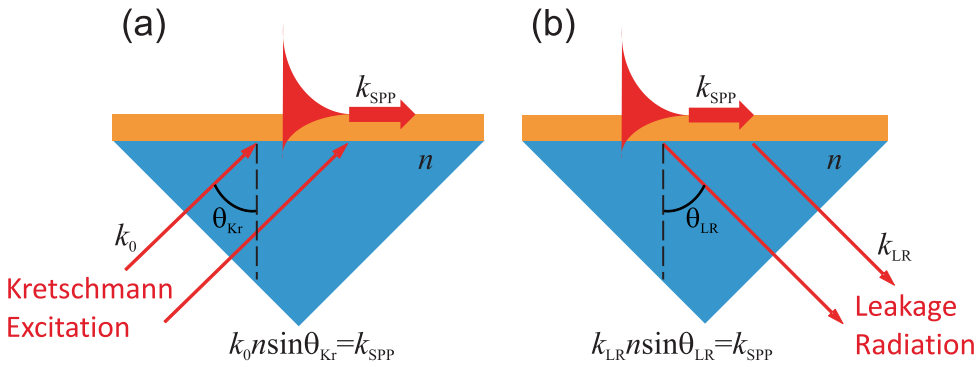

Figure 3.1: Two schematics in comparison with each other: (a) coupling from light into SPs (Kretschmann configuration) and (b) outcoupling from SPs into leakage radiation.

lengths, 200-nm-thick film is already completely opaque) then the whole SP power is dissipated due to the ohmic loss. With the decrease of the film thickness, the LR starts to appear which leads to additional (radiation) loss of the SP power and therefore, the SP propagation length is decreased. For the so-called optimum (for Kretschmann excitation) thickness, the absolute value of the radiation loss of SP equals precisely the internal (ohmic) loss. For gold at free-space wavelength of 800 nm, that thickness is 43 nm. Hence for the optimum film thickness, the SP propagation length is twice as short as that for the infinitely thick film. For practical purposes, it is important to know how the ability of SP to leak into the substrate develops with the changing wavelength, metal thickness and the metal itself because it gives an opportunity to measure SP power by measuring the power of the corresponding LR. In the following section we shall consider some useful relations.

3.1 Leakage coefficient

Let us define a leakage coefficient τ as a relative amount of SP power being elastically radiated into the substrate in the form of LR, i.e.,

$$P_{\mathrm{LR}} = \tau P_{\mathrm{SP}}, \tag{3.1}$$

where P_{LR} is the power of LR and P_{SP} is the total power guided by SP beam. In the steady state, the former is equal to the Poynting vector integrated over the plane perpendicular to the direction of SP propagation and passing through the origination point of SP beam since the ohmic and radiation losses should be compensated for by the power pumped into the SP.

Denoting SP electric-field attenuation along the propagation direction x due to ohmic loss by α and that due to radiation loss by β, the SP field at the metal surface can be written as $E(x) = E_0 e^{-\alpha x} e^{-\beta x}$. Since the SP Poynting vector integrated over the plane $x = const$ contains the field intensity $|E(x)|^2$ of the

SP just at the metal surface, the power transferred by the SP beam through the plane of integration is expressed as follows:

$$P(x) = P_{\mathrm{SP}} e^{-2(\alpha+\beta)x}. \tag{3.2}$$

This formula assumes that the SP emerges at the plane $x = 0$ and its total power (at the origin) is P_{SP}. The value β depends on the metal-film thickness and for an infinitely thick film it is equal to zero, whereas for the optimum film thickness $\alpha = \beta$. The SP propagation length, which depends on the wavelength λ and on the metal-film thickness d, is by definition:

$$L_{\mathrm{SP}}(\lambda, d) = \frac{1}{2(\alpha+\beta)}. \tag{3.3}$$

For short, let us denote $l = L_{\mathrm{SP}}(\lambda, d = d_0)$ and $L = L_{\mathrm{SP}}(\lambda, d = \infty)$. Then from Eq. (3.3) taking into account that $\beta(d = \infty) = 0$, we write:

$$\frac{L_{\mathrm{SP}}(\lambda, d = d_0)}{L_{\mathrm{SP}}(\lambda, d = \infty)} = \frac{l}{L} = \frac{2\alpha}{2(\alpha+\beta)} = \frac{\alpha}{\alpha+\beta}.$$

We shall further need the ratio $\beta/(\alpha+\beta)$ which can be easily obtained from the above equation:

$$\frac{\beta}{\alpha+\beta} = 1 - \frac{\alpha}{\alpha+\beta} = 1 - \frac{l}{L} = \frac{L-l}{L}. \tag{3.4}$$

Differentiating Eq. (3.2), we can express the SP power loss at an interval dx due to internal absorption in the metal and LR: $\frac{dP}{dx} = -2(\alpha+\beta)P(x)$. For an ideal metal without resistance (i.e., when $\alpha = 0$) we get $\frac{dP}{dx}\big|_{\alpha=0} = -2\beta P(x)$. This formula remains valid for real metals if one is interested in the SP power loss only due to LR. Obviously, this SP power loss is equal, with the minus sign, to the power radiated into the substrate from an interval dx. Therefore we write this radiated power P_{LR} as follows:

$$\frac{dP_{\mathrm{LR}}}{dx} = -\frac{dP}{dx}\bigg|_{\alpha=0} = 2\beta P(x).$$

Integration of this equation over x from zero to infinity using Eq. (3.2) gives the total radiated power:

$$P_{\mathrm{LR}} = \int_0^{+\infty} 2\beta P(x)dx = 2\beta P_{\mathrm{SP}} \int_0^{+\infty} e^{-2(\alpha+\beta)x}dx = \frac{\beta}{\alpha+\beta} P_{\mathrm{SP}}. \tag{3.5}$$

Similarly, we could write the total power dissipated in the metal (ohmic loss):

$$P_{\Omega} = \int_0^{+\infty} 2\alpha P(x)dx = 2\alpha P_{\mathrm{SP}} \int_0^{+\infty} e^{-2(\alpha+\beta)x}dx = \frac{\alpha}{\alpha+\beta} P_{\mathrm{SP}}.$$

As expected, in agreement with the energy conservation law $P_{\mathrm{SP}} = P_{\mathrm{LR}} + P_{\Omega}$. We can now express the leakage coefficient using Eqs. (3.5) and (3.4):

$$\tau = \frac{P_{\mathrm{LR}}}{P_{\mathrm{SP}}} = \frac{\beta}{\alpha+\beta} = \frac{L-l}{L}. \tag{3.6}$$

This formula allows obtaining leakage coefficient if SP propagation length is known for a thin metal film under consideration and for metal–dielectric interface of the semi-infinite media. Those, in turn, can be found by employing simple numerical methods (e.g., a transfer-matrix approach) or using approximate relations for α and β. Thus considering a three-layer air/metal/dielectric structure with dielectric permittivities $(\varepsilon_0 = 1)/(\varepsilon_1 = \varepsilon_r + i\varepsilon_i)/\varepsilon_2$ and suggesting $\varepsilon_r < -1$ and $\varepsilon_i \ll |\varepsilon_r|$, one finds [64]:

$$\begin{aligned}
\alpha &= \frac{\omega}{c}\left(\frac{|\varepsilon_r|}{|\varepsilon_r|-1}\right)^{3/2}\frac{\varepsilon_i}{2\varepsilon_r^2}, \\
\beta &= \frac{\omega}{c}\frac{2\gamma}{|\varepsilon_r|+1}\left(\frac{|\varepsilon_r|}{|\varepsilon_r|-1}\right)^{3/2}\exp\left(-\frac{4\pi d|\varepsilon_r|}{\lambda\sqrt{|\varepsilon_r|-1}}\right), \\
\gamma &= \frac{2\varepsilon_2\sqrt{|\varepsilon_r|(\varepsilon_2-1)-\varepsilon_2}}{\varepsilon_2^2+|\varepsilon_r|(\varepsilon_2-1)-\varepsilon_2}.
\end{aligned} \tag{3.7}$$

Requiring that $\alpha = \beta$, we obtain the optimum (for Kretschmann excitation) thickness of the metal film:

$$d_{\mathrm{opt}} = \frac{\lambda\sqrt{|\varepsilon_r|-1}}{4\pi|\varepsilon_r|}\ln\left(\frac{4\varepsilon_r^2\gamma}{\varepsilon_i(|\varepsilon_r|+1)}\right). \tag{3.8}$$

Comparing values obtained numerically and using Eqs. (3.6), (3.7), one can see (Table 3.1) that approximate relations work reasonably good in the whole tabulated wavelength range except for the two smallest wavelengths where the assumption $\varepsilon_i \ll |\varepsilon_r|$ is not valid.

3.2 Experimental setup

The experimental setup for LRM consists of SP-excitation and -detection parts (Fig. 3.2). The former is a (Ti:Sapphire) laser whose illumination is focused onto the surface of a nanostructured gold film on a glass substrate through a microscope objective. To facilitate observation of the surface structure, a lamp illumination is conjugated with the objective. Light–SP coupling is mediated by a single gold ridge or a periodic set of those on the film surface. LR is emitted from the interface between the gold film and a higher-refractive-index medium (the substrate) at a characteristic angle θ_{LR}, at which the SP and LR waves are phase matched [Fig. 3.1(b)]. Since the k-vector of SP is larger than that

SP propagation length on gold

Wavelength, nm	Numeric l, μm	Analytic l, μm	Numeric L, μm	Analytic L, μm
520.3	0.6	0.3	0.6	0.4
542.9	1.2	0.9	1.5	1.3
567.6	2.0	1.8	3.0	2.8
657.3	3.6	3.5	8.5	8.3
693.8	7.8	8.2	17.1	16.9
734.6	13.6	14.4	27.1	27.0
780.5	20.8	22.3	38.5	38.3
832.5	30.4	32.8	52.5	52.2
892.0	40.1	43.5	65.9	65.6
960.6	54.6	59.2	84.8	84.4
1040.7	69.6	76.2	104.7	104.1
1135.3	99.9	109.0	141.4	140.5
1248.8	129.5	141.8	177.3	176.0
1274.3	88.2	99.5	135.5	134.2
1300.8	93.3	104.8	141.8	140.4
1328.5	97.9	110.4	148.2	146.7
1357.4	102.9	116.1	154.7	153.0
1387.5	108.2	122.3	161.7	160.0
1419.1	113.8	129.1	169.5	167.6
1452.1	119.6	135.9	177.4	175.3
1486.6	126.4	143.9	186.3	184.0
1522.9	134.0	152.8	196.4	194.0
1561.0	142.6	162.8	207.9	205.2
1601.0	154.7	176.7	223.4	220.4
1643.1	161.2	184.7	233.0	229.7

Table 3.1: Numerical and approximate analytic data for SP propagation length along 50-nm-thick gold film (l) and along gold-air interface beetween two semi-infinite media (L). "Multilayer waveguides" software developed by Thomas Søndergaard for Micro Managed Photonics A/S has been used to calculate the numerical values.

of the corresponding free-space radiation (LR), the characteristic angle θ_{LR} is always larger than the critical angle of total internal reflection, and the radiation is sometimes called forbidden [62]. Hence an immersion-oil objective (numerical aperture, NA > 1) is used in the detection part of the setup. Imaging of SP fields is accomplished by a charge-coupled device (CCD) camera positioned in the plane optically conjugated with the gold film/substrate interface. The intensity at any point of the image plane is directly proportional to the LR intensity emerging from the corresponding position at the object plane of the microscope, and thus to the SP field intensity on the strength of Eq. (3.1).

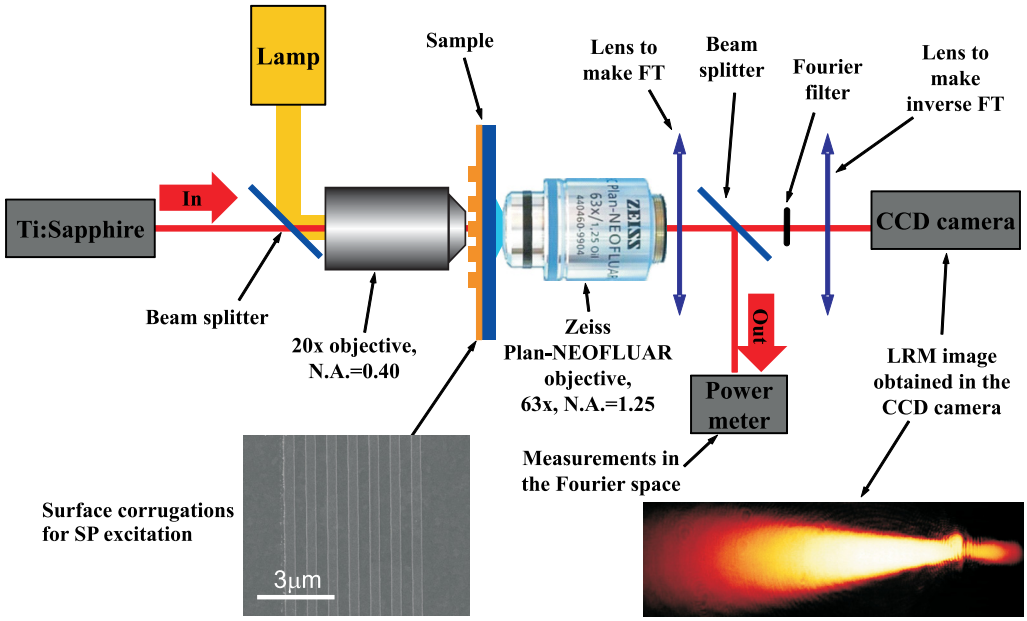

Figure 3.2: Experimental setup for LRM.

The back focal plane of the immersion-oil objective contains a FT of the field collected by this objective, which means that every point of the Fourier plane contains particular (and different from the other points) spatial component of the field emerging at the metal film/substrate interface. This circumstance can be employed to block all field components except for those corresponding to LR, increasing hereby the contrast of the image recorded with the CCD array. At the same time, measuring radiation power in the Fourier plane allows evaluating the whole power guided by SP beam through Eq. (3.1) if coefficient τ is quantified.

The power of the laser beam used for SP excitation and the LR power measured in the Fourier plane are related through the equation

$$\frac{Out}{In} = \tau_{\mathrm{opt}} \eta \tau, \tag{3.9}$$

where τ_{opt} is the optical transmission of the setup (i.e., transmission of all its optical elements), η is the light–SP coupling efficiency (i.e., a relative amount of power transmitted from light into SPs), and τ is the leakage coefficient defined by Eq. (3.1). The product $\eta\tau$ can be considered as an optical transmission of the sample that converts the incident laser power into LR. Equation (3.9) allows simple experiment on measuring light–SP coupling efficiency on various structures. Note that the coefficient τ is wavelength-dependent [Fig. 3.3(a)], which makes smaller-wavelength SP modes leakier for the same metal-film thickness. Thus the optimum thickness of gold film is reduced from 43 nm for 800-nm wavelength down to 31 nm for telecom wavelength of 1500 nm [Fig. 3.3(b)].

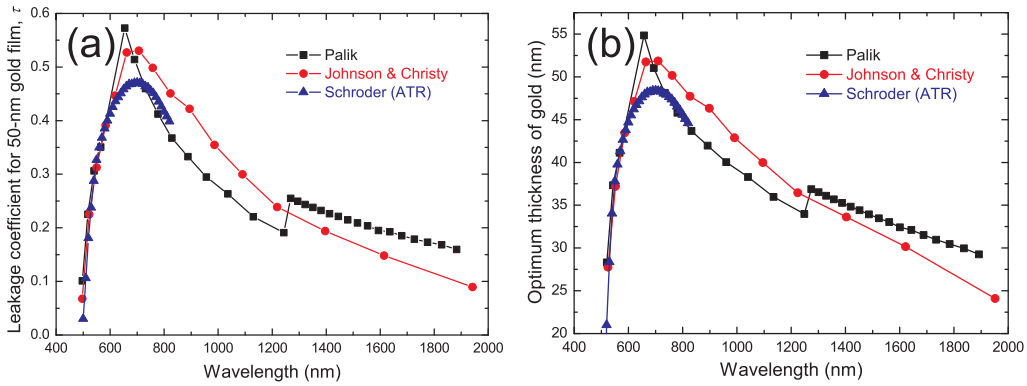

Figure 3.3: Wavelength dependence of (a) leakage coefficient for 50-nm-thick gold film, and (b) optimum (for Kretschmann configuration) thickness of gold film. In both cases a three-layer structure is assumed: the gold layer is sandwiched between a silicon substrate (refractive index $n = 1.45$) and air ($n = 1$). The calculations are made using Eqs. (3.6)–(3.8) at page 22 and refracive indices of gold as given in Palik (black curve) [65], Johnson and Christy (red curve) [66], and Schröder (blue curve) [67].

Part II

Collection of papers

Chapter 1

Adiabatic bends in SPBG structures

Adiabatic bends in surface plasmon polariton band gap structures

Ilya P. Radko, Thomas Søndergaard, and Sergey I. Bozhevolnyi

Department of Physics and Nanotechnology, Aalborg University, Skjernvej 4A, DK-9220 Aalborg Øst, Denmark

ilya@physics.aau.dk

Abstract: Propagation and interaction of surface plasmon polaritons (SPPs) excited in the wavelength range 700–860 nm with periodic triangular arrays of gold bumps placed on gold film surfaces are investigated using a collection near-field microscope. We observe the inhibition of SPP propagation into the arrays within a certain wavelength range, i.e., the band gap (BG) effect. We demonstrate also the SPP propagation along a 30° bent channel obtained by an adiabatic rotation of the periodic array of scatterers. Numerical simulations using the Lippmann-Schwinger integral equation method are presented and found in reasonable agreement with the experimental results.

OCIS codes: (240.6680) Surface plasmons; (250.5300) Photonic integrated circuits; (230.7380) Waveguides, channeled; (180.5810) Scanning microscopy.

References and links

1. H. Raether, *Surface Plasmons on Smooth and Rough Surfaces and on Gratings* (Springer-Verlag, Berlin, 1988).
2. W. L. Barnes, A. Dereux, and T. W. Ebbesen, "Surface plasmon subwavelength optics," Nature (London) **424,** 824–830 (2003).
3. J. R. Krenn, J.-C. Weeber, "Surface plasmon polaritons in metal stripes and wires," Phil. Trans. R. Soc. Lond. A **362,** 739–756 (2004).
4. R. Charbonneau, N. Lahoud, G. Mattiussi, and P. Berini, "Demonstration of integrated optics elements based on long-ranging surface plasmon polaritons," Opt. Express **13,** 977–984 (2005), http://www.opticsexpress.org/abstract.cfm?URI=OPEX-13-3-977.
5. T. Nikolajsen, K. Leosson, and S. I. Bozhevolnyi, "Surface plasmon polariton based modulators and switches operating at telecom wavelengths," Appl. Phys. Lett. **85,** 5833–5836 (2004).
6. M. Hochberg, T. Baehr-Jones, C. Walker, and A. Scherer, "Integrated plasmon and dielectric waveguides," Opt. Express **12,** 5481–5486 (2004), http://www.opticsexpress.org/abstract.cfm?URI=OPEX-12-22-5481.
7. S. I. Bozhevolnyi, J. Erland, K. Leosson, P. M. W. Skovgaard, and J. M. Hvam, "Waveguiding in Surface Plasmon Polariton Band Gap Structures," Phys. Rev. Lett. **86,** 3008–3011 (2001).
8. J. D. Joannopoulos, R. D. Meade and J. N. Winn, *Photonic Crystals* (Princeton University Press, Princeton, NJ, 1995).
9. S. C. Kitson, W. L. Barnes, and J. R. Sambles, "Full photonic band gap for surface modes in the visible," Phys. Rev. Lett. **77,** 2670–2673 (1996).
10. S. I. Bozhevolnyi, V. S. Volkov, K. Leosson, and A. Boltasseva, "Bend loss in surface plasmon polariton band-gap structures," Appl. Phys. Lett. **79,** 1076–1078 (2001).
11. C. Marquart, S. I. Bozhevolnyi, and K. Leosson, "Near-field imaging of surface plasmon-polariton guiding in band gap structures at telecom wavelengths," Opt. Express **13,** 3303–3309 (2005), http://www.opticsinfobase.org/abstract.cfm?URI=OPEX-13-9-3303.
12. M. Kretschmann, "Phase diagrams of surface plasmon polaritonic crystals," Phys. Rev. B **68,** 125419 (2003).
13. T. Søndergaard and S. I. Bozhevolnyi, "Theoretical analysis of finite-size surface plasmon polariton band-gap structures," Phys. Rev. B **71,** 125429 (2005).
14. A. Boltasseva, T. Nikolajsen, K. Leosson, K. Kjaer, M. S. Larsen, and S. I. Bozhevolnyi, "Integrated optical components utilizing long-range surface plasmon polaritons," J. Lightwave Technol. **23,** 413–422 (2005).

15. A. Degiron and D. Smith, "Numerical simulations of long-range plasmons," Opt. Express **14,** 1611–1625 (2006), http://www.opticsinfobase.org/abstract.cfm?URI=oe-14-4-1611.
16. P. Berini and J. Lu, "Curved long-range surface plasmon-polariton waveguides," Opt. Express **14,** 2365-2371 (2006), http://www.opticsinfobase.org/abstract.cfm?URI=oe-14-6-2365.
17. J. Arentoft, T. Søndergaard, M. Kristensen, A. Boltasseva, M. Thorhauge and L. Frandsen, "Low-loss silicon-on-insulator photonic crystal waveguides," Electron. Lett. **38,** 274–275 (2002).
18. DME-DualScope^{TM}, Herlev, Denmark.
19. Y. A. Vlasov, M. O'Boyle, H. F. Hamann, and S. J. McNab, "Active control of slow light on a chip with photonic crystal waveguides," Nature (London) **438,** 65–69 (2005).
20. A. Jugessur, L. Wu, A. Bakhtazad, A. Kirk, T. Krauss, and R. De La Rue, "Compact and integrated 2-D photonic crystal super-prism filter-device for wavelength demultiplexing applications," Opt. Express **14,** 1632–1642 (2006), http://www.opticsinfobase.org/abstract.cfm?URI=OPEX-14-4-1632.

1. Introduction

Surface plasmon polaritons (SPPs) are quasi-two-dimensional waves propagating along a metal-dielectric interface [1]. SPP fields decay exponentially into both media and reach maximum at the interface, a circumstance that makes SPPs extremely sensitive to surface properties. SPP guiding structures are basic elements of most plasmonic components needed to route optical signals in photonic devices and optical interconnects [2]. Many fundamental properties of SPPs have been studied, and a number of SPP guiding structures have been suggested, including SPP guiding along metal stripes [3-5] and their edges [6], as well as along channels in periodic arrays of scatterers (bumps) placed on metal surfaces [7]. In the latter case, the main principle is similar to that known for photonic crystals [8], i.e., the inhibition of SPP propagation within a certain wavelength range in periodic scattering arrays. The possibility to fabricate periodically corrugated metal surfaces exhibiting a full band gap (BG) for SPPs was first demonstrated 10 years ago [9]. Such a BG effect for SPPs excited in the wavelength range of 780–820 nm has been shown to result in efficient SPP guiding, bending and splitting (albeit for relatively small angles) by line defects in periodic scattering arrays [10]. There has been shown also the possibility of the SPP propagation in and scattering by such periodic structures at telecom wavelengths [11].

The experimental [10, 11] and theoretical [12, 13] studies of SPPBG structures indicated that the main concern in the context of efficient SPPBG waveguiding is related to the problem of simultaneous realization of the full SPPBG, i.e., the BG for all in-plane directions of SPP propagation. In particular, low-loss bending (for relatively large angles) seems to depend crucially on the realization of full SPPBG, which turned out to be a challenging problem [11, 13]. One can try to circumvent this problem by using adiabatic bends for stripe SPPs [3] or long-range SPPs [14-16]. In both cases, SPP modes supported by thin metal stripes are only weakly guided implying that the bend radii should be relatively large in order to keep the bend loss at an acceptable level. Usage of SPPBG structures might be less restrictive in this respect because the SPP propagation outside a bent channel (into the periodic structure) is prohibited for the wavelengths in the BG [9, 10]. For this reason, we have decided to explore the potential of gradually bent SPPBG structures containing straight channels for low-loss guiding around large-angle bends. Similarly bent (curved) channels have been successfully used in low-loss silicon-on-insulator photonic crystal waveguides [17]. Here we demonstrate the SPP propagation in the periodic array of scatterers along a 30° bent channel obtained by an adiabatic rotation of the triangular lattice. Using a scanning near-field optical microscopy (SNOM) arrangement operating in collection mode [10], we consider the SPP excitation in the wavelength range 700–860 nm along gold films covered with periodic arrays of gold bumps, and demonstrate the inhibition of SPP propagation into the arrays within a certain wavelength range as well as the SPP propagation along the bent channel.

2. Experimental setup

The experimental setup used in this work is shown in Fig. 1. It consists of a collection SNOM [18] in which the near-field radiation scattered by an uncoated sharp fiber tip into fiber modes is detected, and an arrangement for SPP excitation in the Kretschmann configuration [1]. The *p*-polarized (electric field is parallel to the plane of incidence) light beam from a tunable Ti:sapphire laser ($\lambda = 700$–860 nm, $P \sim 100$ mW) is weakly focused (spot size ~ 300 μm) onto the sample attached with immersion oil to the hypotenuse side of a right-angle BK7 glass prism. The SPP excitation is usually recognized as a minimum in the angular dependence of the reflected light power (attenuated total reflection) [1]. In our case, the SPP excitation is manifested by a dark stripe in the reflected beam spot. A sharp tip, obtained by a standard chemical etching technique in 40% hydrofluoric acid, is scanned over the surface at a constant distance maintained by shear-force feedback. The optical signal picked up by the fiber tip is then converted by a photomultiplier tube and amplified in a lock-in amplifier. The setup used allows us to make far-field observations of the sample for preliminary adjustment of the position and the size of a focal spot from the laser. Once the adjustment is accomplished, the far-field arrangement is removed and the near-field scanning head is placed instead.

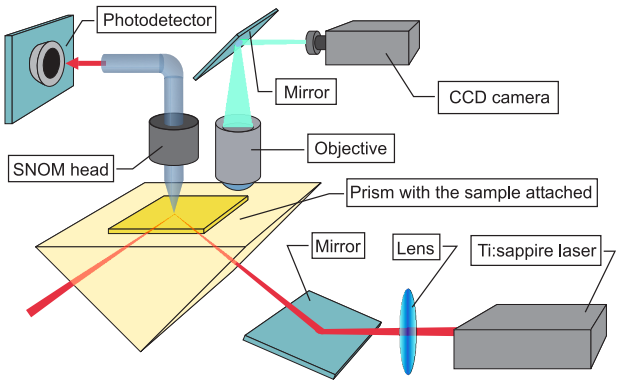

Fig. 1. Schematic of the experimental setup.

The SPPBG structures we consider in this work consist of 60-nm-thick gold films deposited on silica substrate and covered with gold bumps having height ~ 60 nm and square profile of ~ 133 nm or ~ 166 nm on the side. This patterning was microfabricated by electron-beam lithography on a resist layer on the thin film, evaporation of a second gold layer and lift-off. The reason for choosing parallelepiped-shaped bumps instead of cylinders is the ease of fabrication, which is also less time consuming. The gold bumps have been arranged to form a 30° adiabatic bend of a triangular lattice with period 475 nm and ΓM orientation of the irreducible Brillouin zone of the lattice [8]. Figure 2 represents the design of two bends investigated. Structure A (Fig. 2(a)) is designed to have the radius of curvature of the bend being 16 μm and combined of square bumps being 133 nm on the side. Structure B (Fig. 2(b)) has the radius of curvature equal to 32 μm and square bumps being 166 nm on the side. In both of the structures a channel has been cut through the array by removing 4 lines of scatterers.

3. Experimental results

The first task was to observe the SPPBG effect with these structures. This has been accomplished with structure A (Fig. 2(a)). Typical topographical and near-field optical images obtained with the SPP interaction with the structure are shown in Fig. 3. The SPP propagates

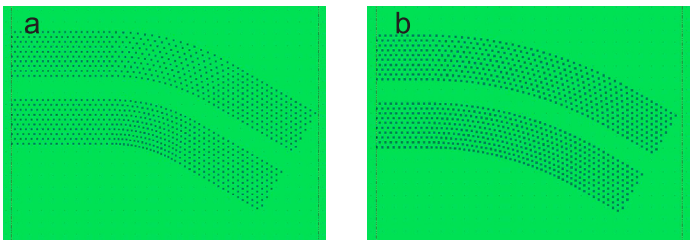

Fig. 2. Design of the adiabatic bends of the triangular lattice having period 475 nm and being arranged in ΓM direction relative to the propagation direction of the incident SPP (from left to right). Both structures are sets of 60-nm-height gold bumps deposited on a 60-nm-thick gold film, and have a channel width of 4 lines of scatterers removed. (a) Structure A: the radius of curvature of the bend is 16 μm, square bumps are 133 nm on the side. (b) Structure B: the radius of curvature of the bend is 32 μm, square bumps are 166 nm on the side.

from left to the right in the figure and it is excited *globally* at an area covering the structure completely, for the spot size from the Ti:sapphire laser is ~ 300 μm whereas the size of the structure is about 25×15 μm. For this reason the field of the incident SPP can be considered as a plane wave. Due to the interaction of the SPP and the surface microstructure, the inhibition of SPP propagation into the array can be observed. In order to estimate the penetration depth an averaged cross section has been made inside the structure as shown by the white bar on Fig. 3(b). Fitting obtained exponentially decaying SPP intensity profiles yields us wavelength dependent penetration depth, which is shown on Fig. 3(e). One can clearly notice a BG near 770 nm wavelength. With the structure A we, however, did not succeed in obtaining effective SPP guiding through the bent channel: the signal drops down drastically after the bend.

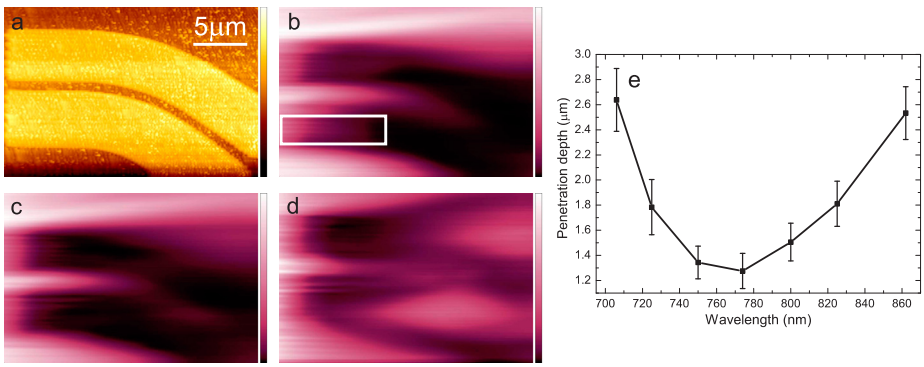

Fig. 3. Shear-force topography (a) and near-field imaging of SPP interaction with the structure A obtained for different wavelengths: (b) 706 nm, (c) 750 nm, and (d) 825 nm. (e) Wavelength dependence of the SPP penetration depth obtained from the SNOM images.

Structure B differs from A by larger radius of curvature (which is 32 μm against 16 μm in the case of structure A) and by larger bump side length (166 nm against 133 nm). While the former leads to more effective SPP guiding after the bend, resulting in a lower bend loss of the structure, the SPPBG is expected to broaden due to the larger bumps in the latter [13]. The filling factor is defined as the ratio of the area occupied by the bump forming one lattice cell to the area of that. For a triangular lattice with square bumps, the filling factor is obtained by $f = \frac{2a^2}{p^2\sqrt{3}}$, where a and p are the side of the square bump and the period of the lattice, respectively. In

our case we get filling factor 0.09 for structure A and 0.14 for structure B. According to the theoretical considerations [13], the SPPBG effect and waveguiding in structure B (having a larger filling factor) should be more pronounced and efficient than those in structure A.

With the conditions of SPP excitation being the same as with the structure A, we observed efficient SPP guiding along the bent channel in the structure B (Figs. 4(a) and 4(b)) at the light wavelength of 713 nm. In order to track the signal inside the channel fifteen perpendicular cross-sections have been taken along the channel. A maximum value in each cross-section, corresponding to the signal at a point positioned inside the channel, has been plotted versus its distance from the entrance to the waveguide along the channel (Fig. 4(c)). The maximum signal was found decreasing exponentially along the bent channel, with the fitting resulting in the SPP propagation length (inside the bent channel) equal to 4.4 μm, which is equivalent to a propagation loss of 1 dB/μm. Note that the SPP propagation length and loss evaluated at the same wavelength (713 nm) for a flat air-gold interface are ~ 32 μm and 0.14 dB/μm, respectively [1]. The measured propagation loss is substantial, but might still be acceptable for some practical applications in which main requirements are to the size of components used rather than insertion losses. On the other hand, long-rage SPP stripe waveguides exhibit rather low bend loss with very large (mm-sized) radii of curvature [14] that preclude their usage in compact devices.

One should explain the origin of an increase of the signal in the interval between 15 and 20 μm from the entrance to the waveguide (Fig. 4(c)). This can be related to the fact that the triangular lattice has ΓM orientation before the bend and ΓK orientation after the bend (since the lattice is 30-degree rotated) relative to the incident SPP beam (Fig. 2). While there is an inhibition of SPP propagation into the array for ΓM orientation, this is not the case to the same extent for ΓK orientation, resulting in the SPP penetration through the array and up to the channel.

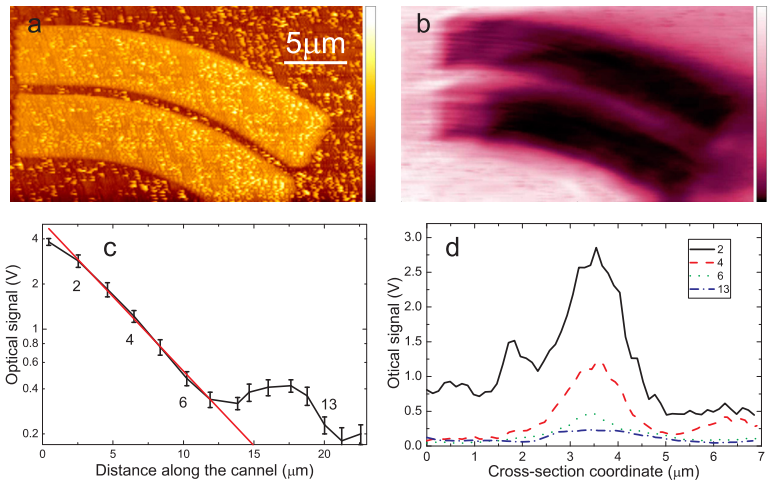

Fig. 4. (a) Shear-force topography and (b) near-field imaging of SPP interaction with the structure B obtained at the wavelength 713 nm. (c) Optical signal distribution along the channel, obtained by taking cross-sections perpendicular to the waveguide. (d) Four cross-sections (2nd, 4th, 6th, and 13th), taken at different distances from the entrance to the waveguide and showing the SPP field confinement.

Finally, to give an idea of SPP field confinement in the channel and signal levels, four from a series of fifteen cross-sections are plotted in Fig. 4(d) (namely, 2nd, 4th, 6th, and 13th, which are also marked by numbers in Fig. 4(c)). It should also be noted that the SPP field sustained

by the bent channel cannot be excited or replenished from below (from the side of the silica substrate) with the global illumination used here, because being directed perpendicular to the input face of the SPPBG structure it is parallel to the bent channel *only* at its input [10].

4. Numerical simulations

Following the experiment, we also calculated the electric field magnitude 300 nm above the air-gold interface for a SPP Gaussian beam incident on structures similar to A and B. The calculations are accomplished by making use of the Lippmann-Schwinger integral equation method and details can be found in ref. 13.

The first structure we analyzed was a set of 26×34 cylindrical scatterers (height $h = 60$ nm and radius $r = 68$ nm) arranged in ΓM-oriented triangular lattice with 475-nm period. The dimensions of the bumps have been chosen in a way to make their shape and volume similar to those composing structure A (Section 2). The calculations have been made for the wavelength range 700–900 nm. Figures 5(a)-(d) show results obtained for four different wavelengths. The dependence of the (theoretically estimated) intensity penetration depth on the wavelength is shown on Fig. 5(e) together with the experimental data, being the same as in Fig. 3(e). It is seen that there is overall agreement between the two dependencies as far as the SPPBG location is concerned, but the penetration depth observed experimentally is considerably larger than the theoretical one. The latter discrepancy can be accounted for by the circumstance that, in the experiment, the *whole* SPPBG structure was illuminated from the side of the silica substrate (global illumination) resulting in the background radiation produced by scattered field components. Such a background sets a limit on the smallest SNOM signal measured at the SPPBG structure influencing thereby the evaluation of the SPP penetration depth, especially at the position of the SPPBG.

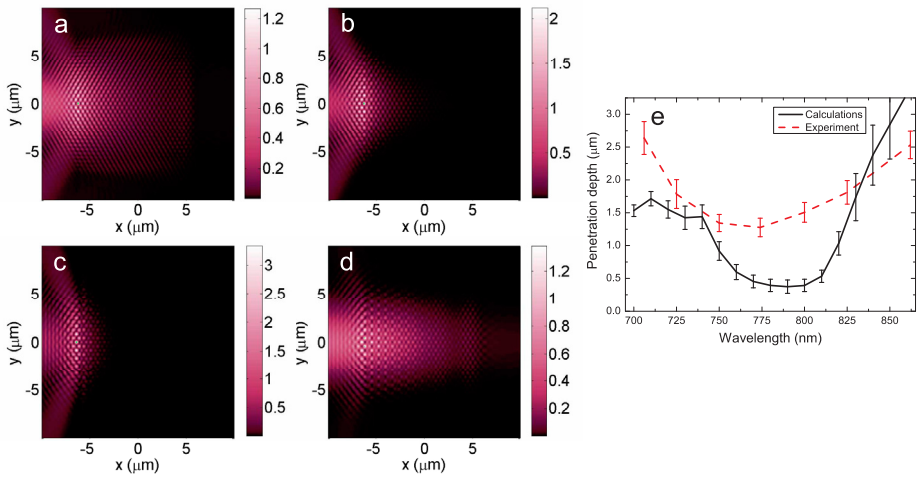

Fig. 5. (Movie 823 KB) Electric field magnitude distributions obtained by numerical simulations for the penetration of the Gaussian SPP beam into the ΓM-oriented triangular lattice (see text for details) for different wavelengths: (a) 720 nm, (b) 760 nm, (c) 800 nm, (d) 840 nm. (e) Wavelength dependence of the SPP penetration depth obtained from the calculated field distributions (solid line) together with the experimental data (dashed line).

The second structure is an adiabatically 30-degree rotated ΓM triangular lattice with a channel formed by removing four lines of scatterers. The structure has the same size and the radius of curvature of the bend as in the experiment and is composed of cylindrical scatterers (height

$h = 60$ nm and radius $r = 86$ nm), whose dimensions have been chosen to emulate the shape and volume of the bumps of structure B (Section 2). Figures 6(a)-(d) show the electric field magnitude distributions obtained with this structure at four wavelengths, particularly Fig. 6(a) is produced at the wavelength of 720 nm, which is closest to that used in the experiment (713 nm). One should note that the figures obtained are not directly comparable with Fig. 4(b) because we used the global SPP excitation in the experiment (Section 3). One can, however, compare the guiding capability of that kind of structure and it is clearly seen on Fig. 6(a) that at the wavelength of 720 nm a reasonable result can be obtained, which has been also observed in the experiment. It appears, nevertheless, that the best guiding should be provided by this structure at the wavelength of 840 nm, which roughly corresponds to the SPPBG wavelength that we would expect for this size of cylindrical scatterers (which is larger than that used in the simulations shown in Fig. 5). We have evaluated the SPP transmission through the bent waveguide (in percent) versus wavelength (Fig. 6(e)) and found the existence of a clear peak around the wavelength of 840 nm. The further increase in the transmission at longer wavelengths is due to the SPP propagation (and scattering) directly through the structure for the wavelengths being on the long-wavelength side of the SPPBG. It should be borne in mind that the transmission shown in Fig. 6(e) was estimated by averaging the field intensity in a small box placed at the exit of the bend and normalizing with the intensity of the incident SPP, and reflects thereby not only the SPP bend and propagation loss (in the channel) but also the coupling loss. The latter loss channel is difficult (though not impossible) to evaluate as it depends upon the overlap between the incident SPP field and the SPP mode field sustained by the channel [13].

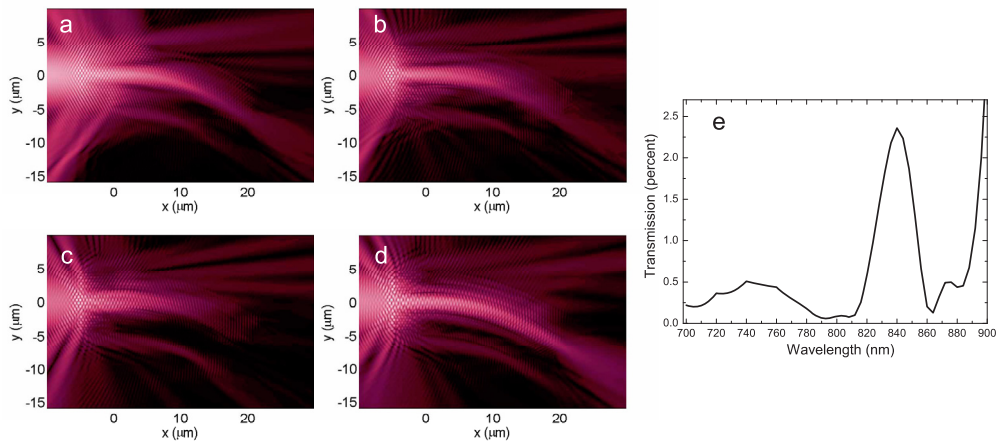

Fig. 6. (Movie 1.02 MB) Theoretical electric field magnitude distributions of the Gaussian SPP beam interaction with the adiabatic bend of the ΓM-oriented lattice with the channel inside (structure B on Fig. 2(b)). Images obtained for different wavelengths: (a) 720 nm, (b) 760 nm, (c) 800 nm, (d) 840 nm. (e) Estimated transmission of the optical signal through the waveguide plotted versus SPP wavelength.

5. Conclusion

To summarize, we have investigated the SPP excitation and interaction with periodic triangular arrays of gold bumps within the wavelength range of 700–860 nm. We have characterized the inhibition of SPP propagation into the periodic structures due to the SPPBG effect. The SPP propagation along a 30° bent channel obtained by an adiabatic rotation of the triangular

lattice of scatterers was observed at the wavelength 713 nm, showing a propagation loss at the level ~ 1 dB/μm. We have also presented the corresponding numerical simulations of SPP propagation in and scattering by periodic arrays of cylindrical scatterers similar to those used in the experiment, which are in reasonable agreement with the experimental observations. We believe that the presented results are useful, in general, for the further understanding of various SPPBG phenomena and, in particular, for finding the optimum parameters of a given adiabatic bend to minimize the loss incurred. Finally, we would like to remark that, similar to recent developments within conventional photonic crystal structures [19, 20], one might expect very interesting applications of the SPPBG structures to be found apart from compact bending and splitting, e.g., in the areas of slow light control and super-prism-based filtering, utilizing thereby very strong dispersion present in BG structures.

Acknowledgments

The authors acknowledge the help of K. Leosson (University of Iceland) in fabrication of periodic gold nanostructures investigated in this work. This work was partially supported by the European Network of Excellence, PLASMO-NANO-DEVICES (FP6-2002-IST-1-507879).

Chapter 2

SP focusing with parabolic nanoparticle chains

Surface plasmon polariton beam focusing with parabolic nanoparticle chains

Ilya P. Radko and Sergey I. Bozhevolnyi

Department of Physics and Nanotechnology, Aalborg University, Skjernvej 4A, DK-9220 Aalborg Øst, Denmark

ilya@physics.aau.dk

Andrey B. Evlyukhin

Department of Physics and Applied Mathematics, Vladimir State University, Gorkii str. 87, 600000 Vladimir, Russia

Alexandra Boltasseva

COM·DTU, Department of Communications, Optics & Materials, Nano·DTU, Ørsteds Plads, Technical University of Denmark, Bldg. 345v, DK-2800 Kongens Lyngby, Denmark

Abstract: We report on the focusing of surface plasmon polariton (SPP) beams with parabolic chains of gold nanoparticles fabricated on thin gold films. SPP focusing with different parabolic chains is investigated in the wavelength range of 700–860 nm, both experimentally and theoretically. Mapping of SPP fields is accomplished by making use of leakage radiation microscopy, demonstrating robust and efficient SPP focusing into submicron spots. Numerical simulations based on the Green's tensor formalism show very good agreement with the experimental results, suggesting the usage of elliptical corrections for parabolic structures to improve their focusing of slightly divergent SPP beams.

OCIS codes: (240.6680) Surface plasmons; (250.5300) Photonic integrated circuits.

References and links

1. R. H. Ritchie, "Plasma losses by fast electrons in thin films," Phys. Rev. **106,** 874–881 (1957).
2. C. J. Powell and J. B. Swan, "Effect of oxidation on the characteristic loss spectra of aluminium and magnesium," Phys. Rev. **118,** 640–643 (1960).
3. W. L. Barnes, A. Dereux, and T. W. Ebbesen, "Surface plasmon subwavelength optics," Nature (London) **424,** 824–830 (2003).
4. S. A. Maier and H. A. Atwater, "Plasmonics: Localization and guiding of electromagnetic energy in metal/dielectric structures," J. Appl. Phys. **98,** 1–10 (2005).
5. E. Devaux, T. W. Ebbesen, J.-C. Weeber, and A. Dereux, "Launching and decoupling surface plasmons via micro-gratings," Appl. Phys. Lett. **83,** 4936–4938 (2003).
6. H. Ditlbacher, J. R. Krenn, A. Hohenau, A. Leitner, and F. R. Aussenegg, "Efficiency of local light-plasmon coupling," Appl. Phys. Lett. **83,** 3665–3667 (2003).
7. J.-C. Weeber, J. R. Krenn, A. Dereux, B. Lamprecht, Y. Lacroute, and J. P. Goudonnet, "Near-field observation of surface plasmon polariton propagation on thin metal stripes," Phys. Rev. B **64,** 045411 (2001).
8. S. I. Bozhevolnyi, J. Erland, K. Leosson, P. M. W. Skovgaard, and J. M. Hvam, "Waveguiding in surface plasmon polariton band gap structures," Phys. Rev. Lett. **86,** 3008–3011 (2001).
9. S. I. Bozhevolnyi, V. S. Volkov, E. Devaux, and T. W. Ebbesen, "Channel plasmon-polariton guiding by subwavelength metal grooves," Phys. Rev. Lett. **95,** 046802 (2005).
10. H. Ditlbacher, J. R. Krenn, G. Schider, A. Leitner, and F. R. Aussenegg, "Two-dimensional optics with surface plasmon polaritons," Appl. Phys. Lett. **81,** 1762–1764 (2002).

11. A. Drezet, A. Hohenau, A. L. Stepanov, H. Ditlbacher, B. Steinberger, F. R. Aussenegg, A. Leitner, and J. R. Krenn, "Surface plasmon polariton Mach-Zehnder interferometer and oscillation fringes," Plasmonics **1,** 141–145 (2006).
12. S. I. Bozhevolnyi, V. S. Volkov, E. Devaux, J.-Y. Laluet, and T. W. Ebbesen, "Channel plasmon subwavelength waveguide components including interferometers and ring resonators," Nature (London) **440,** 508–511 (2006).
13. T. Nikolajsen, K. Leosson, and S. I. Bozhevolnyi, "Surface plasmon polariton based modulators and switches operating at telecom wavelengths," Appl. Phys. Lett. **85,** 5833–5835 (2004).
14. A. V. Krasavin, K. F. MacDonald, N. I. Zheludev, A. V. Zayats, "High-contrast modulation of light with light by control of surface plasmon polariton wave coupling," Appl. Phys. Lett. **85,** 3369–3371 (2004).
15. Z. Liu, J. M. Steele, W. Srituravanich, Y. Pikus, C. Sun, and X. Zhang, "Focusing surface plasmons with a plasmonic lens," Nano Lett. **5,** 1726–1729 (2005).
16. L. Yin, V. K. Vlasko-Vlasov, J. Pearson, J. M. Hiller, J. Hua, U. Welp, D. E. Brown, and C. W. Kimball, "Subwavelength focusing and guiding of surface plasmons," Nano Lett. **5,** 1399–1402 (2005).
17. Z. Liu, J. M. Steele, H. Lee, X. Zhang, "Tuning the focus of a plasmonic lens by the incident angle," Appl. Phys. Lett. **88,** 171108 (2006).
18. A. Drezet, A. L. Stepanov, H. Ditlbacher, A. Hohenau, B. Steinberger, F. R. Aussenegg, A. Leitner, and J. R. Krenn, "Surface plasmon propagation in an elliptical corral," Appl. Phys. Lett. **86,** 074104 (2005).
19. A. B. Evlyukhin, S. I. Bozhevolnyi, A. L. Stepanov, J. R. Krenn, "Splitting of a surface plasmon polariton beam by chains of nanoparticles," Appl. Phys. B **84,** 29–34 (2006).
20. B. Hecht, H. Bielefeldt, L. Novotny, Y. Inouye, and D. W. Pohl, "Local excitation, scattering, and interference of surface plasmons," Phys. Rev. Lett. **77,** 1889–1892 (1996).
21. A. Bouhelier, Th. Huser, H. Tamaru, H.-J. Güntherodt, D. W. Pohl, F. I. Baida and D. Van Labeke, "Plasmon optics of structured silver films," Phys. Rev. B **63,** 155404 (2001).
22. A. B. Evlyukhin and S. I. Bozhevolnyi, "Surface plasmon polariton guiding by chains of nanoparticles," Laser Phys. Lett. **3,** 396–400 (2006).
23. T. Søndergaard and S. I. Bozhevolnyi, "Vectorial model for multiple scattering by surface nanoparticles via surface polariton-to-polariton interactions," Phys. Rev. B **67,** 165405 (2003).

1. Introduction

Plasmonic components operating with surface plasmon polaritons (SPPs), due to the hybrid nature of the latter, exhibit the potential of combining strong sides of electronic (nm-size confinement) and photonic (large bandwidth) components. The possibility for the electron charges on a metal boundary to perform coherent fluctuations has been demonstrated long ago [1, 2]. Nevertheless, it was not until the last decade that the interest to SPPs greatly increased [3, 4] due to the development of nanofabrication techniques, such as electron-beam lithography and ion-beam milling, and nano-optical characterization tools, such as near-field optical microscopy, as well as due to the emergence of accurate quantitative electromagnetic simulation methods.

In order to realize integrated plasmonic devices one has to first develop approaches for SPP launching [5, 6] and waveguiding [7-9], as well as to realize basic SPP components, such as interferometers [10-12], modulators and switches [13, 14]. One of the important functionalities that should be mastered in SPP micro-optics is the delivery of intense SPP fields to a particular point within an integrated circuit, a bio-sensor or a data storage device. Several configurations have been suggested for this purpose including SPP excitation on circular structures [15-17] and exploiting of elliptical corrals [18]. For circular structures to perform efficiently, a very wide incident beam exciting converging SPPs should be used (in order to cover a large part of circumference) with only a small part of the beam contributing to the SPP excitation. In the elliptical configuration, SPP rays arrive to the focal point after propagating over considerable distances (much longer than the distance between the excitation and focusing points) and thereby being notably attenuated upon the propagation.

One can tackle the issue of SPP delivery to a particular surface point by separating the SPP excitation and focusing steps. Thus, local and efficient SPP coupling can be achieved with a metal ridge being illuminated at normal incidence, a process that results in slightly diverging SPP beams propagating away from the ridge [6]. One can then further focus the excited SPP beams with parabolic chains of nanoparticles, utilizing the circumstance that nanoparticle

chains represent efficient SPP reflectors for oblique angles of incidence [19]. Here we present the results of experimental and theoretical investigations of SPP beam focusing by means of nanoparticles arranged in different parabolic structures having very small focal distances (from 63 to 250 nm). With these structures, we exploit the advantage of high SPP reflectivity at oblique angles while minimizing the SPP travelling path lengths and, thereby, the incurred propagation losses.

2. Experimental results

The structures we consider in this work were fabricated on a 50-nm-thick gold film deposited on a quartz substrate using electron-beam lithography, evaporation of another 50-nm-thick gold layer and subsequent lift-off. Thus fabricated parabolic chains consisted of 50-nm-high gold bumps having the lateral cross sections in the form of rounded squares [Fig. 1(a)] with the width varying from 160 to 250 nm for different structures. The centre-to-centre distance between bumps in the chains was also varying (from 250 to 320 nm) for different structures. It should be noted, that the fabricated structures included those in which the bump width of 250 nm was equal to their (centre-to-centre) separation, i.e. those representing continuous lines of 250 nm width. Five different parabolic structures corresponding to the focal distances of 250, 175, 125, 90 and 63 nm were fabricated and investigated. Hereafter we refer to these structures as parabola 1 through 5. Each parabola extended over 50 μm along the SPP propagation direction.

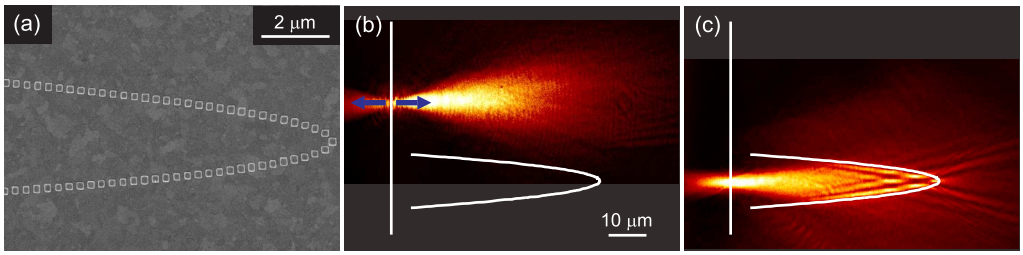

Fig. 1. (a) SEM image of the outmost part of the parabolic chain structure with the focal distance of 63 nm. (b) Free SPP mode excited on a 100-nm-wide stright (gold) ridge. SPP propagation directions are shown by arrows. (c) SPP excited on a 100-nm-wide stright (gold) ridge in front of the parabolic structure which modifies the right-propagation part of the mode.

A 100-nm-wide straight (gold) ridge was fabricated perpendicular to each parabola's axis of symmetry at the distance of 5 μm away from its entrance (i.e. 55 μm away from its apex) in order to facilitate the SPP excitation. The SPP excitation was achieved by direct illumination of the straight ridge with a tuneable (700–860 nm) laser beam focused to a $\sim$ 3-μm-diameter spot and polarized perpendicular to the ridge. Figure 1(b) represents a free SPP mode (i.e. propagating along smooth gold surface without any parabolic structure on it) excited on the straight ridge. While investigating parabolic structures, the excitation spot was adjusted so that the excited SPP beam propagated from the ridge inside parabola's branches towards its vertex [Fig. 1(c)]. Mapping of SPP fields was accomplished by making use of leakage radiation microscopy (LRM) [20, 21], a technique which is well established and described in detail elsewhere [18]. Note that all further experimental LRM images of the SPP intensity distributions are presented in the way that the left image border coincides with the excitation ridge position. Typical SPP intensity maps recorded for five different parabolic structures are displayed in Fig. 2. In this particular case, the laser excitation wavelength of 800 nm was used, and the parabolic chains consisted of 250-nm-wide bumps separated by the distance of 320 nm.

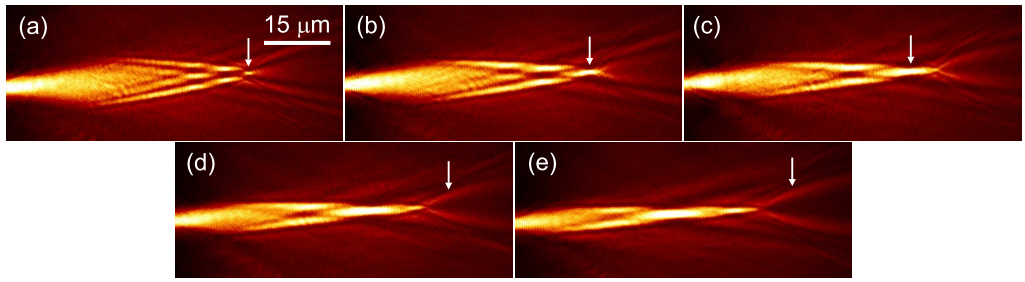

Fig. 2. LRM images ($\lambda_0 = 800$ nm) of SPP beam propagation inside parabolic structures of nanoparticles (width = 250 nm, centre-to-centre separation = 320 nm) with the focal distances of (a) 250 nm (parabola 1), (b) 175 nm (parabola 2), (c) 125 nm (parabola 3), (d) 90 nm (parabola 4), (e) 63 nm (parabola 5). Arrows indicate the locations of cross sections shown in Fig. 3.

It is seen that all parabolas are rather efficient in reflecting the SPP beam with their branches and thereby confining the excited SPP waves (Fig. 2). The resulting SPP intensity distributions are however different for different parabolas. While parabolas 1–3 produce a bright spot close to the vertex, whose dimensions increase from parabola 1 to 3 [Figs. 2(a)-2(c), parabolas 4 and 5 do not form a clear spot at their vertices but rather split the incident SPP beam into two beams propagating further away [Figs. 2(d), 2(e)]. This effect is most pronounced with parabola 5.

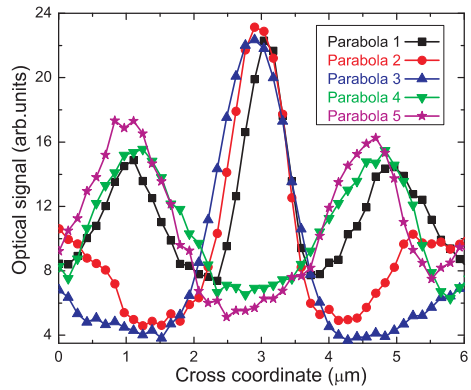

Fig. 3. Normalized with respect to the SPP beam propagation distance cross sections of LRM images shown in Figs. 1(b)-1(f).

In order to quantitatively characterize the focusing ability of parabolas 1–3 and the splitting ability of parabolas 4 and 5, we considered cross sections through the maximum intensity level of bright spots for parabolas 1–3 and 5 μm away from the parabola vertex for parabolas 4 and 5 (Fig. 3). To eliminate the influence of propagation losses, the signal was normalized with respect to the SPP beam propagation distance taking also into account the SPP beam divergence. The evolution of the SPP intensity distributions across the bright spots formed by parabolas 1–3 can be accounted for by the decrease in the effective aperture from parabola 1 to 3. The SPP splitting, which is especially pronounced with parabola 5, is a rather complicated phenomenon with both the SPP reflection by parabola branches and the SPP scattering along these branches (i.e., along the nanoparticle chains) contributing to the resultant splitting effect. Given the cross sections shown in Fig. 3, one can characterize the full-width-at-half-maximum (FWHM) of the central (parabolas 1–3) and side (parabolas 4 and 5) peaks (Table 1) along

with the corresponding contrast levels determined as $10\log(P_{max}/P_{min})$, P_{max} and P_{min} being the maximum and minimum signal levels in the considered distributions (Fig. 3).

Parabola	1	2	3	4	5
Contrast (dB)	4.9	7.1	7.9	3.8	5.3
FWHM (μm)	0.7	0.9	1.2	1.4	1.6

Table 1. Characteristics calculated from the SPP intensity cross sections shown in Fig. 3

The SPP focusing by parabolic chains of nanoparticles is based on the SPP *reflection* and, therefore, expected to be stable and robust with respect to variations in both nanoparticle parameters and radiation wavelength. Indeed, the performance of parabolic structures characterized with 12 different combinations of bump width and separation was found quite similar and without clear influence of either of the parameters. The SPP intensity distributions imaged with the LRM remained similar also when changing the excitation wavelength from 700 to 860 nm, though the effect of increasing (with the wavelength) the SPP propagation length was clearly visible, resulting in the SPP intensity increase at parabola vertices (Fig. 4).

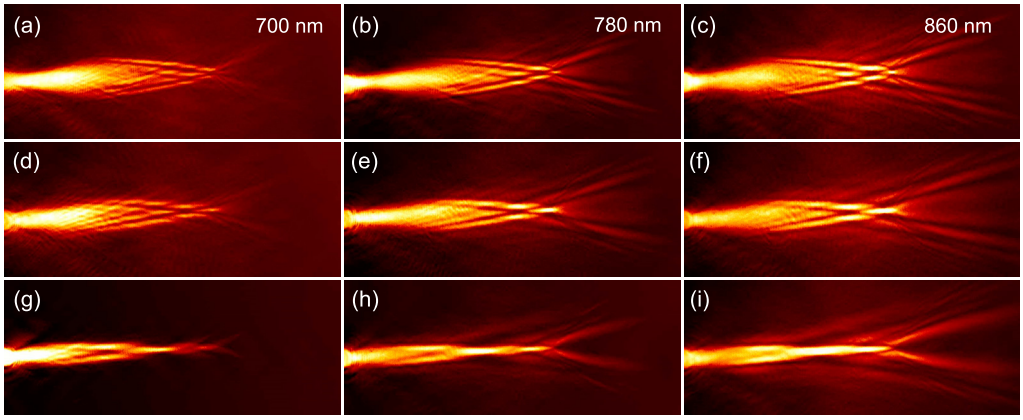

Fig. 4. LRM images of SPP beam propagation inside (a-c) parabola 1, (d-f) parabola 2, and (g-i) parabola 5 for different wavelengths of SPP excitation: (a, d, g) 700, (b, e, h) 780, and (c, f, i) 860 nm.

3. Numerical simulations

The SPP beam propagation inside parabolic structures has been numerically simulated by making use of the total Green's tensor formalism and the dipole approximation for multiple SPP scattering by nanoparticles [19, 22, 23]. The bumps forming parabolic chains were approximated by spherical particles considered as point-dipole scatterers, which were characterized with isotropic free-space polarizability obtained in the long-wavelength approximation. First the dipole moments of particles illuminated with a Gaussian SPP beam were calculated self-consistently, and then the total electric field distribution was determined above the sample surface (using in both cases the total Green's dyadic) [22]. The radius of the particles was not a crucial parameter and chosen to be equal to 50 nm judging from the overall similarity between the simulated field intensity distributions and the experimental LRM images. Very good agreement between the LRM images and the intensity distributions was observed for all considered parabolic structures [cf. Figs. 5(a) and 5(b)]. Note that the simulated and experimental images

have different contrasts due to the nonlinear sensitivity of a CCD camera used in our experiments and that otherwise all features are perfectly reproduced, confirming the validity of the developed numerical approach.

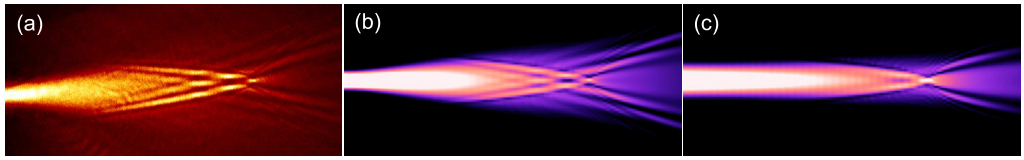

Fig. 5. (a) LRM image of SPP beam propagation inside parabola 1, and (b, c) the electric field intensity distributions calculated at the height of 150 nm above the surface plane for the same parabola with the SPP beam diameter being (b) 3 and (c) 6 μm. The excitation wavelength is 800 nm.

We have further used the developed modelling tool to get better insight in the underlying physics of the SPP focusing. In the approximation of geometrical optics, parabolic reflectors are ideal for the focusing parallel light beams. In our experiments, we have used a 3-μm-wide light spot for the SPP excitation resulting in slightly divergent SPP beams. We believe that this divergence constituted the main reason for the aforementioned complicated effects in the SPP focusing with different parabolas (Fig. 2). Indeed, our simulations of the SPP focusing of a 6-μm-wide SPP beam demonstrated a significant improvement in the quality of SPP focusing [cf. Figs. 5(b) and 5(c)]. In practice, however, an increase in the excitation spot size is not desirable since it would most probably result in a decrease of the SPP excitation efficiency (due to a decrease in the overlap between the excitation spot and a ridge). We would rather suggest to maintain the excitation spot size and to improve the SPP focusing by introducing elliptical corrections for parabolic structures, since elliptical structures are best suited for the focusing of divergent beams [18].

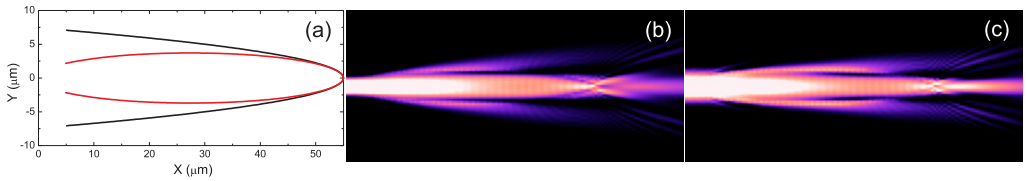

Fig. 6. (a) Geometry of the considered elliptical structure along with that of parabola 1, and (b, c) the electric field intensity distributions calculated for the elliptical structure focusing with the SPP beam diameter being (b) 3 and (c) 6 μm. The excitation wavelength is 800 nm.

We have tested this idea by considering the SPP focusing with the elliptical structure corresponding to parabola 1 at the focusing end, i.e., with its first focus coinciding with that of the parabola, and having its second focus at the point of SPP excitation, i.e., 55 μm away from the vertex [Fig. 6(a)]. Modelling of the SPP focusing conducted for a 3- and 6-μm-wide SPP beam showed a significant improvement in the focusing quality for the 3-μm-wide beam (cf. 5(b) and 6(b)) and, somewhat surprisingly, a deterioration of the focusing for the 6-μm-wide beam (cf. 5(c) and 6(c)). Note that both considered beams are divergent (though with different rates) from the same focus point of the elliptical structure. The difference in their focusing can be explained by considering their waist lengths estimated as ~ 9 and 35 μm, respectively. The wide SPP beam remains therefore nearly parallel while propagating in the focusing structure and is therefore better focused with a parabolic chain. One should therefore use arguments of geometrical optics with care, when designing SPP focusing structures, and supplement such a

design with accurate modelling.

4. Conclusion

Summarizing, we have realized the efficient SPP focusing with parabolic chains of gold nanoparticles. The influence of excitation wavelength and geometrical system parameters has been investigated with the help of LRM imaging, demonstrating good stability and robustness of the focusing effect. Numerical simulations based on the Green's tensor formalism have shown very good agreement with the experimental results, suggesting the usage of elliptical corrections for parabolic structures to improve their focusing of slightly divergent SPP beams. The SPP splitting effect observed with narrow parabolic structures might also be found useful in SPP micro-optics.

Acknowledgments

Two of the authors (I.P.R. and S.I.B.) acknowledge financial support from the Danish Technical Research Council, Contract No. 26-04-0158, and from the European Network of Excellence, PLASMO-NANO-DEVICES (FP6-2002-IST-1-507879). A.B.E. is grateful to the Russian Foundation for Basic Research, Grant No. 06-02-16443 for the financial support. A.B. acknowledges support from the Danish Technical Research Council, "Talent project" grant No. 26-04-0268.

Chapter 3

Refracting SPs with nanoparticle arrays

Refracting surface plasmon polaritons with nanoparticle arrays

Ilya P. Radko,[1*] Andrey B. Evlyukhin,[2] Alexandra Boltasseva,[3] and Sergey I. Bozhevolnyi[1,4]

[1] *Department of Physics and Nanotechnology, Aalborg University, Skjernvej 4A, DK-9220 Aalborg Øst, Denmark*

[2] *Department of Physics and Applied Mathematics, Vladimir State University, Gorkii str. 87, 600000 Vladimir, Russia*

[3] *COM·DTU, Department of Communications, Optics & Materials, Nano·DTU, Ørsteds Plads, Technical University of Denmark, Bldg. 345v, DK-2800 Kongens Lyngby, Denmark*

[4] *Institute of Sensors, Signals and Electrotechnics, University of Southern Denmark, Niels Bohrs Allé 1E, DK-5230 Odense M, Denmark*

[*] *Corresponding author: ilya@nano.aau.dk*

Abstract: Refraction of surface plasmon polaritons (SPPs) by various structures formed by a 100-nm-period square lattice of gold nanoparticles on top of a gold film is studied by leakage radiation microscopy. SPP refraction by a triangular-shaped nanoparticle array indicates that the SPP effective refractive index increases inside the array by a factor of ~ 1.08 (for the wavelength 800 nm) with respect to the SPP index at a flat surface. Observations of SPP focusing and deflection by circularly shaped areas as well as SPP waveguiding inside rectangular arrays are consistent with the SPP index increase deduced from the SPP refraction by triangular arrays. The SPP refractive index is found to decrease slightly for longer wavelengths within the wavelength range of 700–860 nm. Modeling based on the Green's tensor formalism is in a good agreement with the experimental results, opening the possibility to design nanoparticle arrays for specific applications requiring in-plane SPP manipulation.

OCIS codes: (240.6680) Surface plasmons; (160.4236) Nanomaterials; (250.5403) Plasmonics.

References and links

1. R. Zia, J. A. Schuller, A. Chandran, and M. L. Brongersma, "Plasmonics: the next chip-scale technology," Materials Today **9,** 20–27 (2006).
2. W. L. Barnes, A. Dereux, and T. W. Ebbesen, "Surface plasmon subwavelength optics," Nature (London) **424,** 824–830 (2003).
3. J.-C. Weeber, J. R. Krenn, A. Dereux, B. Lamprecht, Y. Lacroute, and J. P. Goudonnet, "Near-field observation of surface plasmon polariton propagation on thin metal stripes," Phys. Rev. B **64,** 045411 (2001).
4. S. I. Bozhevolnyi, J. Erland, K. Leosson, P. M. W. Skovgaard, and J. M. Hvam, "Waveguiding in surface plasmon polariton band gap structures," Phys. Rev. Lett. **86,** 3008–3011 (2001).
5. H. Ditlbacher, J. R. Krenn, G. Schider, A. Leitner, and F. R. Aussenegg, "Two-dimensional optics with surface plasmon polaritons," Appl. Phys. Lett. **81,** 1762–1764 (2002).
6. A. Drezet, A. Hohenau, A. L. Stepanov, H. Ditlbacher, B. Steinberger, F. R. Aussenegg, A. Leitner, and J. R. Krenn, "Surface plasmon polariton Mach-Zehnder interferometer and oscillation fringes," Plasmonics **1**, 141–145 (2006).

7. S. C. Kitson, W. L. Barnes, and J. R. Sambles, "Full photonic band gap for surface modes in the visible," Phys. Rev. Lett. **77,** 2670–2673 (1996).
8. T. Søndergaard and S. I. Bozhevolnyi, "Theoretical analysis of finite-size surface plasmon polariton band-gap structures," Phys. Rev. B **71,** 125429 (2005).
9. T. Søndergaard, S. I. Bozhevolnyi, and A. Boltasseva, "Theoretical analysis of ridge gratings for long-range surface plasmon polaritons," Phys. Rev. B **73,** 045320 (2006).
10. A. Hohenau, J. R. Krenn, A. L. Stepanov, A. Drezet, H. Ditlbacher, B. Steinberger, A. Leitner, and F. R. Aussenegg, "Dielectric optical elements for surface plasmons," Opt. Lett. **30,** 893–895 (2005).
11. B. Steinberger, A. Hohenau, H. Ditlbacher, A. L. Stepanov, A. Drezet, F. R. Aussenegg, A. Leitner, and J. R. Krenn, "Dielectric stripes on gold as surface plasmon waveguides," Appl. Phys. Lett. **88,** 094104 (2006).
12. T. Holmgaard, S. I. Bozhevolnyi, L. Markey, and A. Dereux, "Dielectric-loaded surface plasmon-polariton waveguides at telecommunication wavelengths: Excitation and characterization," Appl. Phys. Lett. **92,** 011124 (2008).
13. S. A. Maier, M. D. Friedman, P. E. Barclay, and O. Painter, "Experimental demonstration of fiberaccessible metal nanoparticle plasmon waveguides for planar energy guiding and sensing," Appl. Phys. Lett. **86,** 071103 (2005).
14. B. Hecht, H. Bielefeldt, L. Novotny, Y. Inouye, and D. W. Pohl, "Local excitation, scattering, and interference of surface plasmons," Phys. Rev. Lett. **77,** 1889–1892 (1996).
15. A. Bouhelier, Th. Huser, H. Tamaru, H.-J. Güntherodt, D. W. Pohl, F. I. Baida, and D. Van Labeke, "Plasmon optics of structured silver films," Phys. Rev. B **63,** 155404 (2001).
16. A. Drezet, A. Hohenau, A. L. Stepanov, H. Ditlbacher, B. Steinberger, N. Galler, F. R. Aussenegg, A. Leitner, and J. R. Krenn, "How to erase surface plasmon fringes," Appl. Phys. Lett. **89,** 091117 (2006).
17. J.-Y. Laluet, E. Devaux, C. Genet, T. W. Ebbesen, J.-C. Weeber, and A. Dereux, "Optimization of surface plasmons launching from subwavelength hole arrays: modelling and experiments," Opt. Express **15,** 3488–3495 (2007), http://www.opticsinfobase.org/abstract.cfm?URI=oe-15-6-3488.
18. H. Kogelnik and V. Ramaswamy, "Scaling rules for thin-film optical waveguides," Appl. Opt. **13,** 1857–1862 (1974).
19. H. Kogelnik and H. P. Weber, "Rays, stored energy, and power flow in dielectric waveguides," J. Opt. Soc. Am. **64,** 174–185 (1974).
20. A. B. Evlyukhin, S. I. Bozhevolnyi, A. L. Stepanov, and J. R. Krenn, "Splitting of a surface plasmon polariton beam by chains of nanoparticles," Appl. Phys. B **84,** 29–34 (2006).
21. A. B. Evlyukhin and S. I. Bozhevolnyi, "Surface plasmon polariton guiding by chains of nanoparticles," Laser Phys. Lett. **3,** 396–400 (2006).
22. T. Søndergaard and S. I. Bozhevolnyi, "Vectorial model for multiple scattering by surface nanoparticles via surface polariton-to-polariton interactions," Phys. Rev. B **67,** 165405 (2003).

1. Introduction

Integrated plasmonics operates with surface plasmon polaritons (SPPs) and is hoped to substitute integrated optics, which suffers from its components being bulkier than electronic ones, but in turn much faster than those [1,2]. The success of development of this relatively young branch of optics depends on the variety of active and passive components available for the integration. Plasmonics, having features of both photonics and electronics, in terms of operational elements, bears more resemblance to optics since Bragg mirrors, waveguides, beam splitters, and interferometers are used [3–6]. So, the vast majority of elements used in plasmonics have their ancestors in integrated optics.

One of the most efficient and widely used means to control the propagation of SPPs is the exploiting of a band-gap, or Bragg-grating effect [4,5,7]. Although flexible and suitable for many applications, those structures suffer from considerable out-of-plane scattering [8], which gets significantly smaller for the wavelength longer than the band gap [9]. Another elegant method for controlling the SPP propagation is borrowed from conventional optics. It introduces elements of higher refractive index to define a spatial change in the optical path length [10]. Hohenau *et al.* use a silica layer (below the cutoff thickness of the guided modes in silica) on top of a metal surface to shift the SPP dispersion relation. This method allows simple structures like lenses and prisms to be made. The possibility of effective and subwavelength SPP waveguiding in such structures has recently been demonstrated at both near-infrared [11] and telecom [12] wavelengths. Finally, the realization of fiber-accessible plasmon waveguides composed of a

two-dimensional array of metal nanoparticles on a silicon membrane exploits the periodicity of the structure to tailor the dispersion relation of the SPP modes to match the refractive index of the waveguide with that of the silica fiber [13].

In this work we utilize a similar principle: a 100-nm-period square lattice of gold nanoparticles on top of a gold film is used to form variously shaped structures. The SPP waves propagating along the surface inside the periodic arrays experience an increase in the effective refractive index (ERI) with respect to that of a flat surface SPP. In this case, since the period is considerably smaller than the wavelength, out-of-plane scattering is relatively weak [9]. We show that those structures possess the ERI of about 1.08 and, if shaped appropriately, feature properties of prisms, lenses, and optical-fiber waveguides.

2. Structures and experimental technique

The parameters of all studied periodic arrays are identical, only the shape is different. Arrays are based on 50-nm-high gold bumps (rounded squares with the width of about 50–60 nm) arranged in a square lattice with a period of 100 nm. The structures were fabricated by electron-beam lithography on a resist layer spun on top of a 50-nm-thick gold film on a quartz substrate, evaporation of a second gold layer, and subsequent lift-off. A typical fabricated periodic pattern is shown in Fig. 1(a).

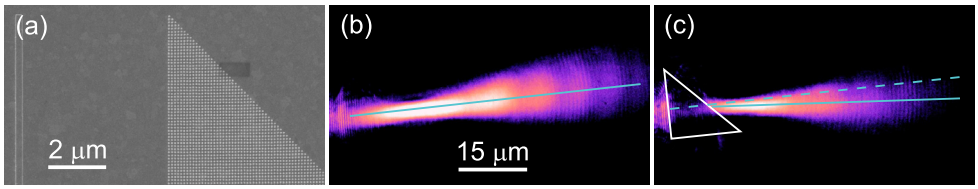

Fig. 1. (a) Scanning electron microscope image of the periodic (triangular shaped) structure along with the excitation ridge. (b) LRM image of the free SPP mode excited on a 180-nm-wide straight (gold) ridge. SPP propagation direction is shown by a solid line. (c) LRM image of the SPP beam propagating through a triangular-shaped periodic structure (same as in Fig. 1(a)). SPP propagation direction is shown by a solid line. Dashed line shows the propagation direction of the SPP beam in Fig. 1(b). Note that all the experimental LRM images of the SPP intensity distributions are presented so that the left image border coincides with the excitation ridge position.

To launch SPPs, we directly illuminated a 180-nm-wide straight gold ridge by a focused laser beam. The ridge was placed 5 μm away from each structure (Fig. 1(a)). We used tuneable (wavelength range of 700–860 nm) Ti:Sapphire laser to make a 5-μm-diameter spot polarized perpendicular to the ridge, thereby defining the direction of the SPP propagation. Note that the divergence of the excited SPP beam is determined mainly by the diffraction and can roughly be estimated as λ/d, where λ is the SPP wavelength and d is the waist diameter of the SPP Gaussian beam. With the 5-μm-diameter waist of the beam, the divergence is appreciable, whereas it is more convenient to have a narrower, self-focusing beam when determining the direction of SPP propagation. We used a defocused excitation in this case. Normally, one would focus the laser beam by means of an objective onto the sample surface, so that the waist position of an emerging SPP Gaussian beam coincides with its excitation point. However, if one moves the focal plane of the objective behind the sample's surface, the SPP beam is excited with the defocused (converging) Gaussian laser beam and continues to converge upon excitation. This method was used to narrow down the SPP beam.

Mapping of the SPP fields was accomplished via leakage radiation microscopy (LRM) [14,15], a well established technique described in details elsewhere [16].

3. Experimental results

Prism effect. First, we show the refractive property of a nanoparticle array by demonstrating a prism effect. For that purpose, a triangular array of bumps was investigated (Fig. 1(a)). It is an isosceles right-angled triangle placed with one of its catheti parallel to the excitation ridge. Figure 1(b) shows the propagation of a reference beam on a smooth gold film without any structure. Note that the sample was initially rotated several degrees counter clockwise, so that the excitation ridge was not exactly vertical, therefore the reference SPP beam looks as propagating to the right and a bit upwards. Note also that the defocused laser beam was used here to excite SPPs as described above. That narrows the SPP beam allowing determining its propagation direction more precisely. Figure 1(c) shows the SPP beam passing through the structure, which is denoted by the white triangle. The image is obtained at the free-space wavelength $\lambda_0 = 800$ nm. Inside the structure the beam is poorly visible. This is due to the array of bumps, which makes the average gold layer in that area thicker and thus the leakage of SPP power into the substrate (where it is collected by an objective) lower. Passing through the triangular array of bumps, the SPP beam is declined towards the base of that structure as it happens with a light beam passing through a glass prism. The propagation direction of the reference SPP beam is shown by the dashed line in Fig. 1(c), and the magnitude of deflection is easily seen. We estimated the deflection angle to be approximately 4.7 degrees, which gave the value of ERI of the structure to be equal to $n_{\text{eff}} \approx 1.08$.

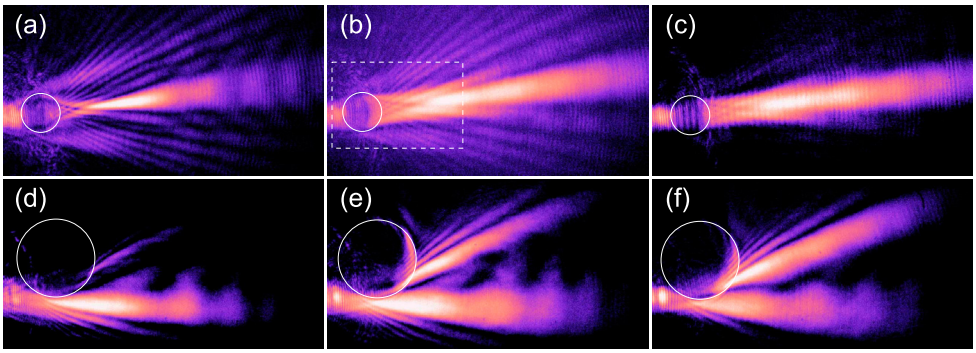

Fig. 2. LRM image of a SPP beam scattered by (a–c) a 7.5-μm-diameter circular-shaped periodic structure and (d–f) a 15-μm-diameter circular-shaped periodic structure. The images are recorded at free-space wavelengths of (a,d) 730 nm, (b,e) 800 nm, and (c,f) 860 nm. Images (b) and (e) are linked with the movies (629KB and 574KB) showing images of scattering of a SPP beam on the corresponding structures passing across.

Lensing effect. The observed deflection seems sufficient for focusing of SPP beams. Indeed, circular-shaped periodic arrays can be seen as a set of prisms with their angles, particularly near the edges, being considerably larger than 45 degrees. We fabricated two such arrays: one of 7.5 μm and the other of 15 μm diameter. Figures 2(a–c) show scattering of a SPP beam with the first of those two structures recorded at different free-space wavelengths. The images clearly demonstrate the focusing property of the structure (cf. with Fig. 1 in [17]), however neither of the figures shows a SPP focusing to a spot. This has two reasons: (i) the incident beam is not a plane wave, but rather a divergent Gaussian beam, and (ii) there is a sufficient spherical aberration due to the nonparaxial rays participating in the image formation. This set of images demonstrates also a wavelength dispersion of the periodic structure with the highest ERI corresponding to the lowest wavelength. Yet, it is difficult to give a quantitative estimate to the dispersion or to the ERI of the SPP inside this array. This was investigated using 15-

μm-diameter circular-shaped array of bumps. With this structure the focusing effect was not clearly observed because of the lower optical strength of the lens due to the decreased curvature. Instead, a well pronounced deflection of a part of SPP beam impinging the edge of the array (Figs. 2(d–f)) was observed. Beside the increased propagation length of SPPs, one can notice a slight decrease of the scattering angle with the increasing wavelength, which indicates also the decrease of the ERI. We estimated those angles to be 24°, 22° and 19° for the wavelengths 730 nm, 800 nm and 860 nm, respectively.

From the images obtained, we evaluated that the border area responsible for the SPP deflection is approximately 2-μm-wide. Thus, the geometrical shape of the array involved in the deflection process is a 2-μm-high circular segment, which has an angle adjacent to the chord of $\sim 30°$. For the simplicity of our estimation, we substitute that circular segment with an isosceles 120° prism ($180° - 30° - 30°$) and assume a symmetric passage of the beam when the refractive index n of the prism is given by a well-known formula: $n = \sin(\alpha/2 + \theta/2)/\sin(\alpha/2)$, where α is the prism angle, and θ is the deflection angle. This gives the ERI values of $n = 1.10$ at 730 nm, $n = 1.09$ at 800 nm, and $n = 1.08$ at 860 nm. Even though it is a rough estimate, it gives an order of magnitude of the ERI dispersion. It also demonstrates the consistency of the ERI value obtained with the triangular structure.

Sets of scattering images when the structures were moved across the stationary SPP beam were also recorded (movies linked to Figs. 2(b) and 2(e)). The sets of images are obtained at the free-space wavelength of 800 nm.

Waveguiding. A simple estimation for the possibility of waveguiding inside rectangular arrays of nanoparticles can be given by determining the V-parameter (normalized frequency) of the planar waveguide and by comparing this parameter with the dispersion curves [18]. In our case of propagating SPPs, the V-parameter is defined as follows: $V = kd(n_1^2 - n_2^2)^{1/2} \approx kd\sqrt{2n_2\Delta n}$, where k is the propagation constant of SPP at a flat surface, d is the waveguide width, n_1 and n_2 are the effective refractive indices of the waveguide and the outer region, respectively. With n_2 being 1 and Δn being 0.08, one gets $V = 2.98$ for a 1-μm-wide planar waveguide at the free-space wavelength $\lambda_0 = 860$ nm, which is enough to have one guided mode [18] with about 83% of power concentrated inside the waveguide [19]. A 2-μm-wide planar waveguide is already double-mode ($V = 5.95$) with about 96% of power of the first and 80% of power of the second mode concentrated inside the waveguide. We note, though, that with the symmetrical illumination of the waveguide, only the first mode is excited since the overlap integral with the second mode is zero.

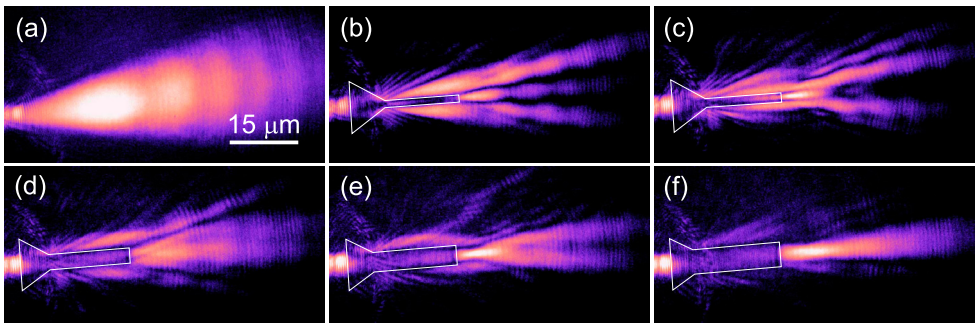

Fig. 3. LRM image of a SPP beam propagating along (a) a smooth gold film and (b–f) a gold film covered with funnel waveguides of the width (b) 1 μm, (c) 2 μm, (d) 3 μm, (e) 4 μm, and (f) 5 μm shown by a white contour line. The funnel region is an equilateral triangle with the side length of 10 μm. The total length of each waveguide (including the funnel region) is 25 μm.

To prove the possibility of SPP waveguiding by periodic patterns of nanoparticles, we fabricated five arrays having a shape of waveguides of width 1, 2, 3, 4 and 5 μm and of length 25 μm. To facilitate the coupling of a smooth gold film SPP to the guided modes, the input of each waveguide was made in a form of a funnel which is an equilateral triangle with the side length of 10 μm. Figure 3(a) shows the reference SPP beam used to test the funnel waveguides, and Figs. 3(b–f) illustrate the propagation of this beam through the structures under consideration (wavelength $\lambda_0 = 860$ nm). As it is expected from the estimation, the narrowest structure supports a mode, which is evidenced by the SPP beam coming out of the waveguide (Fig. 3(b)). In fact, this beam is strongly divergent because the waveguide width is about the wavelength. This divergent SPP beam interferes with the plasmons leaking out of the funnel and then propagating outside, along the waveguide. Three beams discernible at the output of the waveguide are the result of this interference. For wider waveguides the output SPP beam diverges less, and less power leaks out of the funnel. As a result, with the increasing width of the waveguide, the interference pattern converges to a single SPP beam (Figs. 3(c–f)). Figure 3(f) demonstrates almost perfect (without leakage from the funnel region) coupling of the incident SPP to guided modes and a well confined plasmon beam coming out of the waveguide.

4. Numerical simulations

The SPP beam scattering by periodic arrays of particles was numerically simulated using total Green's tensor formalism and the dipole approximation for multiple SPP scattering by nanoparticles [20–22]. The bumps forming the arrays were approximated by spherical particles, considered as point-dipole scatterers suspended 40 nm above the surface, and characterized with isotropic free-space polarizability obtained in the long-wavelength approximation. First, the dipole moments of particles illuminated with a Gaussian SPP beam were calculated self-consistently, and then the total electric field distribution was determined 130 nm above the sample surface (using in both cases the total Green's dyadic) [21]. The radius of the particles was a fitting parameter chosen to match the experimental images.

To optimize the calculation resources, we reduced the total amount of scatterers in the modeled array by increasing their periodicity up to 150 nm. As long as the array period is sufficiently smaller than the incident SPP wavelength, we consider this method as a one giving the correct result, provided that the size of the particles is adjusted appropriately. We found that experimental images are best fitted in simulations if the diameter of the bumps is set to 60 nm. Note that this is the value we had in the experiment, even though the array period was smaller. This is because the size of the particles used in simulations is only relevant within the model and influences particles' polarizability, but does not bear a direct relation to the size of the bumps in the experiment.

Figure 4(a) shows the zoom into the dashed bar in Fig. 2(b). This is the experimental LRM image that we tried to fit in calculations shown in Fig. 4(b). One can see a very good agreement with the main features perfectly reproduced, which confirms the validity of the developed numerical approach.

With the diameter of bumps having been fitted, we were able to model a SPP beam deflection by a periodic triangular structure, similar to that shown in Fig. 1(a), to determine the ERI of the structure. Figure 4(c) shows the result of the modeling. As an incident wave, we used a Gaussian SPP beam having the waist situated 5 μm apart (before) the array. The divergent SPP beam is partially reflected (inside the structure) by the horizontal cathetus of the triangle. This creates an interference pattern in form of several dark lines along the passed through the structure SPP beam (the lowermost one is clearly pronounced). To estimate the magnitude of the beam deflection, we used its upper part: the dashed line in Fig. 4(c) shows the assumed direction of SPP beam propagation after the periodic structure. The deflection angle was estimated to

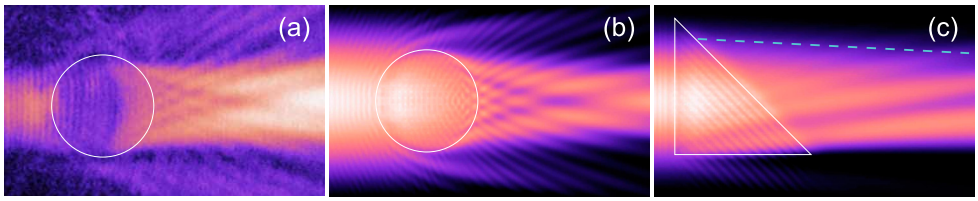

Fig. 4. (a) The zoom into the dashed rectangle shown in Fig. 2(b) and (b) the electric field intensity distribution calculated at the height of 130 nm above the surface plane in the same region. (c) The electric field intensity distribution calculated (130 nm above the surface) for the SPP beam incident onto a periodic array of bumps having the shape of a right-angle triangle. The dashed line shows the propagation direction of the SPP beam after its scattering by the array and indicates the deflection of the SPP beam by such a triangular prism.

be approximately 3 degrees, which gives the ERI of the structure $n_{\text{eff}} \approx 1.05$. This value is very close to the one obtained experimentally and is somewhat smaller, which can be partially explained by our underestimation of the SPP beam deflection magnitude due to its divergent behaviour. Thus, we showed that the developed numerical approach gives consistent results and can be used to model SPP scattering on various structures prior to their fabrication. Moreover, we showed that the value of the ERI estimated in the experiment is fairly reliable.

5. Conclusion

Summarizing, we showed that a periodic pattern of gold nanoparticles with a period considerably smaller than the wavelength of the propagating SPP possesses an effective refractive index of about 1.08. We demonstrated the possibility of creating variously shaped arrays that feature useful properties such as prism effect, lensing, and waveguiding using the total internal reflection. Even though the similar properties had already been observed on dielectric-coated gold surfaces [10], we believe that the periodic patterns are more flexible, since the ERI can be controlled by the filling factor of the structure. In addition, the refractive index can be sufficiently higher at the wavelength close to the resonance of the individual nanoparticle, thus giving rise to non-trivial dispersion properties that can lead to new interesting phenomena.

Acknowledgments

The authors gratefully acknowledge support from the Danish Technical Research Council (Contract No. 26-04-0158), European Network of Excellence, Plasmo-Nano-Devices (FP6-2002-IST-1-507879), Russian Foundation for Basic Research (Grant No. 06-02-16443), and the NABIIT project (Contract No. 2106-05-033 from the Danish Research Agency).

Chapter 4

SP nano-slit couplers

New Journal of Physics
The open-access journal for physics

Modulation of surface plasmon coupling-in by one-dimensional surface corrugation

F López-Tejeira[1], Sergio G Rodrigo[1], L Martín-Moreno[1,9], F J García-Vidal[2], E Devaux[3], J Dintinger[3,7], T W Ebbesen[3], J R Krenn[4], I P Radko[5], S I Bozhevolnyi[5], M U González[6,8], J C Weeber[6] and A Dereux[6]

[1] Departamento de Física de la Materia Condensada, Facultad de Ciencas-ICMA, Universidad de Zaragoza-CSIC, E-50009 Zaragoza, Spain
[2] Departamento de Física Teórica de la Materia Condensada, Universidad Autónoma de Madrid, E-28049 Madrid, Spain
[3] Laboratoire de Nanostructures, ISIS, Université Louis Pasteur, F-67000 Strasbourg, France
[4] Institute of Physics, Karl Franzens University, A-8010 Graz, Austria
[5] Department of Physics and Nanotechnology, Aalborg University, DK-9220 Aalborg, Denmark
[6] Laboratoire de Physique de l'Université de Bourgogne, UMR CNRS 5027, F-21078 Dijon, France
E-mail: lmm@unizar.es

New Journal of Physics **10** (2008) 033035 (19pp)
Received 21 December 2007
Published 27 March 2008
Online at http://www.njp.org/
doi:10.1088/1367-2630/10/3/033035

Abstract. Surface plasmon-polaritons have recently attracted renewed interest in the scientific community for their potential in sub-wavelength optics, light generation and non-destructive sensing. Given that they cannot be directly excited by freely propagating light due to their intrinsic binding to the metal surface, the light–plasmon coupling efficiency becomes of crucial importance for the success of any plasmonic device. Here, we present a comprehensive study on

[7] Present address: Nanophotonics and Metrology Laboratory, Swiss Federal Institute of Technology Lausanne (EPFL), CH-1015 Lausanne, Switzerland.
[8] Present address: ICFO-Institut de Cincies Fotniques, E-08860 Castelldefels, Spain.
[9] Author to whom any correspondence should be addressed.

the modulation (enhancement or suppression) of such a coupling efficiency by means of one-dimensional surface corrugation. Our approach is based on simple wave interference and enables us to make quantitative predictions which have been experimentally confirmed at both the near-infrared and telecom ranges.

Contents

1. Introduction

Surface plasmon-polaritons (SPPs) are electromagnetic (EM) modes originating from the interaction between light and mobile surface charges, typically the conduction electrons in metals [1]. Because of the so-called 'excess of momentum' with respect to light of the same frequency, SPPs cannot propagate away from a planar surface and are thus bound to and guided by it. As a consequence of this binding, SPP modes can be laterally confined below the diffraction limit, which has raised the prospect of SPP-based photonic circuits [2–4]. To build up this kind of circuit, one would require a variety of components in which incident light would be first converted in SPPs, propagating and interacting with different devices before being recovered as freely propagating light. Hence, a great deal of attention has recently been devoted to the creation of optical elements for SPPs [5]–[10], as well as to the efficient coupling of freely-propagating light into and out of them. This latter issue constitutes the fundamental bottleneck that must be overcome in order to fully exploit the potential of SPPs, given that established techniques for SPP generation (which make use of prism [11, 12], grating [13] or nanodefect [14] coupling) require that the system's size be well out of the sub-wavelength scale in order to obtain a neat SPP signal. On the other hand, p-polarized back-side illumination of sub-wavelength apertures in optically thick metal films [15]–[22] prevents both damping and signal blinding but it does not ensure a unique propagation direction for the generated SPPs.

In a previous work [23], we proposed a novel back-side slit-illumination method based on drilling a periodic array of indentations at one side of the slit. It was demonstrated that the SPP beam emerging from the slit to its corrugated side can be backscattered in such a way that it interferes constructively with the one propagating in the opposite direction, thus obtaining a localized unidirectional SPP source. Here, we provide a comprehensive version of our proposal and discuss to some extent its range of validity. Additional experimental measurements will also be presented.

IOP Institute of Physics DEUTSCHE PHYSIKALISCHE GESELLSCHAFT

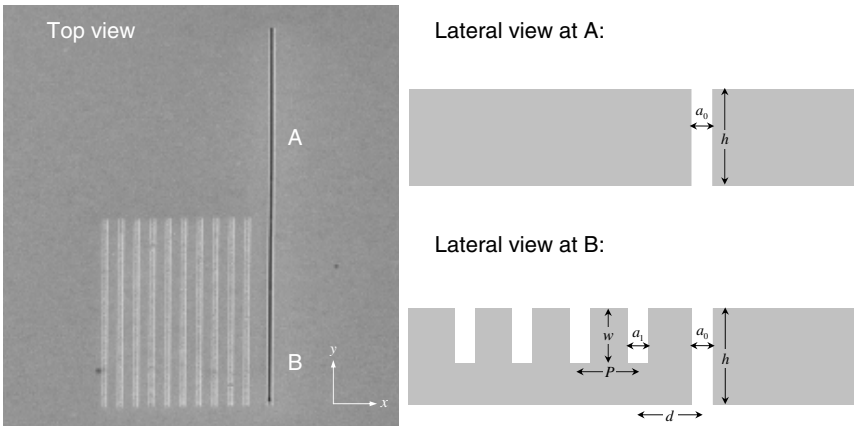

Figure 1. Scanning electron micrograph and schematic diagrams of the proposed structure. Parameters $\{a_i, h, w, d, P\}$ defining the geometry of the system are also shown.

This paper is organized as follows: in section 2, we summarize the key concepts of our proposal and focus on some quantitative aspects of SPP generation and reflection. The validity of our simple wave interference model is discussed in section 3. Finally, experimental results are presented in section 4, prior to the general conclusions.

2. Description of our proposal

A picture of the proposed structure is shown in figure 1. A periodic array of one-dimensional (1D) indentations is fabricated at the output metal surface close and parallel to the illuminated slit. The starting point for such a design can be found in a previous work on 1D SPP scattering by means of a modal expansion formalism [24, 25]. In order to cope with SPP launching, we considered a single slit flanked by an array of indentations (rectangular grooves) placed in the output surface of a thick metallic film. Eventually, the distance between the slit and indentations was taken to be infinity. In this way, the slit merely played the role of a theorist's SPP-launcher, as far as it can be shown that the field created by the slit corresponds to SPP illumination into the grooves. Besides, we also found a simple geometrical condition for the groove array to behave as a perfect Bragg mirror, associated with the low-λ edge of the plasmonic bandgap for the periodic system. Combining these two elements, one can obtain a remarkably simple scheme to modulate the SPP coupling-in at a real back-side illumination experiment: given an incident wavelength, let us design a groove array for which SPP reflectance rises to a maximum and place it at a distance d from the slit (situation B of figure 1). Hence, any outgoing SPP generated at the same side of the slit will be mainly backscattered by the grooves and interfere either constructively or destructively with the one that is generated at the opposite side. This interference can be tuned by adjusting the separation d between the slit and the first groove of the array, defined centre to centre. The total phase difference, ϕ, between the interfering SPPs will then consist of the phase change upon reflection plus the additional shift resulting from the

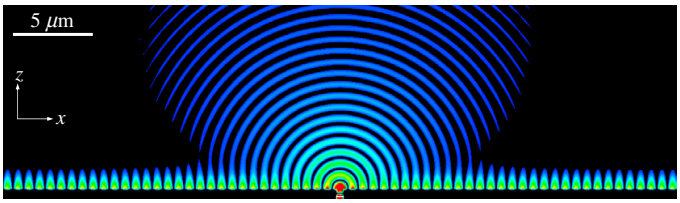

Figure 2. Calculated $|\mathrm{Re}[H_y]|$ distribution at the output surface of an Au film perforated by a single slit (situation A of figure 1). Incident light is p-polarized and impinges normally onto the back side of the metal surface at $\lambda = 800$ nm. Here, slit width $a_0 = 160$ nm and film thickness $h = 300$ nm.

two different path lengths along the metal:

$$\phi = \phi_R + 2\mathrm{Re}[k_p]\, d, \tag{1}$$

where k_p holds for in-plane plasmon wavevectors. According to (1), constructive or destructive interference should occur for those phase values equal to, respectively, even or odd multiples of π.

It is clear that, as will be discussed in section 3, several objections may arise against this very simplified model, but before we turn to its validity, let us take a closer look at the two ingredients on which it is based: the generation of SPPs at a sub-wavelength aperture and the phase they acquire as a result of Bragg reflection.

2.1. SPP generation at a single sub-wavelength slit

Figure 2 presents a finite-difference time-domain (FDTD) [26] simulation of the (EM) field distribution originated from p-polarized back-side illumination of a sub-wavelength slit on a thick Au film. As can be seen, the most of the field is diffracted away, but a significant fraction appears to be bound to the metallic surface at each side of the aperture. However, to what extent is that a confined state of surface plasmon?

Such an assessment requires that analytical expressions for the EM field distribution created by the slit be obtained without any *a priori* assumption about the presence of SPPs. For that purpose, we have made use of the above-mentioned modal expansion technique. Given that it has been extensively described elsewhere [24, 25], let us just briefly summarize its basic ingredients: the EM fields are expanded in terms of the eigenmodes in each spatial region (plane waves at input/output regions and waveguide modes inside the indentation) and then the expansion coefficients are obtained by just matching appropriately the parallel components of the fields at the two metal–dielectric interfaces. The dielectric response of the metal is taken into account by applying surface impedance boundary conditions (SIBC) [27] to the tangential components of the EM fields at the metallic surface. For a non-magnetic medium,

$$\boldsymbol{F}_t(\boldsymbol{r}) \equiv \boldsymbol{E}_t(\boldsymbol{r}) - Z_s \boldsymbol{H}_t(\boldsymbol{r}) \times \boldsymbol{n}(\boldsymbol{r}) = 0, \tag{2}$$

where $Z_s = \varepsilon(\lambda)^{-1/2}$ and $\boldsymbol{n}(\boldsymbol{r})$ is the unitary vector normal to the surface directed into the metal half-space. However, SIBC are not applied at the vertical walls defining the slit but for the calculation of propagating constants along the z-direction. This choice allows us to express the EM fields inside in terms of the waveguide eigenmodes of a perfect conductor (PC), which are

known analytically. Although the absorption inside the cavities is therefore neglected, one can expect this not to be a serious shortcoming when considering sizes much greater than the skin depth. The end product of our expanding and matching is a linear system of algebraic equations that connect the modal amplitudes of the $\boldsymbol{F}$ field at the input and output openings of the slit. Once those self-consistent amplitudes are found, it is straightforward to obtain the EM fields at any desired point.

By imposing the constraint that incident light impinges in 'classical mounting' (i.e. within the xz-plane), we just have to concern ourselves with the y-component of the magnetic field. From a mathematical point of view, H_y at the output side is obtained by integrating all across the slit every considered eigenmode ϕ_n multiplied by a scalar 1D Green's function and then weighting each contribution with the corresponding amplitude E'_n at the output opening:

$$H_y(x,z) = -\sum_n E'_n \int_{x_0-a_0/2}^{x_0+a_0/2} \mathrm{d}x' G(x,x';z)\phi_n(x'), \tag{3}$$

where z stands for the distance from the output surface. This closely resembles the Huygens–Fresnel description of wave propagation in terms of a set of point emitters, but we have to keep in mind that all those 'emitters' are self-consistently connected.

However, information on the character of the generated field is contained neither in the modes nor in their amplitudes, but in the propagator itself:

$$G(x,x';z) = \frac{\mathrm{i}}{\lambda}\int_{-\infty}^{+\infty} \mathrm{d}k \frac{\exp[\mathrm{i}(k(x-x')+\sqrt{k_0^2-k^2}z)]}{\sqrt{k_0^2-k^2}+k_0 Z_\mathrm{s}}, \tag{4}$$

where $k_0 \equiv 2\pi/\lambda$. Despite its impressive appearance, $G(x,x';z)$ just computes the projection of EM fields at the opening of the slit onto all possible diffracted waves, whether they are propagating or evanescent. Bound-to-interface contributions are incorporated into the picture as a consequence of finite Z_s, which makes the difference with respect to PC approximation: for $Z_\mathrm{s} = 0$, (4) transforms into an integral representation of the zeroth-order Hankel function of the first kind (i.e. the well-known Green's function for the two-dimensional Helmholtz operator [28]), otherwise it has to be evaluated numerically. Such a numerical inspection reveals that $G(x,x';z)$ tends to the PC result for $|x-x'| \ll \lambda$ irrespective of Z_s [24, 25]. On the other hand, in the regime where $z, |x-x'| \approx O(\lambda)$, oscillatory contributions within the kernel of (4) mutually cancel everywhere but in the region close to the integrand singularities at $k = \pm k_\mathrm{p}$, with k_p satisfying

$$\sqrt{k_0^2-{k_\mathrm{p}}^2} = -Z_\mathrm{s}k_0. \tag{5}$$

This is, by the way, the SPP dispersion relation of a flat metal–dielectric interface within the SIBC. In that asymptotic limit, Green's function can be explicitly approximated as

$$G_\mathrm{as}(x,x';z) = -\frac{k_0^2 Z_\mathrm{s}}{k_p}\,\mathrm{e}^{\mathrm{i}(k_\mathrm{p}|x-x'|-k_0 Z_s z)}. \tag{6}$$

Therefore, and even in the presence of absorption, SPPs govern the EM coupling along the surface at a distance of several wavelengths, whereas 'PC-like' behaviour is observed at the close vicinity of the slit. It is worth mentioning that this simple fact is completely misinterpreted in several recent papers, as pointed out in a previous work [29]. In any case, the existence of these two regimes has also been remarked by introducing a 'creeping wave contribution' that

IOP Institute of Physics DEUTSCHE PHYSIKALISCHE GESELLSCHAFT

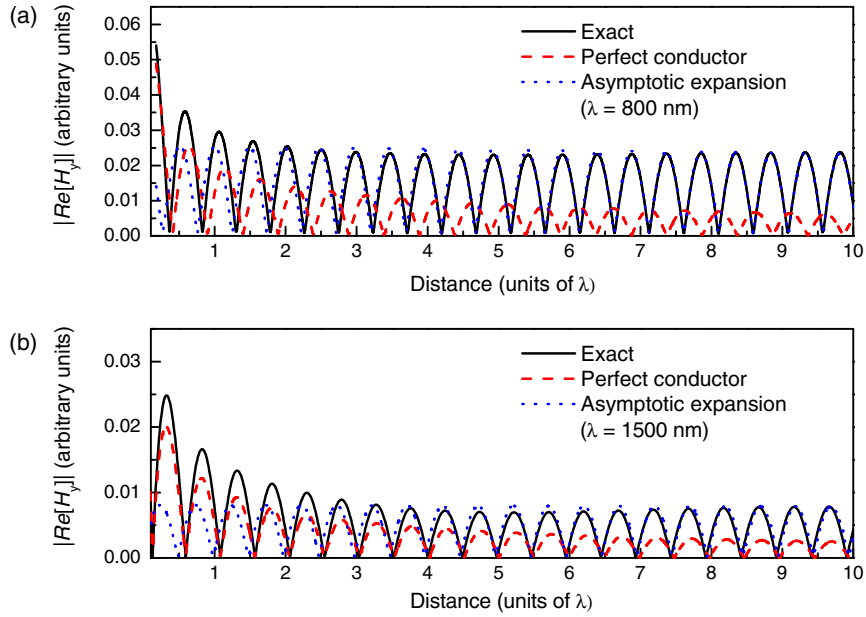

Figure 3. Calculated $|\mathrm{Re}[H_y]|$ as a function of the distance from the centre of the slit, evaluated at the output surface of an Au film. Solid lines represent the full calculation, whereas dashed and dotted ones stand for PC approximation and asymptotic expansion, respectively. The geometrical parameters are: slit width $a_0 = 160$ nm and film thickness $h = 300$ nm. Incident light is p-polarized and impinges normally onto the back side of the metal surface. (a) and (b) Results for $\lambda = 800$ and $\lambda = 1500$ nm, respectively.

rapidly vanishes for increasing distances and is explicitly defined as the difference between total and SPP fields along the metal–dielectric interface [30].

In order to determine the precise range of distances for the EM field at figure 2 to be dominated by either 'PC-like' or SPP contribution, we have calculated $|\mathrm{Re}[H_y]|$ at the metal surface for Z_s values corresponding to that of Au at 800 and 1500 nm. Each calculation was carried out for the exact, asymptotic and PC versions of Green's function. As can be seen in figure 3, comparison with the exact result in the near-infrared (NIR) shows that the asymptotic limit is already reached for a distance of about 2λ from the centre of the slit, which is increased up to 6λ when the incident wavelength falls within the telecom range. Consequently, it is only for greater distances that we can unambiguously establish a one-to-one correspondence between fields at the interface and SPPs.

In figure 4, we present the fraction of the output current that is transferred into SPPs (f_{SPP}) and scattered out of the plane (f_{out}) for the same Z_s parameters as in figure 3 all across the sub-wavelength regime. Given that SPPs gradually attenuate when propagating along the metal, the values for f_{SPP} are calculated at $x = \pm a_0/2$ in order to compare with those of f_{out}. As the slit width increases, the out-of-plane radiation is clearly favoured at the expense of the coupling

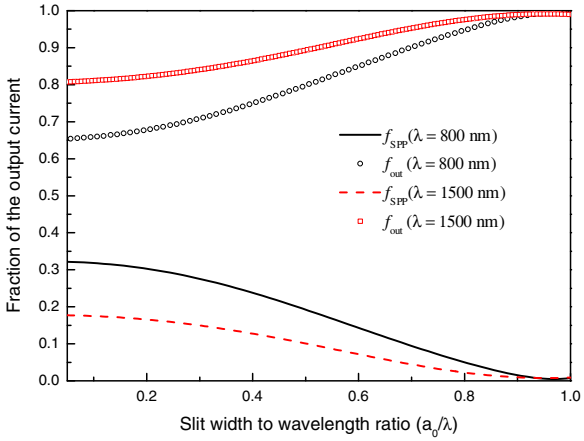

Figure 4. Fraction of the energy that is transferred into SPPs (lines) and scattered out of the plane (symbols) at the output surface of an Au film perforated by a single slit that is back-side illuminated with p-polarized light. The values for f_{SPP} are calculated at distances of $\pm a_0/2$ from the centre of the slit.

into SPPs, which can be easily found to be proportional to $(\sin[k_{\mathrm{p}}\, a_0/2]/k_{\mathrm{p}}\, a_0)^2$ because of the geometry of the system [24, 25]. For typical experimental width $a_0 = 160\,\mathrm{nm}$, no more than 30% of the output energy is driven into SPPs at $\lambda = 800\,\mathrm{nm}$ and such a percentage is reduced to 17% at $\lambda = 1500\,\mathrm{nm}$. These values are in good agreement with those previously reported [21] and provide a preliminary estimate of the expected performance for our proposed slit + grating structure when operating at perfect constructive interference conditions.

2.2. Phase shift upon Bragg reflection

As mentioned at the beginning of the section, it has been shown that the reflection of SPPs by a periodic array of indentations presents maxima at those frequencies corresponding to the low-λ edges of plasmonic bandgaps [24, 25]. For narrow sub-wavelength indentations, the spectral locations of these edges can be approximated by folding the dispersion relation of SPPs for a flat metal surface into the first Brillouin zone [31]. Within the SIBC, such a folding results in

$$k_{\mathrm{p}} P = k_0 \mathrm{Re}[q_{\mathrm{p}}] P = m\pi, \quad m = 1, 2, \ldots, \tag{7}$$

where P is the period of array and $q_{\mathrm{p}} \equiv \sqrt{1 - Z_{\mathrm{s}}^2}$. Remarkably, although the reflectance maxima depend on the groove geometry (width and depth) and the number of grooves [24, 25], their spectral locations do not (see figure 5).

Assuming that λ and P fulfil (7), let us consider the phase shift for a given resonant wavelength λ_{R}. Information on such a shift is contained in the complex reflection coefficient r relating the amplitudes of incident and reflected fields. Although the obtention of r is usually regarded as a mere preliminary to that of reflectance (defined as $R = |r|^2$), we can always establish a straightforward connection between r and phase shift ϕ_{R}:

$$\cos\phi_{\mathrm{R}} = \mathrm{Re}[r]/|r|; \quad \sin\phi_{\mathrm{R}} = \mathrm{Im}[r]/|r|. \tag{8}$$

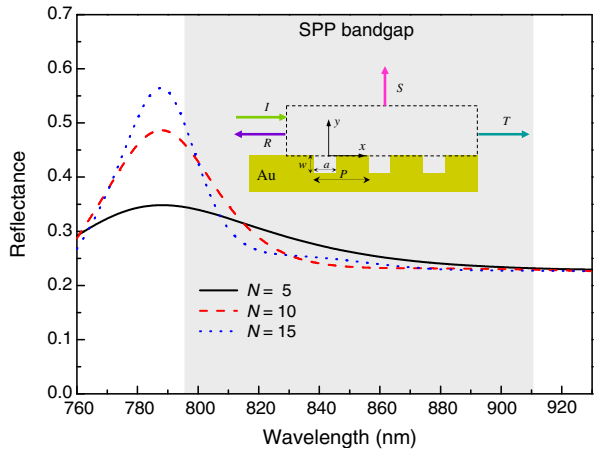

Figure 5. Calculated reflectance of SPPs by a finite periodic array consisting of 5 (solid line), 10 (dashed) and 15 (dotted) grooves carved on Au. Here, $a = w = 100$ nm and $P = 390$ nm. Grey-shaded area marks the region where a plasmonic bandgap occurs. SPP fields are evaluated at $x = -3.5\,\mu$m ($\approx -3.8\lambda_{\max}$), the origin being located at the centre of the first groove.

Once the asymptotic limit is already reached, these auxiliary magnitudes $\cos\phi_R$, $\sin\phi_R$ provide complete information about SPP shift upon reflection, irrespective of the exact distance at which fields are evaluated. We have found that ϕ_R is close to π over a wide range of groove depths for $a/\lambda \leqslant 0.2$ at both NIR and telecom ranges, as can be seen in figure 6. Taking this result into account and substituting for k_p from (7) into (1) yields

$$\phi(\lambda_R) = (2md/P + 1)\pi, \tag{9}$$

which reduces the design of our proposed scheme to a suitable choice of the d/P ratio.

3. Validity of the simple wave interference model

Our previous discussion leading to (9) implies that slit and grating be considered as independent elements. Therefore, it does not take into account the radiation coming back from the grooves, while, in principle, EM fields at all openings have to be self-consistently calculated [32]. In order to quantify the 'perturbation' of the SPP source (i.e. the slit), we define a re-illumination parameter ξ that averages the modification of the x-component of the electric field inside the slit originated by the adjacent grating:

$$\xi = \frac{1}{a_0}\int_{-a_0/2}^{+a_0/2} \mathrm{d}x' |1 - E_x(x')/E_x^{ss}(x')|, \tag{10}$$

where a_0 is the width of the slit, E_x the x-component of the electric field calculated in the presence of the array and E_x^{ss} the one obtained for the isolated slit.

In figure 7, we present a contour plot of ξ versus groove depth and slit-to-array separation for a system with ten grooves at $\lambda = 800$ nm. As can be seen, the modification of the field

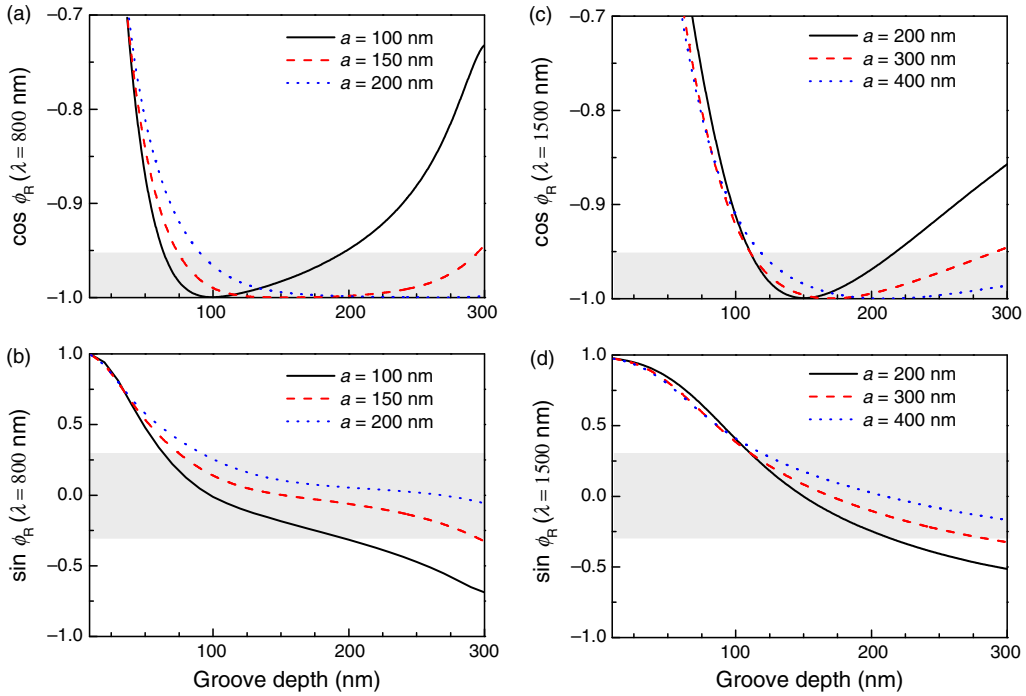

Figure 6. Calculated values of $\cos\phi_R(\lambda_R)$, $\sin\phi_R(\lambda_R)$ of a ten-groove array in Au for increasing values of groove depth. (a) and (b) Results for $a = 100$, 150 and 200 nm (solid, dashed and dotted lines, respectively) evaluated at $\lambda_R = 800$ nm ($P = 390$ nm, $m = 1$). Results for $a = 200$, 300 and 400 nm at $\lambda_R = 1500$ nm ($P = 750$ nm, $m = 1$) are presented in (c) and (d). Grey-shaded areas mark the region where $\phi_R = \pi \pm 0.1\pi$. Results for $\lambda_R = 800$ and 1500 nm are calculated at distances of 3λ and 7λ from the centre of the first groove, respectively.

pattern within [400, 800] nm is below 15% and ξ rapidly decreases for increasing distances, thus supporting our implicit assumption in (9). With respect to the dependence on groove depth, it is governed by the reflectance properties of the array, ξ rising to its maximum as R does (see the inset in figure 7). Such a maximum becomes clearer the more separation approaches to the plasmonic regime ($d \approx 3\lambda$). On the other hand, modulation along the vertical axis results from simple interference between counter-propagating SPP waves originated at the slit and its nearest groove. Therefore, sequential minima of ξ appear for $d = (2m+1)\lambda_p/4$, whereas $\{\xi_{max}\}$ are associated with $d = m\lambda_p/2$, given that $\lambda_p = 2\pi/k_p$ and $m = 0, 1, 2, \ldots$.

However, the key point of our proposal still relies on SPPs being reflected by a groove array, while the EM fields radiated by the slit cannot be considered 'purely plasmonic' but at a distance of several wavelengths (see figure 3). In order to characterize the efficiency of the slit + array system as an SPP-launcher for any slit-to-array separation, we introduce its 'efficiency ratio', E_R: given that the array be located at the left side of the slit (see figure 3), E_R is defined as the quotient between the current intensity of right-propagating SPP with and without

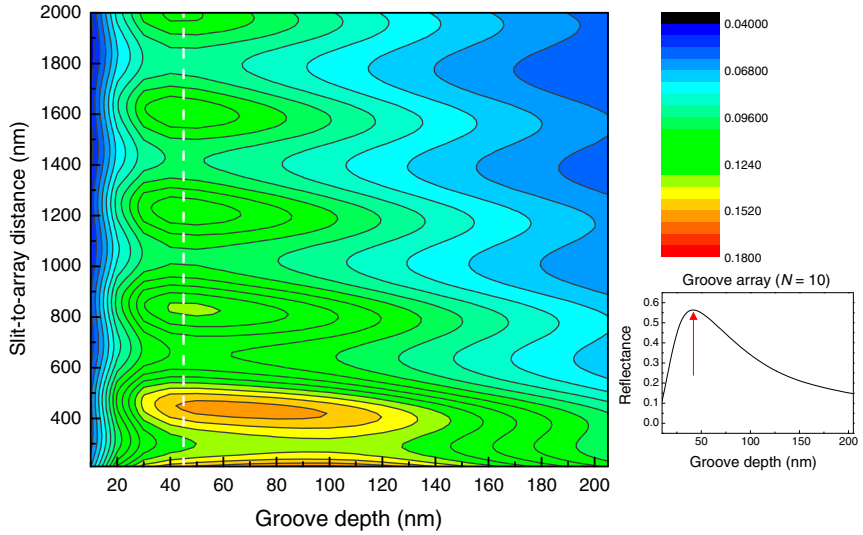

Figure 7. Contour plot of re-illumination parameter ξ in Au as a function of groove depth and slit-to-array separation. Here $a_0 = a_1 = 160\,\text{nm}$, $P = 390\,\text{nm}$, $N = 10$ and $\lambda = 800\,\text{nm}$. The vertical dashed line marks the maximum value of the reflectance curve for the isolated groove array, which is presented at the lower right inset panel.

the grooves. Strictly speaking, E_R provides the efficiency of the output side of the device. The total efficiency, defined as the percentage of incident energy transferred onto the plasmon channel, strongly depends on the illuminating set-up. E_R should vary within the interval $[0, 4]$ showing a dependence on the distance between the illuminating slit and the groove array. More importantly, $E_R > 2$ implies that the right-propagating SPP current in the presence of grooves is larger than the total SPP current (left+right-moving) in the single slit case, so some of the power radiated out of the plane is redirected onto the SPP channel. According to our simple wave interference model,

$$E_R \approx |1 + r\, e^{2ik_p d}|^2, \tag{11}$$

where r is the complex reflection coefficient of the groove array for SPPs.

To check the validity of (9) and (11) for slit-to-array separations outside the asymptotic regime, we have carried out numerical calculations of EM fields by means of both modal expansion and FDTD. The system under consideration is intended to operate at a wavelength of 800 nm on a gold film [33]. We consider an array of ten grooves with a period $P = 390\,\text{nm}$. The depth of the grooves is chosen to be $w = 100\,\text{nm}$, while the width of both grooves and slit is $a = 160\,\text{nm}$, which are typical experimental parameters. Figure 8(a) shows the comparison between (11) and numerical evaluations of E_R, as well as the location of interference maxima (vertical lines) predicted by (9) for $m = 1$. The agreement between the modal expansion and FDTD results is excellent but for distances at which intra-wall coupling between the slit and the first groove has to be taken into account ($d \approx 2a$). As can be seen, the locations of maximum E_R are accurately predicted by (9), which allows us to design SPP-launchers without

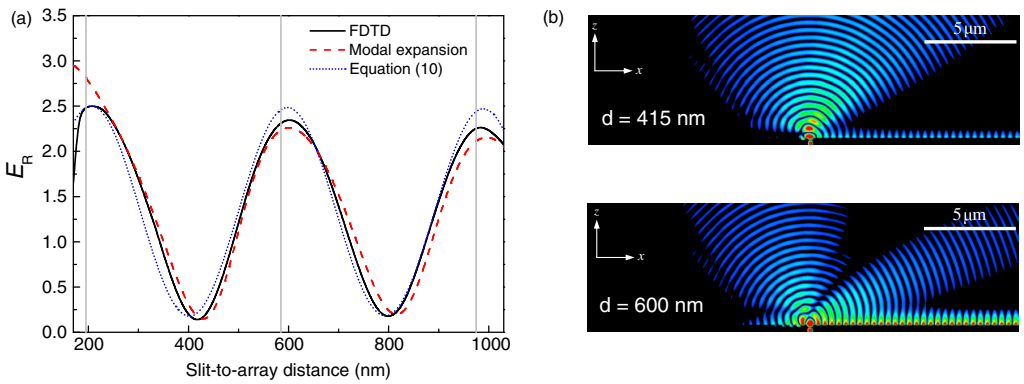

Figure 8. Numerical results for the SPP-launcher at wavelength $\lambda = 800$ nm. (a) Dependence of the efficiency ratio E_R on the slit-to-array distance. The geometrical parameters defining the system are: slit and groove widths $a = 160$ nm, groove depth $w = 100$ nm and array period $P = 390$ nm. The figure renders the curves obtained by means of FDTD (solid), modal expansion (dashed) and equation (11) (short-dotted). Vertical lines mark the positions of E_R maxima according to (9). (b) Calculated $|\mathrm{Re}[H_y]|$ distributions over the xz-plane for two different distances corresponding to minimum and maximum values of E_R at $\lambda = 800$ nm.

elaborate numerical calculations. Moreover, the simplified model of (11) provides a good approximation to E_R with the sole input of r. This also implies that non-plasmonic contributions to groove illumination play a minor role in the occurrence of either constructive or destructive interference, which is clearly described by (11) with the exception of minor shifts.

In addition to the efficiency ratio, field patterns in both minimum and maximum conditions were also calculated using the FDTD method. As shown in figure 8(b), SPPs are completely absent from the left side of the slit, whereas field intensity at the right side of the slit is clearly modulated by the slit-to-array separation, which also governs the spatial distribution of the field that is radiated into vacuum.

4. Experimental results

4.1. NIR measurements

For our proposal to be tested out at the NIR regime, several slit + array samples were fabricated on gold films with a focused ion beam (FIB). As described in [23], each sample consists of a single long ($L = 30\,\mu$m) slit of width $a_0 = 160$ nm perforated at a 300-nm-thick film that is flanked by a periodic array of grooves ($P = 390$ nm, $a = 160$ nm, $w = 100$ nm). Such an array is placed at a given distance d and only extends over $L/2$ (see figure 1). This kind of sample enables us to measure E_R, as the upper part can be used as an on-chip reference of the 'isolated slit'.

A set of samples with $d = \{195, 292, 390, 486, 585\}$ nm was imaged at 800 nm by a photon scanning tunnelling microscope (PSTM) making use of an incident focused beam illumination.

IOP Institute of Physics DEUTSCHE PHYSIKALISCHE GESELLSCHAFT

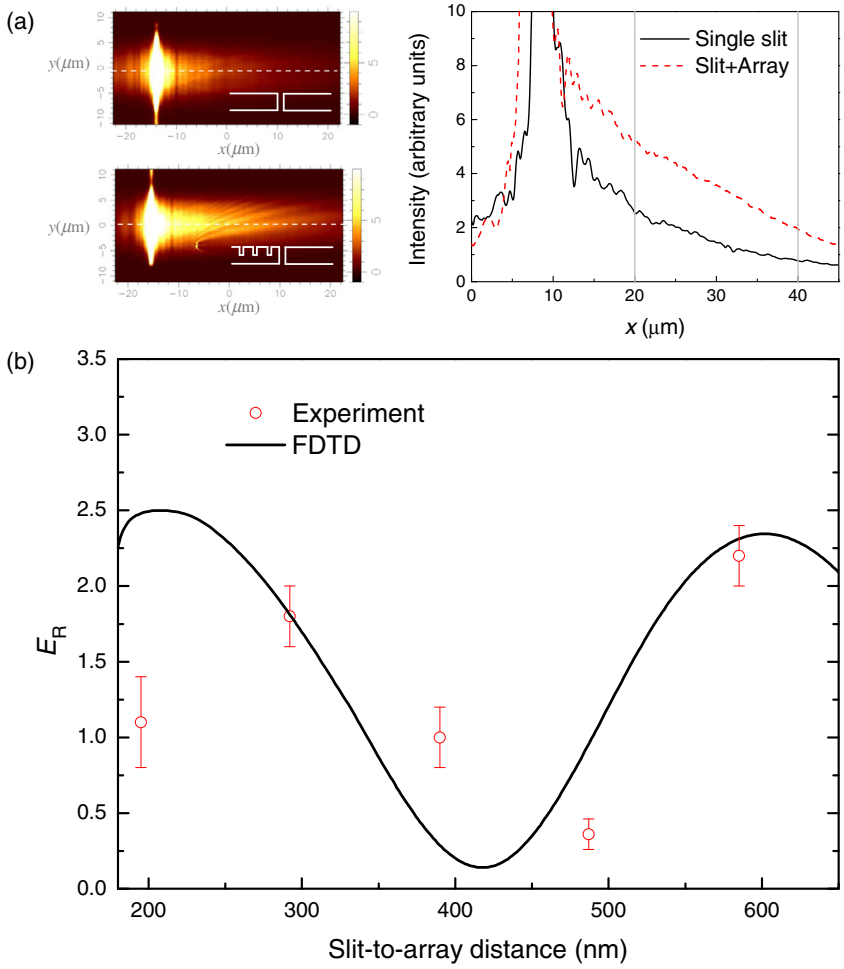

Figure 9. Experimental measurement of E_R at $\lambda = 800$ nm for the same geometrical parameters as in figure 8. (a) PSTM micrographs recorded for a sample with $d = 585$ nm at both 'single slit' (top) and slit + array configurations (bottom). The right panel shows the two cross-cuts from which E_R is obtained. Vertical lines define the interval along which the ratio is averaged. (b) Experimental (circles) and numerical (solid line) values of E_R as a function of slit-to-array distance. The error bars represent the standard deviation over a set of different structures with the same nominal parameters.

For each sample, a pair of images was recorded by scanning at a constant distance of about 60–80 nm from the surface (see figure 9(a)). The first image of the pair, corresponding to an SPP generated from a single slit, is obtained by focusing the laser beam on the upper part of the slit. For the second image, the laser beam is moved to the lower part in order to collect the data for the slit + array structure. An average longitudinal cross-cut of each image is obtained by

using 20 longitudinal cross-cuts, corresponding to different coordinates along the slit axis. Then, the relative position of the two average cross-cuts is adjusted so that the saturated areas (i.e. the signal taken right on top of the slit) are superimposed. Finally, the experimental efficiency ratio, E_R, is extracted by averaging the ratio between the two curves along the longitudinal cross-cut. Figure 9(b) renders experimental values (circles) of E_R for the five different samples fabricated, as well as the ones obtained from FDTD simulations (solid line). The concordance between measurements and theoretical predictions is quite remarkable, especially when taking into account that each experimental point corresponds to an average over a different set of samples. We find that this agreement (previously reported in [23]) provides a clear support to our proposal for a localized unidirectional SPP source.

Another way of looking at the role of surface corrugation is to consider its influence on the fraction of the output energy that is radiated into vacuum. Given that some of the radiated power is redirected onto the SPP channel for the condition of maximum E_R (see field pattern at figure 8), we may wonder whether or not the radiated field is also modulated by the slit-to-array separation. For that purpose, a new magnitude E_{out} can be defined as the ratio between the radiated energy with and without the grooves. According to our numerical simulations, such an 'out-of-plane efficiency' presents a similar (but opposite) dependence on d to that of E_R. In order to obtain experimental values for E_{out}, a new type of sample was designed (see figure 10(a)). Now, the illuminating slit is flanked by two-groove arrays with the same periodicity $P = 390$ nm, each one extending over $L/3$. No corrugation is present at the middle part of the system, for it to be used as the 'single slit' reference. The array on the top is located at a distance $d_1 = 607$ nm for which the coupling to SPPs rises to a maximum at $\lambda = 800$ nm, whereas a minimum appears for the distance $d_2 = 404$ nm of the bottom one. Consequently, the far-field radiation pattern of the composed structure is expected to present a $d_1 \rightarrow d_2$ ascending staircase profile.

In figures 10(b) and (c), we present PSTM images recorded at 800 and 3000 nm from the surface of the sample. As can be seen, the intensity distribution along the illuminating slit increases from the upper to the middle third, as well as from the middle to the lower. Although this behavior is in qualitative agreement with our predictions, a rigorous determination of E_{out} would have required extensive measurements similar to those of E_R. Unfortunately, such a procedure became impossible because of accidental fatal damage in the sample. However, we have managed to obtain a rough estimate of E_{out} from available PSTM images: dashed rectangles in figures 10(b) and (c) mark the areas over a four-line average ($\approx$625 nm) longitudinal cross-cut of each image obtained by means of WSxM software [34]. The resulting intensity profiles at figure 10(d) and (e), show a clear succession of steps, which we decide to characterize by the arithmetic mean along the 5-micron central segment of each plateau. Numerical estimates of E_{out} are then calculated as the ratio between d_1, d_2 and single slit values (see table at the bottom left of figure 10). The coincidence of those estimates with the calculated E_{out} curve in figure 10(f) is amazingly good, which encourages us to carry out conclusive measurements in the near future. With respect to figure 10(f), we finally have to remark that the radiative-to-SPP conversion seems to be more efficient than its opposite, as far as $E_{out} < 2$ for any d.

4.2. Telecom measurements

Similar samples to those used in the NIR measurements were designed to operate at the telecom range by upscaling the period of the array and its separation from the slit (see figure 11(a)).

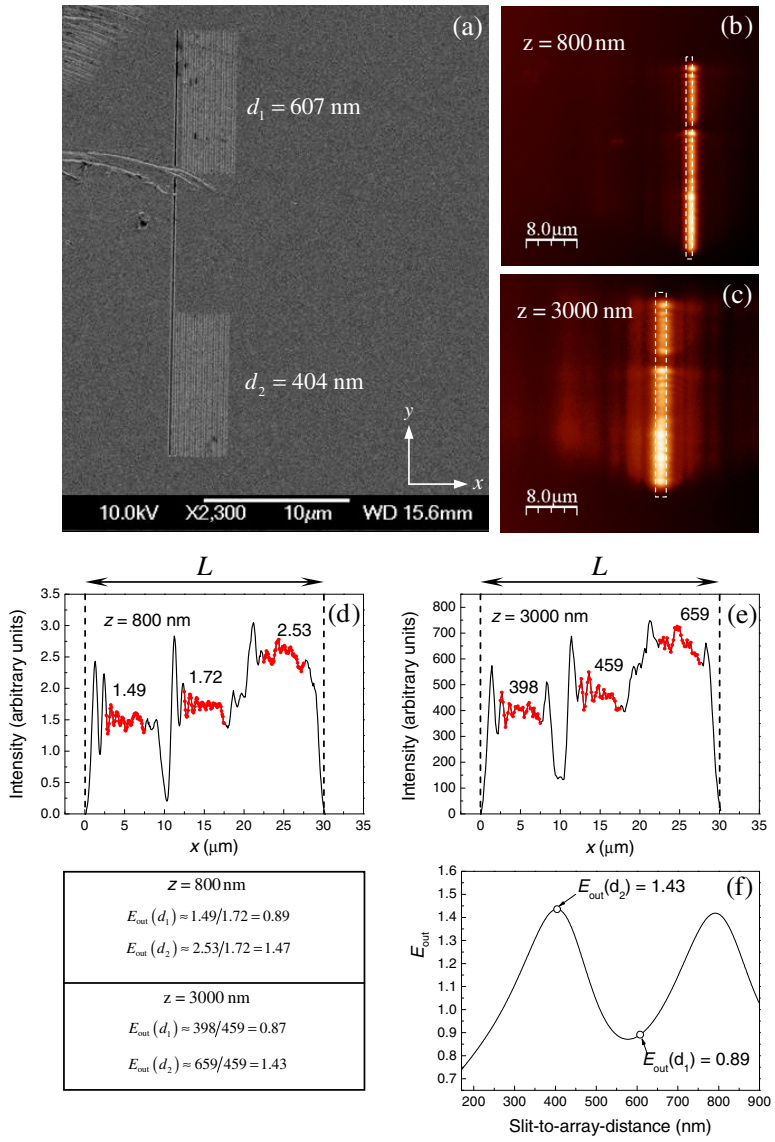

Figure 10. Experimental estimate of E_{out} at $\lambda = 800$ nm. (a) Scanning electron micrograph of the sample. The geometrical parameters are: slit length $L = 30\,\mu$m, slit width $a_0 = 104$ nm, groove width $a = 75$ nm, groove depth $w = 100$ nm and array period $P = 390$ nm. (b) and (c) PSTM micrograph recorded at distances of 800 and 3000 nm from the metal surface. (d) and (e) Average longitudinal cross-cuts along dashed rectangles in images (b) and (c). Vertical dashed lines mark the position of the slit. (f) Calculated E_{out} as a function of slit-to-array distance. Lower left table: summary of the experimental estimates of E_{out}.

IOP Institute of Physics DEUTSCHE PHYSIKALISCHE GESELLSCHAFT

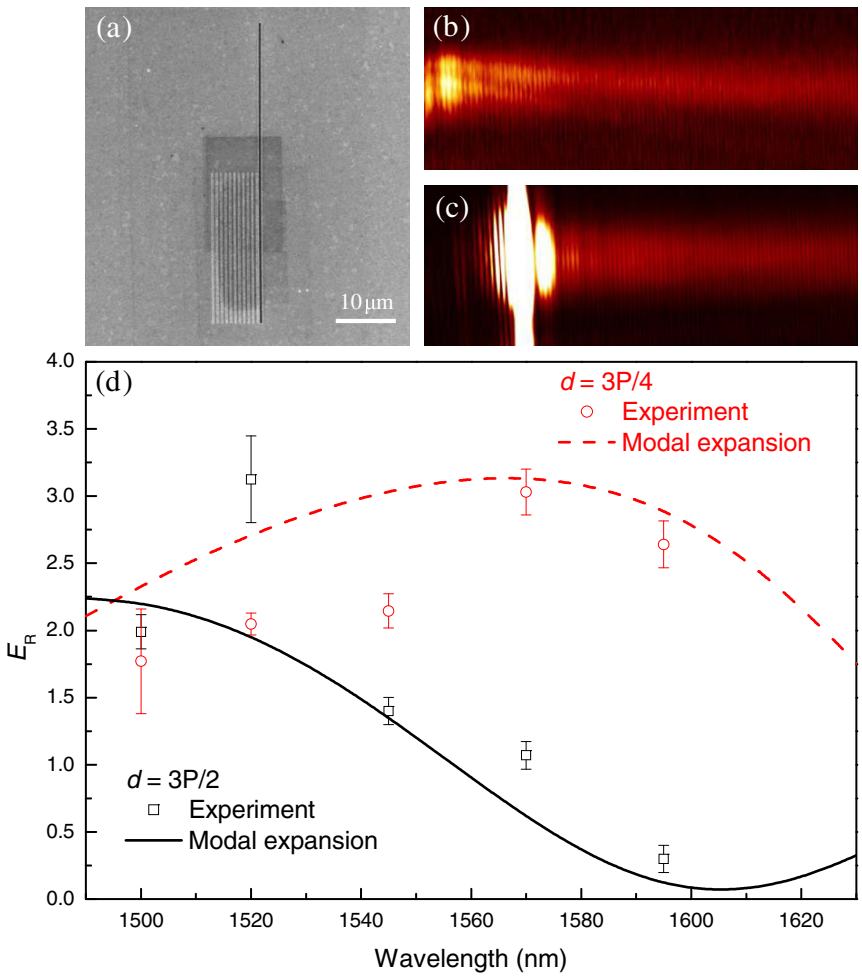

Figure 11. Spectral dependence of E_R at the telecom range. (a) Scanning electron micrograph of the sample. The geometrical parameters are: slit length $L = 50\,\mu$m, slit width $a_0 = 400$ nm, groove width $a = 200$ nm, groove depth $w = 100$ nm and array period $P = 750$ nm. (b) Near-field image recorded with the laser beam focused at the 'isolated slit' position of a sample with $d = 3P/2 = 562$ nm. (Size $= 70 \times 26\,\mu$m^2, $\lambda = 1520$ nm.) (c) Same for slit + array focusing. (d) Spectral dependence of E_R for slit-to-array distances of $d = 3P/2 = 1125$ nm (experiment: squares; theory: solid line) and $d = 3P/4 = 562$ nm (experiment: circles; theory: dashed line).

However, in this wavelength regime, we found a kind of instability in the illumination setup that resulted in a noticeable variation of SPP intensity during the near-field scan process, which takes about 45 min per image. As a consequence of those intensity jumps, the technique used to evaluate the 'efficiency ratio' in the NIR became unsuitable. Instead, we found E_R as the SPP

signal ratio taken from each pair of near-field images (with and without side grooves) at the same distance from the slit, where its non-plasmonic field contribution can be disregarded, whereas the SPP signal is still substantial for the quantification ($\approx$50 μm). To decrease the uncertainty of the thus obtained efficiency, a series of scans were performed for every structure and wavelength measurements, conducting independent adjustments, with the subsequent averaging of the E_R values obtained. Hence, the error of E_R represents a statistically estimated deviation.

A typical pair of near-field optical images is presented in figures 11(b) and (c). For telecom wavelengths, the SPP propagation length is increased up to $\approx$200 μm. Figure 11(c) features a strong SPP beam propagating away from the slit in the direction opposite to the array and thereby demonstrating unidirectional SPP excitation. Averaged results and estimated errors for E_R (previously reported in [23]) are rendered in figure 11(d). Notice that the validity of our proposal is now tested in a different way: for a given slit-to-array separation, E_R is measured within the wavelength range 1500–1620 nm, so that the phase difference described by (1) is changed with the increasing wavelength, providing the conditions for constructive or destructive interference. Obviously, this spectral dependence of the efficiency is different for different slit-to-array separations, and we support that experimentally. For the case of the sample with $d = P + P/2 = 1125$ nm, E_R decreases as the wavelength increases (with the only exception of a sharp peak at 1520 nm), evolving from a favorable regime ($E_R \approx 2$) to one in which coupling into SPPs is clearly diminished by the array ($E_R < 1$). Conversely, $E_R \approx 2$ for the sample with $d = 3P/4 = 562$ nm all over the range. As can be seen, the comparison between experiments and modal expansion calculation is rather satisfactory.

Finally, we have to mention that the proposed approach for the excitation of localized unidirectional SPP beams can also be combined with the appropriate design modifications to create functional components for SPP focusing to a spot or tuning the SPP beam divergence. If $E_R \geqslant 2$ is expected for a given slit + array set, its circular bending may produce a converging Gaussian beam whose waist length and radius can be adjusted by means of the curvature. Several curved SPP focusers have been previously achieved [35]–[39], but we find the mirror-blocked back-propagation to be a plus. Although the rigorous modelling of SPP coupling at curved structures is rather complicated and falls out of the scope of the present work, we expect (9) to still provide a good estimation for the proper design of the structure, at least as a starting point. On that assumption, we have fabricated several samples consisting of an arc-of-a-circle slit flanked by the corresponding array of parallel bent grooves (see figures 12(a)–(c)). Geometrical parameters a_0, a, w and P are the same as in figure 11, whereas slit-to-array distance is set to $d = 3P/2 = 1125$ nm.

As shown in figures 12(d)–(f), the effect of SPP launching and focusing can be appreciated already at the stage of far-field adjustment due to weak out-of-plane SPP scattering by surface roughness. Near-field images of SPP excitation on those structures recorded at free-space wavelength of 1520 nm are presented in figure 13. These images clearly demonstrate the property of a curved slit to excite a convergent SPP beam, with the effect being sufficiently enhanced due to the side grooves (cf [36, 37]). With the smallest radius of curvature (30 μm), focusing to a confined spot having size 3×3 μm^2 is observed (see the cross-cuts in the lower left panel of figure 13). The SPP beams excited on the less curved structures feature an extended waist (figures 13(b) and (c)), which scales (at least visually) according to expectations, providing a wider, and hence less divergent, SPP beam. That might be useful for particular applications, e.g. in sensing of elongated biological samples or in coupling to low-numerical-aperture waveguides.

IOP Institute of Physics DEUTSCHE PHYSIKALISCHE GESELLSCHAFT

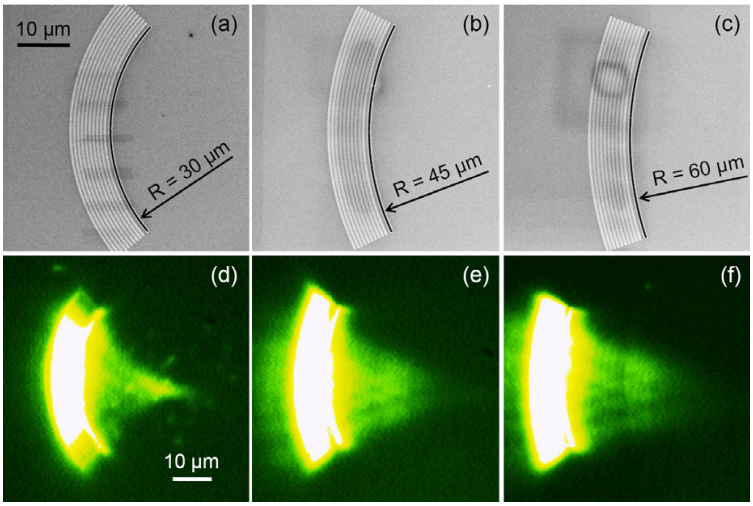

Figure 12. (a) Scanning electron micrograph of the curved structure, characterized by slit and groove widths of 400 and 200 nm, respectively, groove periodicity $P = 750$ nm, groove depth $w = 100$ nm and slit–groove distance $d = 1125$ nm. Film thickness $h = 280$ nm, curvature radius $R = 30\,\mu$m and slit chord length $L = 40\,\mu$m. (b) and (c) Same for $R = 45\,\mu$m and R = 60 μm. (d)–(f) Far-field images of SPPs excited on the structures (a), (b) and (c), respectively, recorded with a charge-coupled device camera.

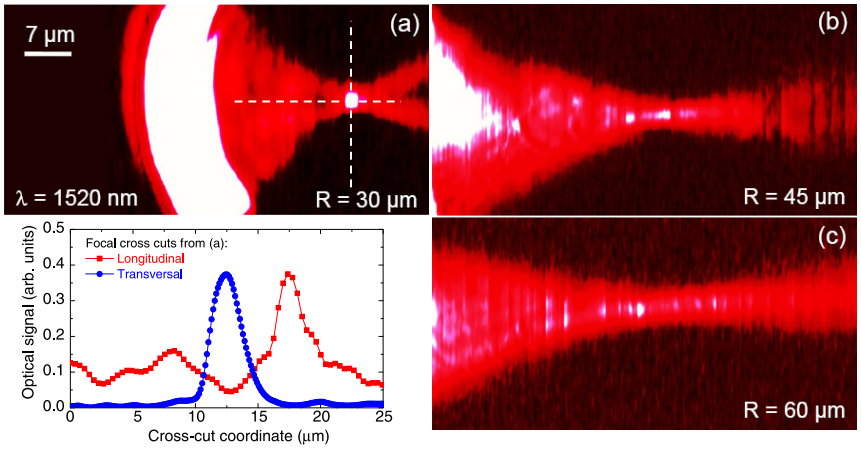

Figure 13. (a)–(c) Near-field images (size $64 \times 32\,\mu$m^2) of SPPs excited on the structures in figure 12 at $\lambda = 1520$ nm. Lower left panel depicts cross cuts obtained from (a) by dissecting the SPP focal spot along longitudinal and transversal directions.

5. Conclusions

In conclusion, we have studied the SPP coupling-in at sub-wavelength apertures with back-side illumination, presenting a novel proposal for the modulation of such a coupling-in by means of a finite array of grooves. Our approach is based on a simple wave interference model that, irrespective of the simplified description of some of the physics involved, has been found to be in good agreement with both sophisticated computer simulations and experimental measurements at NIR and telecom ranges. We find this to constitute a stimulating challenge for further developments on a wide range of SPP devices.

Acknowledgments

Financial support by the EU (project FP6-2002-IST-1-507879) and Spanish MEC (project MAT2005-06608-C02-02) is gratefully acknowledged. We thank J-Y Laluet for technical assistance.

References

[1] Raether H 1988 *Surface Plasmons* (Berlin: Springer)
[2] Barnes W L, Dereux A and Ebbesen T W 2003 *Nature* **424** 824
[3] Maier S A 2005 *Curr. Nanosci.* **1** 17
[4] Ozbay E 2006 *Science* **311** 189
[5] Weeber J C, Krenn J R, Dereux A, Lamprecht B, Lacroute Y and Goudonnet J P 2001 *Phys. Rev.* B **64** 045411
[6] Krenn J R, Ditlbacher H, Schider G, Hohenau A, Leitner A and Aussenegg F R 2003 *J. Microsc.* **209** 167
[7] Weeber J C, Lacroute Y, Dereux A, Devaux E, Ebbesen T W, González M U and Baudrion A L 2004 *Phys. Rev.* B **70** 235406
[8] Gómez-Rivas J, Kuttge M, Kurz H, Haring-Bolivar P and Sánchez-Gil J 2006 *Appl. Phys. Lett.* **88** 082106
[9] Bozhevolnyi S I, Volkov V S, Devaux E, Laluet J Y and Ebbesen T W 2006 *Nature* **440** 508
[10] González M U, Weeber J C, Baudrion A L, Dereux A, Stepanov A L, Krenn J R, Devaux E and Ebbesen T W 2006 *Phys. Rev.* B **73** 155416
[11] Otto A 1968 *Z. Phys.* **216** 398
[12] Lamprecht B, Krenn J R, Schider G, Ditlbacher H, Salerno M, Felidj N, Leitner A, Aussenegg F R and Weeber J C 2001 *Appl. Phys. Lett.* **79** 51
[13] Ritchie R H, Arakawa E T, Cowan J J and Hamm R N 1968 *Phys. Rev. Lett.* **21** 1530
[14] Ditlbacher H, Krenn J R, Felidj N, Lamprecht B, Schider G, Salerno M, Leitner A and Aussenegg F R 2002 *Appl. Phys. Lett.* **80** 404
[15] Sönnichsen C, Duch A C, Steininger G, Koch M, von Plessen G and Feldmann J 2000 *Appl. Phys. Lett.* **76** 140
[16] Devaux E, Ebbesen T W, Weeber J C and Dereux A 2003 *Appl. Phys. Lett.* **83** 4936
[17] Yin L, Vlasko-Vlasov V K, Rydh A, Pearson J, Welp U, Chang S H, Gray S K, Schatz G C, Brown D E and Kimball C W 2004 *Appl. Phys. Lett.* **85** 467
[18] Popov E, Bonod N, Nevière M, Rigneault H and Lenne P F 2005 *Appl. Opt.* **44** 2332
[19] Agrawal A, Cao H and Nahata A 2005 *New J. Phys.* **7** 249
[20] Chang S H, Gray S K and Schatz G C 2005 *Opt. Express* **13** 3150
[21] Lalanne P, Hugonin J P and Rodier C 2005 *Phys. Rev. Lett.* **95** 263902
[22] Aigouy L, Lalanne P, Hugonin J P, Julié G, Mathet V and Mortier M 2007 *Phys. Rev. Lett.* **98** 153902
[23] López-Tejeira F *et al* 2007 *Nat. Phys.* **3** 324
[24] López-Tejeira F, García-Vidal F J and Martín-Moreno L 2005 *Phys. Rev.* B **72** 161405

[25] López-Tejeira F, García-Vidal F J and Martín-Moreno L 2007 *Appl. Phys.* A **89** 251
[26] Taflove A and Hagness S C 2000 *Computational Electrodynamics: The Finite-Difference Time-Domain Method* (Boston: Artech House)
[27] Jackson J D 1975 *Classical Electrodynamics* 2nd edn (New York: Wiley)
[28] Arfken G 1985 *Mathematical Methods for Physicists* 3rd edn (San Diego: Academic)
[29] García-Vidal F, Rodrigo S G and Martín-Moreno L 2006 *Nat. Phys.* **2** 790
[30] Lalanne P and Hugonin J 2006 *Nat. Phys.* **2** 551
[31] Kitson S C, Barnes W L and Sambles J R 1996 *Phys. Rev. Lett.* **77** 2670
[32] Martín-Moreno L, García-Vidal F J, Lezec H J, Degiron A and Ebbesen T W 2003 *Phys. Rev. Lett.* **90** 167401
[33] Vial A, Grimault A, Macias D, Barchesi D and de la Chapelle M 2005 *Phys. Rev.* B **71** 085416
[34] Horcas I, Fernández R, Gómez-Rodríguez J, Colchero J, Gómez-Herrero J and Baró A M 2007 *Rev. Sci. Instrum.* **78** 013705
[35] Nomura W, Ohtsu M and Yatsui T 2005 *Appl. Phys. Lett.* **86** 181108
[36] Yin L, Vlasko-Vlasov V K, Pearson J, Hiller J M, Hua J, Welp U, Brown D E and Kimball C W 2005 *Nano Lett.* **5** 1399
[37] Liu Z, Steele J M, Srituravanich W, Pikus Y, Sun C and Zhang X 2005 *Nano Lett.* **5** 1726
[38] Offerhous H L, van der Bergen B, Escalante M, Segerink F B, Korterik J P and van Hulst N F 2005 *Nano Lett.* **5** 2144
[39] Steele J M, Liu Z, Wang Y and Zhang X 2006 *Opt. Express* **14** 5664

Chapter 5

Efficiency of local SP excitation on ridges

PHYSICAL REVIEW B **78**, 115115 (2008)

Efficiency of local surface plasmon polariton excitation on ridges

I. P. Radko,[1,*] S. I. Bozhevolnyi,[2,†] G. Brucoli,[3] L. Martín-Moreno,[3] F. J. García-Vidal,[4] and A. Boltasseva[5]
[1]*Department of Physics and Nanotechnology, Aalborg University, Skjernvej 4A, DK-9220 Aalborg Øst, Denmark*
[2]*Institute of Sensors, Signals and Electrotechnics, University of Southern Denmark, Niels Bohrs Allé 1, DK-5230 Odense M, Denmark*
[3]*Departamento de Fisica de la Materia Condensada-ICMA, Universidad de Zaragoza, E-50009 Zaragoza, Spain*
[4]*Departamento de Física Teórica de la Materia Condensada, Universidad Autónoma de Madrid, E-28049 Madrid, Spain*
[5]*Department of Photonics Engineering, Technical University of Denmark, Building 345v, DK-2800 Kongens Lyngby, Denmark*
(Received 3 June 2008; revised manuscript received 23 August 2008; published 19 September 2008)

The issue of efficient local coupling of light into surface plasmon polariton (SPP) modes is an important concern in miniaturization of plasmonic components. Here we present experimental and numerical investigations of efficiency of local SPP excitation on gold ridges of rectangular profile positioned on a gold film. The excitation is accomplished by illuminating the metal surface normally with a focused laser beam. Wavelength dependence and dependence of the efficiency on geometrical parameters of ridges are examined. Using leakage radiation microscopy, the efficiency of ~20% is demonstrated experimentally. Numerical simulations based on Green's tensor approach are in good agreement with the experiment and allow suggesting an optimization of parameters for improving the efficiency of SPP excitation.

DOI: 10.1103/PhysRevB.78.115115 PACS number(s): 42.82.Et, 73.20.Mf, 78.67.Bf, 42.25.Fx

I. INTRODUCTION

Plasmonics is a branch of nanophotonics that is concerned with manipulation of surface plasmon polaritons (SPPs) at nanoscale by means of specifically tailored metal structures. A great interest in this area is explained by two very interesting and promising applications for SPPs: integrated plasmonics and nanosensing. Integrated plasmonics, in contrast to integrated optics, operates with SPP waves, which can be squeezed much better than light, giving a possibility for high integration and in turn transmitting the signal much faster than electric current does. This provides a technology capable to replace electrical-circuit interconnections, which are strongly speed limited by the *RC* delay,[1] with plasmonic ones limited merely by the SPP frequency.[2,3] Moreover, plasmonics can bridge microscale photonics and nanoscale electronics.[2] Use of SPPs for nanosensing exploits surface plasmon resonances, which can be frequency shifted due to the presence of a substance being sensed as well as due to structure geometry. Furthermore, the latter, if chosen appropriately, can lead to an enormous field enhancement increasing otherwise very weak Raman signal.[4] Both applications require high miniaturization of the components involved, and the issue of efficient *local* light coupling into SPP modes is an important concern.

A very well-known and widely used technique for excitation of SPPs is Kretschmann configuration. If a metal film illuminated from below is of appropriate thickness, and a parallel beam is used as a light source, almost all the incident power can be transmitted into plasmons, meaning that the efficiency of light to SPP coupling reaches nearly 100%. However, it is not a local excitation since a parallel beam assumes its width to be at least a few hundreds of microns, whereas plasmonic applications are in lack of efficient compact sources of SPPs of the several-wavelength size. Moreover, the propagation length of a SPP beam along such a metal film is twice shorter than along an opaque one[5] due to the additional radiation losses into the substrate, which in most cases is undesirable. Otto configuration, which in common with Kretschmann one uses a similar principle of evanescent coupling, bears the same disadvantage of nonlocal excitation.

A number of configurations have been developed for local light-SPP coupling.[6] Among them are excitation using illumination through a probe of a scanning near-field optical microscope[7] by a highly focused laser beam[8,9] or by a radially polarized Bessel beam[10] and excitation at discontinuities of a metal film,[11] launching surface plasmons through an array of nanoholes,[12] through a subwavelength slit supplemented with a periodic set of grooves[13] or by a surface protrusion defect in form of a particle or a single ridge[14] as well as by a periodic set of those.[15] The efficiency of light-SPP coupling, defined as the ratio of SPP power to that of light, for some configurations has been evaluated both experimentally and numerically.[9,10,15–17] The efficiency of the techniques that use radially polarized Bessel or highly focused parallel beams can be quite high.[9,10] But apart from the already mentioned disadvantage of use of thin metal films, those methods, especially the former one, produce SPPs with virtually all directions of their k vectors. This is very impractical for integrated plasmonics operating with SPP beams—laterally confined SPP waves with their k vectors lying in a small range of directions (usually considerably below a radian)—but might be useful for nanosensing. In the work of Ditlbacher *et al.*,[15] the efficiency of SPP excitation mediated by gold ridges was studied. By illuminating the structures with a focused laser beam incident normally to the surface, two SPP beams propagating in opposite directions were excited. With only three ridges placed periodically on a gold film, the efficiency of light coupling into a single SPP beam was found to be ~8%. This is already a very good result if one bears in mind that it is a local coupling configuration, and such commercial devices in serial production could be virtually fabricated on a microchip. A very recent study of light coupling to SPP for a single subwavelength hole in a gold film[16] revealed the efficiency of up to 28%. Note, though, that this is the value normalized with respect to the

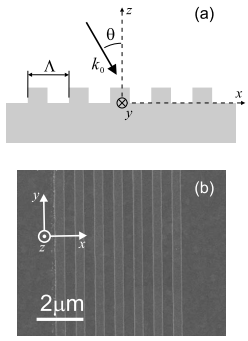

FIG. 1. (a) Geometry of the configuration under study and coordinate system. (b) Scanning electron microscope image of a typical structure under investigation. In this case it is a set of seven periodically arranged ridges. Period is 800 nm.

power incident onto the hole area, meaning that the absolute efficiency (normalized with respect to the total incident power) is considerably smaller. In our further discussions we shall operate with absolute values of efficiency. Note that a possibility of grating geometry optimization has been investigated numerically.[17] It was shown that a grating of indentations is more efficient than a grating of protrusions and an optimization of groove depth and width results in the coupling efficiency of 16%–22% to a single SPP beam.

This paper reports on the capability to optimize the ridge configuration for SPP excitation, found already promising,[15] with respect to its efficiency. We chose our structures to have a form of protrusions rather than indentations because ridges are easier to fabricate using electron-beam lithography (EBL), a technique which is more available than focused ion beam required for grooves. We tried to optimize the geometrical parameters of an individual ridge (width and height), the number of those in a periodic array, as well as the working wavelength for a given array period. The results presented were obtained both numerically and experimentally.

II. INVESTIGATION TECHNIQUES

A. Structures under investigation and experimental technique

We consider single ridges and periodic sets of those on top of a gold film illuminated with a focused laser beam. In the case of multiple ridges, the interaction between light and SPPs is achieved by coupling through the grating[5] and can be described approximately by the condition of momentum conservation,

$$\vec{k}_{\mathrm{SPP}}^{\parallel} = \vec{k}_0^{\parallel} + \vec{u}_x \frac{2\pi}{\Lambda} n, \tag{1}$$

where $\vec{k}_{\mathrm{SPP}}^{\parallel}$ and $\vec{k}_0^{\parallel}$ denote the wave-vector components in the (x,y) plane [see Fig. 1(a)] of the scattered SPP and the incident light, respectively, Λ is the grating period, and n is an integer. Since the grating momentum has only x component, we consider light incidence in the (x,z) plane, hence $\vec{k}_0^{\parallel} = \vec{u}_x k_0 \sin\theta$ and Eq. (1) can be rewritten as

$$k_{\mathrm{SPP}} = k_0 \sin\theta + nG, \tag{2}$$

with G denoting the grating momentum $2\pi/\Lambda$. As mentioned in Sec. I, excitation of laterally confined SPP waves is of most practical importance, therefore we need to focus the incident beam to a spot. On the other hand, we would like to have relatively small divergence of the excited SPP beam. Both conditions can be satisfied if we require that the SPP propagation length be of the order of the Rayleigh length of the SPP Gaussian beam, which gives the diameter of several microns for our wavelength range (see below). We use a 20-fold objective [numerical aperture (NA=0.4)], which fits well for these purposes. Due to the short working distance of the objective, the normal incidence of light is the only possibility for our configuration, thus from the Eq. (2) we obtain an approximate condition for the grating period, which should be a multiple of the SPP wavelength.

All structures were fabricated by EBL on a resist layer spun on top of a 50-nm-thick gold film on a quartz substrate, evaporation of a second gold layer, and subsequent liftoff. A scanning electron microscope image of a typical structure used in our investigations can be seen in Fig. 1(b).

The number of ridges to be used for SPP excitation is changing from 1 (single-ridge configuration) to at most 19. To find the exact optimum relation between the illumination wavelength and the grating period, it is enough to change only one of those parameters, and we choose to change the wavelength with the periodicity of ridges being fixed at $\Lambda = 800$ nm. Because of limitations of EBL the height of the structures cannot be changed within a sample, therefore in the experiment all ridges are 50 nm high, although, in numerical simulations it is a variable parameter.

To launch SPPs, we illuminate our structures with a tunable (wavelength range 700–860 nm) Ti:sapphire laser's Gaussian beam at normal incidence. Using the 20-fold objective, the beam is focused to a spot with diameter estimated to be $\sim(5\pm0.5)$ μm (at the level $1/e^2$ of intensity). Since the structure under investigation is homogeneous along the y direction, only x component of the incident field will contribute into SPPs. Therefore the polarization of the incident laser beam is perpendicular to the ridges. In this case two SPP beams are excited propagating in opposite directions away from the structure. Note that in most application configurations only one of them can be used. For this reason we define the light-plasmon coupling efficiency as the ratio between the power carried by one of the SPP beams and that of the incident laser illumination, i.e., the percentage of power transferred from light into a SPP beam. In other words, we find a *unidirectional* SPP excitation efficiency. Note also that with extended structures (such as periodic set of ridges) the efficiency depends substantially on the position of the illumination spot. In this case we search for the position that gives the maximum efficiency. It is this unidirectional efficiency that we call the light-plasmon coupling efficiency or the SPP excitation efficiency.

To estimate the magnitude of the efficiency, we measure the power of the leakage radiation (LR) from the excited SPP

beam into the glass substrate. The power of the LR is in strict relation with that of the SPP.[18] So, if the metal film thickness and the SPP wavelength are known, it is easy to evaluate the power carried by a SPP beam from the measured power of the corresponding LR. The random error of all measurements discussed in this paper is estimated to be ~15%. A setup for making LR measurements is well known and described in details elsewhere.[19]

B. Calculation technique

All calculations are based on the two-dimensional (2D) electromagnetic Green's tensor (GT) approach. The general theory and the solution technique have been developed previously.[20] The air-gold interface is set in the (x,y) plane and the ridges are infinite along the y axis, and thus all the properties are invariant in this direction. If the incident electric field propagates in the (x,z) plane and has p polarization [see Fig. 1(a)], then the total and the scattered fields will keep propagating in the (x,z) plane with the same polarization. That allows us to assume that the system can be solved in a 2D subspace $\mathbf{r}=(x,0,z)$ excluding the y dependence in the calculations. For the incident electric field we assume (i) $E_y^{\text{in}}=0$ and (ii) $E_x^{\text{in}}(x,z)=e^{-(x-x_0)^2/\sigma^2}E_x^{\text{in}}(z)$; i.e., the field has Gaussian profile only in the x direction. Even though y components of the incident electric field in the experiment are nonzero with relatively weak focusing ($\sigma=2.5$ μm), they are negligible.[21] Since the thickness of the gold film in the experiment (of 50 nm) is comparable to its skin depth, we approximate the gold slab with a semi-infinite gold half space. Let the dielectric constants of gold (as well as the gold ridges) and air be ϵ and 1, respectively. When a system formed by two semi-infinite half spaces (air and gold) with embedded scatterers (ridges) at the interface is illuminated with an incident electric field $\mathbf{E}_0(\mathbf{r})$, the total field $\mathbf{E}(\mathbf{r})$ is given, according to Eq. (8) of Ref. 20, by the volume-integral equation

$$\mathbf{E}(\mathbf{r})=\mathbf{E}_0(\mathbf{r})+k_0^2\int_A(\epsilon-1)\mathbf{G}_{2D}(\mathbf{r},\mathbf{r}')\mathbf{E}(\mathbf{r}')d\mathbf{r}', \qquad (3)$$

where the integration runs only over the scatterers section A. $\mathbf{G}_{2D}(\mathbf{r},\mathbf{r}')$ is the 2D GT that gives the field at a point $\mathbf{r}$ generated by an infinite line source extending in the y direction centered at an arbitrary point $\mathbf{r}'$. Equation (3) is a combination of the physical constraints governing our system that is the Maxwell equations and the boundary conditions.

The solution is found in a two-step process. (i) First, the electric field inside every ridge of the grating is computed by solving Eq. (3) for points $\mathbf{r}$ being placed inside the ridges. The calculation involves the GT connecting any two points inside the scatterers, which can be found (in direct space) in the integral representation[22] and must be attained numerically. The integration technique has been described in details in Appendix B of Ref. 23. (ii) The field outside the ridges can then be found using the self-consistent field inside the ridges determined in the first step. Calculating the excitation efficiency only involves the analytical asymptotic approximation of the GT for the in-plane far-field zone,[22,23] $\mathbf{G}_{2D}(x-x'\gg\lambda,z\sim 0,z'\sim 0)\rightarrow\mathbf{G}_{SPP}$,

$$\mathbf{E}_{SPP}(\mathbf{r})=k_0^2\int_A(\epsilon-1)\mathbf{G}_{SPP}(\mathbf{r},\mathbf{r}')\mathbf{E}(\mathbf{r}')d\mathbf{r}'. \qquad (4)$$

This GT describes the coupling between the field inside the ridges and the SPP field at remote points near the surface plane.

III. EXPERIMENTAL AND NUMERICAL RESULTS

A. Wavelength dependence of coupling efficiency

First, we investigated the wavelength dependence of the SPP excitation efficiency. For this purpose a 50-nm-high and 150-nm-wide single gold ridge was fabricated. A unidirectional SPP excitation efficiency was measured in the wavelength range 750–860 nm and found to decrease rapidly with the increasing wavelength. The most basic description of SPP launching in this configuration relies on a dipole scattering of light on the ridge. Its two sharp edges separated by 50 nm act as a dipole in the incident electric field oriented perpendicular to the ridge. Since the size of this dipole is considerably smaller than the wavelength, Rayleigh scattering gives an adequate description of the wavelength dependence of scattered light intensity.[24] We plotted the experimentally obtained values along with the numerical data in a double-logarithmic chart to find the exponent in the power-law dependence [Fig. 2(a)]. Both plots are fitted with a straight line, which yields the magnitudes of the assumed exponents −5.4 and −4.5 for the experimental and numerical data, respectively. One can see that the agreement is fairly good both between each other and with Rayleigh scattering, which scales as a power of −4 of the wavelength. One should hardly expect the exact correspondence between the experimental and numerical data because the simulated results depend much on the dielectric constant of metal (which is known to depend on the fabrication) as well as on the exact profile of the ridge, which is not ideally rectangular in the experiment.

In order to increase the efficiency, it seems reasonable to use several ridges arranged periodically. As mentioned in Sec. II A, the period should be close to the SPP wavelength, but the precise value is not obvious. We investigated the wavelength dependence of light-plasmon coupling efficiency for structures composed of up to six ridges having the same geometrical parameters as in the previous experiment [Fig. 2(b)]. Having the feature of a single-ridge dependence (to decrease rapidly with wavelength), the efficiency is noticeably enhanced near the wavelength of 790 nm where the coherently excited (on different ridges) SPP waves interfere with each other constructively increasing the light-plasmon coupling. Note that while the number of ridges used is increasing, this effect starts to be more pronounced. For one ridge we obtained a unidirectional efficiency around 0.6% at the wavelength 800 nm, which is almost four times less than that declared in Ref. 15. This is due to the difference in laser illumination spot size (~5 μm in our case vs 1 μm in Ref. 15). Although better focusing is preferred with a few ridges, a larger beam size might be more advantageous with the considerable number of ridges (10–20) since more scatterers are involved in the excitation process.

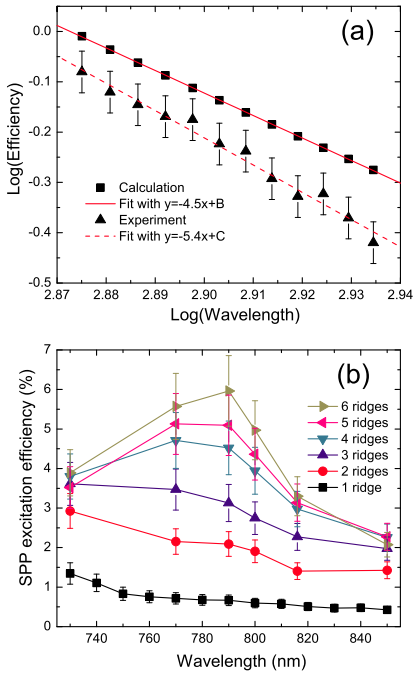

FIG. 2. (Color online) (a) Efficiency of SPP excitation on 50-nm-high and 150-nm-wide gold ridge versus the free-space wavelength used for excitation plotted in double-logarithmic scale along with a linear fit. (b) Efficiency of SPP excitation on sets of periodically arranged 50-nm-high 150-nm-wide gold ridges versus the free-space wavelength measured for the different number of ridges composing the grating. Separation between ridges is $\Lambda = 800$ nm.

B. Dependence on geometrical parameters of ridge

Finding the optimum geometrical parameters of an individual ridge is important because, as we show in this section, geometrical optimization can sufficiently increase the efficiency of light-plasmon coupling. We performed numerical simulations of SPP excitation on a single ridge whose height is varying in the range 50–230 nm and width, in the range of 200–600 nm, and calculated its efficiency [Fig. 3(a)]. With only small difference, ridges of all heights feature maximum efficiency when the width is close to 350 nm, i.e., almost half of the wavelength. The maximum achievable efficiency for every given height is then plotted in Fig. 3(b). One can see almost a sixfold increase in the efficiency with the height growing from 50 up to 130 nm, where it reaches its maximum.

We checked the width dependence of excitation efficiency experimentally also using illumination at the wavelength 800 nm. The ridge height was fixed at 50 nm. We tested configurations with one, three, and five ridges aligned periodically (period $\Lambda = 800$ nm) in the two latter cases [Fig. 3(c)]. The experimental data exhibit maximum efficiency for the ridge

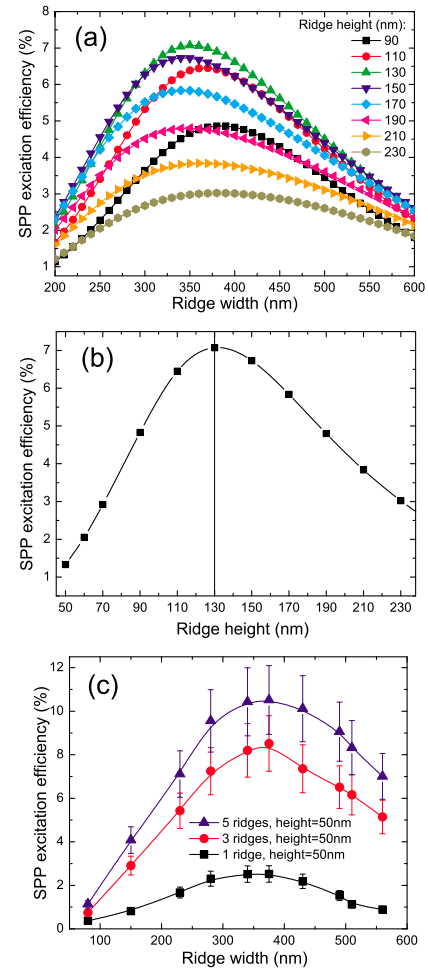

FIG. 3. (Color online) (a) Calculation of efficiency of SPP excitation on a single ridge versus its width. Different curves show data for different ridge heights. (b) Calculation of maximum attainable efficiency (with all possible ridge widths) of the SPP excitation on a single ridge versus its height. (c) Experimental results for dependencies of SPP excitation efficiency on the ridge width. The ridge height is fixed at 50 nm. Three curves show three sets of measurements accomplished on a single ridge and on three and five ridges aligned in gratings with the period $\Lambda = 800$ nm. The free-space wavelength is 800 nm both in calculations and in the experiment.

width close to 350 nm, which is in agreement with the numerical simulations. The figure also demonstrates that the optimum width is not changing for the increasing number of ridges at least within a small quantity. Note that the fact that we obtained larger efficiency experimentally, than it is pre-

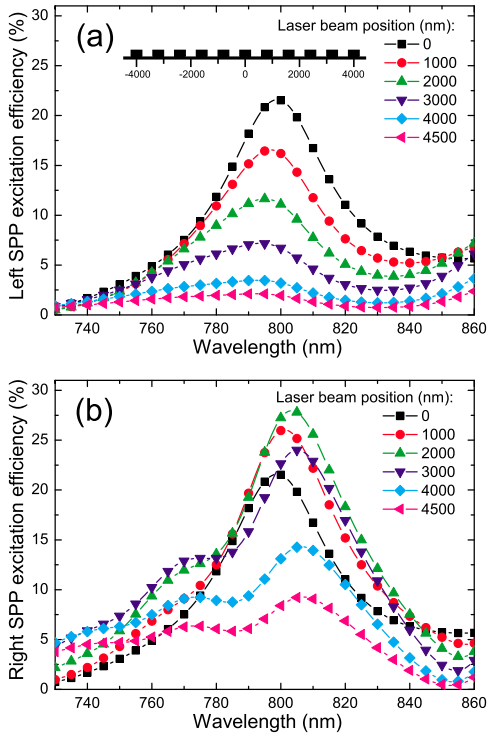

FIG. 4. (Color online) Numerical results for wavelength dependence of efficiency of SPP excitation on 11 ridges (height=50 nm and width=280 nm). Different positions of a laser beam (diameter=5 μm) illuminating the sample are shown by different curves. Calculations accomplished for SPP propagating (a) to the left and (b) to the right from the grating. Inset of the panel (a) shows the geometry and coordinate system.

dicted numerically for a 50-nm-high ridge, can be explained by a slightly smaller laser-beam diameter used in the experiment.

C. Optimum wavelength for excitation on ridges

As we already mentioned, one of the ways to increase the efficiency of excitation is to use a periodic set of ridges. However, the optimum period is not necessarily equal to the SPP (or free-space) wavelength. To get more insight into that, we investigate arrays of ridges with the fixed period of $\Lambda=800$ nm and change the laser-beam wavelength instead since array period cannot be changed in the experiment.

First, we investigated numerically SPP excitation on a grating composed of 11 ridges having width of 280 nm and height of 50 nm. The diameter of the modeled laser beam is 5 μm. We placed the zero of the coordinate system to the center of the grating [inset of Fig. 4(a)]. Then we performed a scan of the laser beam from the center toward increasing coordinates evaluating the powers carried by the two SPP beams propagating in opposite directions for different wavelengths [Figs. 4(a) and 4(b)]. Expectedly, the efficiency drops down monotonously for the left-propagating SPP beam [see the inset of Fig. 4(a) for the geometry] with the laser beam moving from the center of the grating to the right [Fig. 4(a)]. On the contrary, the efficiency for the right-propagating SPP increases first, reaching the maximum at the coordinate ~2000 nm, and then monotonously decreases [Fig. 4(b)]. We will get back to this behavior in Sec. III D, whereas now a more important result is the wavelength where the maximum efficiency is observed: it is 805 nm. Note that in this optimum case, the grating period of 800 nm is between the free-space wavelength 805 nm and the corresponding SPP wavelength ~789 nm.

In the experiment, we investigated two gratings composed of 7 and 11 ridges of the width 200 nm and 280 nm each, respectively. Instead of scanning the laser beam across the gratings, we were searching the position with the maximum achievable efficiency and then picked that efficiency value to the chart. Thus, the way it was measured gives an envelope of all the curves in Fig. 4(b). The result obtained is shown in Fig. 5(a) together with the envelope for comparison. The lower curve yields the optimum wavelength of 790 nm, which repeats the result shown in Fig. 2(b). The experimental curve for the 11-ridge gratings shows that the optimum wavelength shifts toward higher values with the increasing number of ridges. Comparison with the envelope of the curves in Fig. 4(b) (obtained for the same geometry, i.e., 11 ridges of the width 280 nm and height 50 nm) shows good agreement in both the optimum wavelength and the general behavior of the spectrum. For lower wavelengths the experiment gives higher efficiencies. This is because the experimental structure always has small irregularities in the ridge periodicity, which makes the spectrum broader and, as a result, its wings higher.

A drift of the optimum wavelength with the increasing number of ridges can be also observed in another series of measurements where we investigated a dependence of light-SPP coupling efficiency on the number of ridges involved in the process [Fig. 5(b)]. The ridges participating in the excitation are 280 nm wide. First of all, at wavelengths far from the optimum one, the efficiency comes very quickly to saturation (730 and 770 nm) or even drops down (850 nm) with the number of ridges exceeding five. Second, for the small number of ridges (below seven) the optimum wavelength is somewhere around 800 nm but cannot be clearly defined: the gratings are broadband. However, with the increasing number of ridges, the wavelength dependence gets more pronounced: first, 800 nm is preferable (for 11 ridges) and then 810 nm (for 15 and more ridges). The two main conclusions are: (i) the optimum wavelength (or the optimum grating period for a given wavelength) is growing (diminishing) with the increasing number of ridges composing the grating and (ii) for a grating with large number of ridges the SPP wavelength corresponding to the optimum illumination is approaching the grating periodicity from the low-wavelength side. The latter means that there are two competing processes of electromagnetic interaction between ridges: one is on the dielectric (air) side and mediated by photons, and the other is

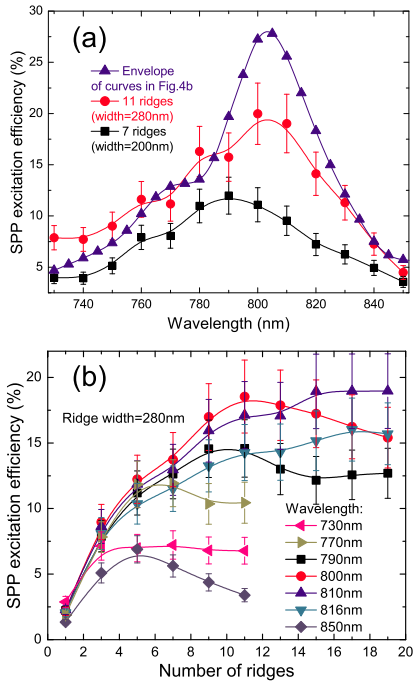

FIG. 5. (Color online) (a) Experimental results for wavelength dependence of efficiency of SPP excitation on two different gratings ($\Lambda=800$ nm) composed of 7 (height=50 nm and width=200 nm) and 11 ridges (height=50 nm and width=280 nm) plotted together with the envelope of curves shown in Fig. 4(b) for comparison. (b) Experimental results for efficiency of SPP excitation versus the number of ridges in the grating ($\Lambda=800$ nm) used for excitation. Ridge with height=50 nm and width=280 nm. Results obtained at different wavelengths are shown by different curves.

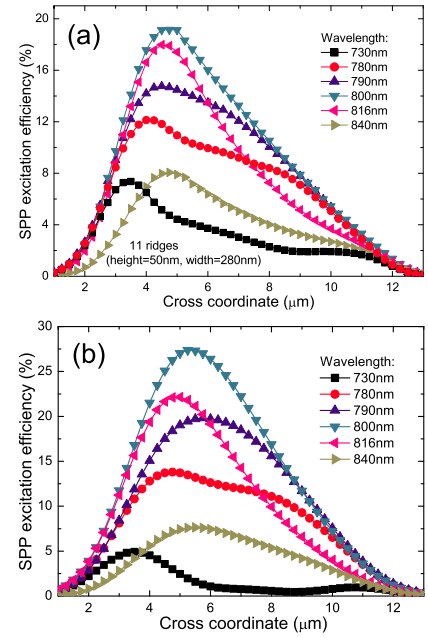

FIG. 6. (Color online) (a) Experimental and (b) numerical results for SPP excitation efficiency versus the position of a laser beam scanned across the grating ($\Lambda=800$ nm) composed of 11 ridges (height=50 nm and width=280 nm). In the experiment the grating extends approximately from 3 to 11 μm of the cross coordinate; in the numerical simulations this is the exact position of the grating. The error bars in (a) are omitted to not obscure the image.

on the metal side occurring through SPPs. To enhance each of those processes, the grating period equal to the corresponding wavelength is required, which sets the optimum period in between of them. As it turns out, however, the interaction through plasmons is stronger, and with the large number of ridges it takes over the process equating the optimum period with the SPP wavelength. One of the reasons that we obtained the maximum efficiency at $\lambda_0=810$ nm instead of 816 nm (corresponding to $\lambda_{SPP}=\Lambda=800$ nm) might be a small misalignment (of about 0.5°) of the objective focusing illumination onto the grating [see Eq. (2)].

D. Directionality of SPP excitation on periodic sets of ridges

We conclude our consideration of efficiency of light-SPP coupling on ridges by demonstrating the extent of asymmetry of surface plasmon beams excitation while using such structures. This gives an idea of the total (bidirectional) light-plasmon coupling efficiency and also demonstrates the sensitivity of efficiency to the position of the laser beam with respect to the illuminated structure.

For this purpose, we measure the efficiency while the laser beam is scanned across a grating [Fig. 6(a)]. Such profiles were recorded at several wavelengths. The grating was composed of 11 ridges (height=50 nm and width=280 nm). At two wavelengths—at which the highest efficiencies were obtained (800 and 816 nm)—the profiles feature a relatively sharp maximum. At the optimum wavelength the efficiency is very sensitive to the laser-beam position, which leads to a more unidirectional excitation. Assuming that the center of the grating is approximately positioned at $x=7$ μm, one can find the efficiency of SPP excitation on the farthest end of the grating while having a maximum at the nearest one: 7% versus 19% at $\lambda_0=800$ nm. For the wavelengths out of the resonance, the profiles possess a small plateau in the middle forming a shape reminding trapezium. At the wavelength 730 nm one can even notice a very small second local maximum on the other end of the grating.

Modeling of this geometry shows an excellent agreement [Fig. 6(b)] in curves' shape including the two local maxima at $\lambda_0=730$ nm. The explanation for the latter could be that out of the resonance the excitation on a fewer number of

ridges is more efficient than on the whole grating because the periodic set of ridges causes destructive interference. Therefore, moving the beam out of the grating excludes most of the ridges from the process, which turns out to be more favorable in this case.

IV. CONCLUSIONS

Summarizing, we have investigated numerically and experimentally the efficiency of SPP excitation on single ridges and on periodic sets of those. The variable parameters were wavelength of light used for excitation, ridges width and height, as well as the number of them in periodic arrangements. The maximum experimental unidirectional SPP excitation efficiency of about 20% was obtained for 11 ridges (width=280 nm and height=50 nm). Although the dependence of efficiency on ridge height was not investigated experimentally, numerical simulations show that it is an important parameter, which can lead to almost sixfold increase in efficiency for one ridge when changing the height from 50 to 130 nm. The optimum ridge width was found to be close to half the illumination wavelength but somewhat smaller. This is in agreement with the result obtained previously for another working wavelength.[17] For periodic sets of ridges used for SPP excitation, the SPP wavelength corresponding to the optimum free-space wavelength was found to be smaller than the ridge periodicity but approaching that with the increasing number of ridges.

It is difficult to extend the conclusions to systems distinct from the suggested one without thorough investigations. One can, however, conclude that efficient local excitation of SPPs is achievable with a moderately focused laser beam and only a few ridges. Regarding optimum parameters, it is clear that with the oblique incidence of the laser beam, the grating period and/or the excitation wavelength has to be adjusted according to Eq. (2). It is further expected that the ridge parameters (height and width) are mainly influenced by the choice of wavelength (most probably scaling with it linearly), but the precise values have to be found with detailed simulations.

Finally, we note that the value of efficiency of 20% found experimentally might be improved in the case of opaque metal film,[17] which prevents the excitation of SPPs on a metal-substrate interface. The higher value of ~28% obtained numerically for the same configuration is a good evidence of that. However, the use of opaque metal films will make the LR microscopy inapplicable for experimental investigations.

ACKNOWLEDGMENTS

This work was supported by the Danish Technical Research Council (Contract No. 26-04-0158), the European Network of Excellence, Plasmo-Nano-Devices (Contract No. FP6-2002-IST-1-507879), the Spanish MCyT under Projects No. MAT2005-06608-C02 and No. AP2005-55-185, and the NABIIT project (Contract No. 2106-05-033 from the Danish Research Agency).

*ilya@nano.aau.dk
†Also at Department of Physics and Nanotechnology, Aalborg University, Skjernvej 4A, DK-9220 Aalborg Øst, Denmark.

[1] R. W. Keyes, Proc. IEEE **89**, 227 (2001).
[2] R. Zia, J. A. Schuller, A. Chandran, and M. L. Brongersma, Mater. Today **9**, 20 (2006).
[3] W. L. Barnes, A. Dereux, and T. W. Ebbesen, Nature (London) **424**, 824 (2003).
[4] S. Lal, S. Link, and N. J. Halas, Nat. Photonics **1**, 641 (2007).
[5] H. Raether, *Surface Plasmons on Smooth and Rough Surfaces and on Gratings* (Springer-Verlag, Berlin, 1988).
[6] A. V. Zayats and I. I. Smolyaninov, J. Opt. A, Pure Appl. Opt. **5**, S16 (2003).
[7] B. Hecht, H. Bielefeldt, L. Novotny, Y. Inouye, and D. W. Pohl, Phys. Rev. Lett. **77**, 1889 (1996).
[8] H. Kano, S. Mizuguchi, and S. Kawata, J. Opt. Soc. Am. B **15**, 1381 (1998).
[9] H. Kano, D. Nomura, and H. Shibuya, Appl. Opt. **43**, 2409 (2004).
[10] Q. Zhan, Opt. Lett. **31**, 1726 (2006).
[11] L. Salomon, G. Bassou, H. Aourag, J. P. Dufour, F. de Fornel, F. Carcenac, and A. V. Zayats, Phys. Rev. B **65**, 125409 (2002).
[12] E. Devaux, T. W. Ebbesen, J.-C. Weeber, and A. Dereux, Appl. Phys. Lett. **83**, 4936 (2003).
[13] F. López-Tejeira *et al.*, New J. Phys. **10**, 033035 (2008).
[14] H. Ditlbacher, J. R. Krenn, N. Felidj, B. Lamprecht, G. Schider, M. Salerno, A. Leitner, and F. R. Aussenegg, Appl. Phys. Lett. **80**, 404 (2002).
[15] H. Ditlbacher, J. R. Krenn, A. Hohenau, A. Leitner, and F. R. Aussenegg, Appl. Phys. Lett. **83**, 3665 (2003).
[16] A.-L. Baudrion, F. de León-Pérez, O. Mahboub, A. Hohenau, H. Ditlbacher, F. J. García-Vidal, J. Dintinger, T. W. Ebbesen, L. Martín-Moreno, and J. R. Krenn, Opt. Express **16**, 3420 (2008).
[17] G. Lévêque and O. J. F. Martin, J. Appl. Phys. **100**, 124301 (2006).
[18] E. Kretschmann, Z. Phys. **241**, 313 (1971).
[19] A. Drezet, A. Hohenau, A. L. Stepanov, H. Ditlbacher, B. Steinberger, N. Galler, F. R. Aussenegg, A. Leitner, and J. R. Krenn, Appl. Phys. Lett. **89**, 091117 (2006).
[20] M. Paulus and O. J. F. Martin, Phys. Rev. E **63**, 066615 (2001).
[21] M. Mansuripur, J. Opt. Soc. Am. A **3**, 2086 (1986).
[22] T. Søndergaard and S. I. Bozhevolnyi, Phys. Rev. B **69**, 045422 (2004).
[23] A. Y. Nikitin, G. Brucoli, F. J. García-Vidal, and L. Martín-Moreno, Phys. Rev. B **77**, 195441 (2008).
[24] J. D. Jackson, *Classical Electrodynamics*, 3rd ed. (Wiley, New York, 1998).

Chapter 6

Unidirectional ridge excitation of SPs

Efficient unidirectional ridge excitation of surface plasmons

I. P. Radko,[1*] S. I. Bozhevolnyi,[1] G. Brucoli,[2] L. Martín-Moreno,[2] F. J. García-Vidal,[3] and A. Boltasseva[4]

[1] *Institute of Sensors, Signals and Electrotechnics, University of Southern Denmark, DK-5230 Odense M, Denmark*

[2] *Instituto de Ciencia de Materiales de Aragón and Departamento de Física de la Materia Condensada, CSIC-Universidad de Zaragoza, E-50009, Zaragoza, Spain*

[3] *Departamento de Física Teórica de la Materia Condensada, Universidad Autónoma de Madrid, E-28049 Madrid, Spain*

[4] *School of Electrical and Computer Engineering, Purdue University, Birck Nanotechnology Center, West Lafayette, IN 47907, USA*

[*] *Corresponding author: ilr@sense.sdu.dk*

Abstract: Using leakage-radiation microscopy, we characterize the efficiency of unidirectional surface-plasmon excitation with periodic (800 nm) arrays of 130-nm-high and 330-nm-wide gold ridges on a thin gold film illuminated with a focused (5-μm-wide) laser beam. We demonstrate that, at the resonant wavelength of 816 nm, the excitation efficiency of > 0.4 can be obtained with ≥ 5 ridges by adjusting the beam position. Conducting numerical simulations, we account for the experimental results and calculate the electric-field enhancement achieved near the gold surface.

OCIS codes: (240.6680) Surface plasmons; (230.1950) Diffraction gratings; (230.3120) Integrated optics devices; (250.5403) Plasmonics.

References and links

1. S. Lal, S. Link, and N. J. Halas, "Nano-optics from sensing to waveguiding," Nature Photon. **1,** 641–648 (2007).
2. J. N. Anker, W. P. Hall, O. Lyandres, N. C. Shah, J. Zhao, and R. P. Van Duyne, "Biosensing with plasmonic nanosensors," Nature Mater. **7,** 442–453 (2008).
3. R. Zia, J. A. Schuller, A. Chandran, and M. L. Brongersma, "Plasmonics: the next chip-scale technology," Materials Today **9,** 20–27 (2006).
4. T. W. Ebbesen, C. Genet, and S. I. Bozhevolnyi, "Surface-plasmon circuitry," Physics Today **May,** 44–50 (2008).
5. H. Raether, *Surface Plasmons on Smooth and Rough Surfaces and on Gratings* (Springer-Verlag, Berlin, 1988).
6. I. P. Radko, S. I. Bozhevolnyi, G. Brucoli, L. Martín-Moreno, F. J. García-Vidal, and A. Boltasseva, "Efficiency of local surface plasmon polariton excitation on ridges," Phys. Rev. B **78,** 115115 (2008).
7. H. Ditlbacher, J. R. Krenn, A. Hohenau, A. Leitner, and F. R. Aussenegg, "Efficiency of local light-plasmon coupling," Appl. Phys. Lett. **83,** 3665–3667 (2003).
8. A.-L. Baudrion, F. de León-Pérez, O. Mahboub, A. Hohenau, H. Ditlbacher, F. J. García-Vidal, J. Dintinger, T. W. Ebbesen, L. Martín-Moreno, and J. R. Krenn, "Coupling efficiency of light to surface plasmon polariton for single subwavelength holes in a gold film," Opt. Express **16,** 3420–3429 (2008).
9. L. B. Scaffardi, N. Pellegri, O. de Sanctis, and J. O. Tocho, "Sizing gold nanoparticles by optical extinction spectroscopy," Nanotechnology **16,** 158–163 (2005).
10. P. B. Johnson and R. W. Christy, "Optical constants of the noble metals," Phys. Rev. B **6,** 4370–4379 (1972).
11. E. D. Palik, *Handbook of Optical Constants of Solids* (Academic, New York, 1985).
12. I. P. Radko, S. I. Bozhevolnyi, A. B. Evlyukhin, and A. Boltasseva, "Surface plasmon polariton beam focusing with parabolic nanoparticle chains," Opt. Express **15,** 6576–6582 (2007).

13. L. Yin, V. K. Vlasko-Vlasov, J. Pearson, J. M. Hiller, J. Hua, U. Welp, D. E. Brown, and C. W. Kimball, "Subwavelength focusing and guiding of surface plasmons," Nano Lett. **5,** 1399–1402 (2005).
14. J.-Y. Laluet, E. Devaux, C. Genet, T. W. Ebbesen, J.-C. Weeber, and A. Dereux, "Optimization of surface plasmons launching from subwavelength hole arrays: modelling and experiments," Opt. Express **15,** 3488–3495 (2007).
15. J. T. Bahns, A. Imre, V. K. Vlasko-Vlasov, J. Pearson, J. M. Hiller, L. H. Chen, and U. Welp, "Enhanced Raman scattering from focused surface plasmons," Appl. Phys. Lett. **91,** 081104 (2007).

Plasmonics being concerned with manipulation of surface plasmon-polaritons (SPPs) using nanofabricated metal structures has attracted much attention due to potential applications in nanosensing and nanophotonics [1–4]. Both applications require high miniaturization of components involved, with the issue of efficient SPP excitation becoming increasingly important. Traditional Kretschmann and Otto configurations are known to be able to convert almost all incident light power into SPPs [5]. However, these techniques require (infinite) plane wave and thereby are not readily compatible with the demand for miniaturization. We have recently showed the possibility to efficiently convert a focused laser beam (at normal incidence) into an SPP beam (i.e., a laterally confined SPP wave possessing small divergence) using periodic set of metal ridges on top of a metal surface [6]. Using 50-nm-high and 280-nm-wide gold ridges we have achieved the SPP excitation efficiency (defined as the power ratio between an SPP beam propagating in a given direction and an incident laser beam) of ~ 0.2 at the wavelength of ~ 800 nm, which we believe is the best result obtained so far. We have also shown via numerical simulations that one can dramatically increase this efficiency by propitiously choosing the ridge dimensions found for this configuration to be ~ 130 nm in height and ~ 350 nm in width. In this letter we report on fabrication and investigation of ridge SPP couplers with optimized parameters [6].

The configuration for SPP excitation exploited in this work is essentially the same as that described in our previous paper [6] and was first introduced by Ditlbacher *et al* [7]. Straight 130-nm-high and 330-nm-wide gold ridges (of nominally rectangular profile) were fabricated using electron-beam lithography on the surface of a 50-nm gold film supported by a quartz substrate. The number of ridges in the configuration under investigation changes from one (single-ridge configuration) to 15 in steps of two with the period being fixed at $\Lambda = 800$ nm [Fig. 1(a)]. We used leakage-radiation microscopy (LRM) to both image the SPP propagation and measure the power of the excited SPP beam [6–8]. The illumination is accomplished by focusing a Gaussian laser beam (tunable wavelength range 700–860 nm) normally to the surface with a 20-fold objective (NA $= 0.4$) to a spot with a diameter estimated to be $\sim (5 \pm 0.5)\ \mu$m (at the level $1/e^2$ of intensity). The incident beam was linearly polarized in the direction perpendicular to the ridges [which run parallel to the y axis in Fig. 1(b)] resulting in the excitation of two SPP beams propagating in opposite directions, whose intensities strongly depended on the position of the illumination spot relative to the structure [Fig. 1(c)]. Note that unless otherwise stated, the SPP excitation efficiency refers to the SPP beam propagating to the left [i.e., towards negative x coordinates in Fig. 1(b)] from the structure.

The most basic description of SPP launching by periodic set of ridges (period Λ) relies on the momentum conservation: $k_{\mathrm{SPP}} = k_0 \sin\theta + nG$, where k_{SPP} and k_0 denote the wave-vector magnitudes of the excited SPP and incident light, respectively, θ is the angle of light incidence in the plane perpendicular to the ridges, n is an integer, and $G = 2\pi/\Lambda$ is the grating momentum [Fig. 1(b)]. Efficient SPP excitation (in the first grating order) at normal incidence requires thereby that the grating period should be equal to the SPP wavelength: $\Lambda = \lambda_{\mathrm{SPP}}$. In this case, the laser illumination scattered on different ridges generates coherent SPP waves, which interfere constructively with each other increasing the efficiency of SPP excitation. In the experiment, we used a discrete set of the laser (free-space) wavelengths centered at the wavelength of 816 nm

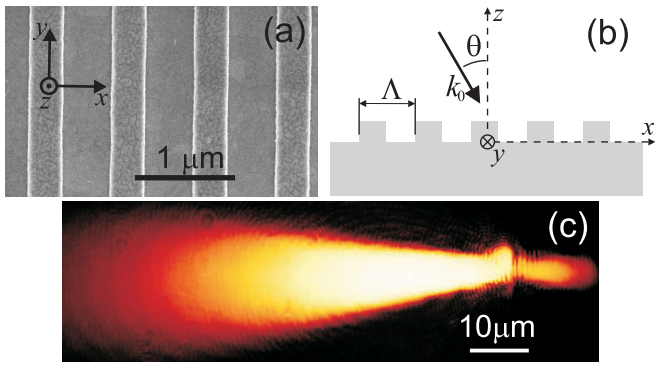

Fig. 1. (a) SEM image of a fragment of the fabricated structure consisting of 130-nm-high and 330-nm-wide ridges. (b) Geometry of the illumination configuration. (c) Typical LRM image of a strong SPP beam excited on the 11-ridge array on its left side. A much weaker SPP beam propagating to the right is also visible.

corresponding to $\lambda_{SPP} = \Lambda = 800$ nm [5]. For each wavelength and number of ridges, the incident laser beam was laterally adjusted [along x axis in Fig. 1(b)] so as to maximize the excited SPP beam power [Fig. 2(a)]. It is seen that the dependence of the SPP excitation efficiency on the number of ridges exhibits a rapid saturation [Fig. 2(a)], even more rapid than in the case of the 50-nm-high ridges (cf. with Fig. 5(b) in [6]). The highest efficiencies were measured at the free-space wavelength of 816 nm as expected. At this wavelength, the SPP excitation efficiency of 0.45 ± 0.06 was achieved with 11 ridges, reaching the level of > 0.4 already with five of them.

The excitation efficiency is very sensitive to the transverse position of laser beam relative to the grating [6], rendering the (practically) unidirectional SPP excitation [Fig. 1(c)]. We conducted the efficiency measurements while the laser beam was scanned across the 11-ridge array illuminated at the wavelength of 816 nm [Fig. 2(b)]. Taking into account that the array center is positioned at $x = 8$ μm, one can deduce the excitation efficiency, η, for the (unwanted) SPP beam propagating to the right when the left-propagating SPP beam is most efficiently excited. Since the highest efficiency of 0.45 is achieved at $x = 4.6$ μm, the corresponding efficiency for the right-propagating SPP beam should be (under the assumption of symmetric excitation configuration) the same as that for the left-propagating one at $x = 8 + (8 - 4.6) = 11.4$ μm, i.e. $\eta = 0.013$, which is ~ 35 times smaller than 0.45 [Fig. 2(b)]. We think that such an efficient suppression of the right-propagating SPP beam can be due to the second-order Bragg reflection from ridges, which redirects the SPP back into the desirable direction, as well as due to the (reciprocal) out-coupling of the propagating (over many ridges) SPP, which can be rather strong since the in-coupling is efficient.

Using a two-dimensional electromagnetic Green's tensor approach, we calculated [6] the corresponding dependence of SPP excitation for the nominal structure parameters [Fig. 2(b)]. There is a good agreement between the experimental and simulated dependencies in their shape, albeit the simulated SPP excitation is more unidirectional than that observed in the experiment, ensuring ~ 140 times more efficient SPP excitation to the left than that to the right. The latter is believed to be due to perfect geometry used in the numerical simulations, featuring identical ridges with exactly the same separation, whereas fluctuations in the geometrical parameters are to be expected only in the experiment. There is also a discrepancy in the maximum value of efficiency, which does not fall into the interval determined by measurement errors. This difference can be explained by deviations in the ridge parameters (in ridge shape and sizes) of

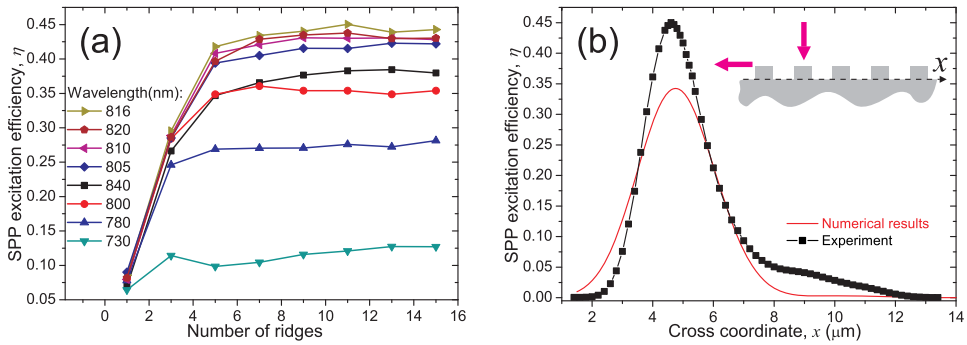

Fig. 2. (a) The maximum efficiency of SPP excitation obtained experimentally for different laser wavelengths as a function of number of ridges. The lines connecting the points are only to guide an eye. (b) Experimental and numerical results for the SPP excitation efficiency versus the position of a laser beam scanned across the 11-ridge array extending from $x = 4$ μm to $x = 12$ μm. Error bars both in (a) and (b) are omitted for clarity of presentation. The error of measurements is estimated to be $\sim 13\%$.

the fabricated structure from the nominal values. It is also known [9] that the dielectric constant of gold within ridges may be different from that reported in literature [10, 11].

Having realized such a high efficiency of (local) SPP excitation, we anticipated to also achieve the field enhancement near the gold surface with respect to the field of the incident laser beam. Continuing our simulations of the 11-ridge array, we calculated the electric-field amplitude (normalized to the amplitude of the incident laser beam) distribution near the surface for the maximum SPP excitation (Fig. 3). Unidirectional excitation of the left propagating SPP is clearly displayed in this distribution showing also that the electric field is indeed enhanced by $\sim$1.5–1.9 times on the left side of the array due to the SPP excitation. One should keep in mind that, upon direct illumination of a smooth metal surface, the field at the surface is rather small due to the reflectivity being close to -1. In this respect, the obtained field enhancement is quite an achievement and very promising for sensing applications, since the enhanced (propagating) field covers a large surface area [Fig. 1(c)] thus allowing the interrogation of a considerable amount of a test substance.

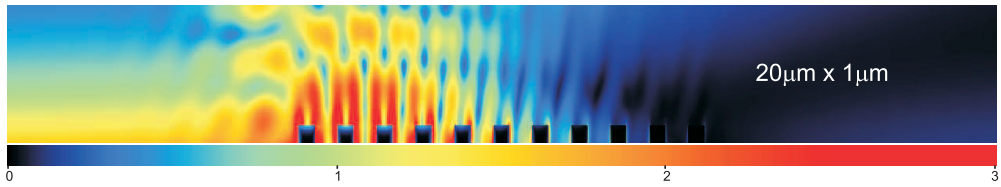

Fig. 3. Numerical results for electric-field amplitude distribution near the 11-ridge array illuminated under the optimal conditions for SPP excitation. The field values are normalized to the amplitude of the incident field.

For the purpose of achieving *local* field enhancement (within a well-defined surface area) one can employ focusing of the excited SPP beam, for example by a parabolic chain of nanoparticles [12] creating thereby an even stronger electric field. Alternatively, the excited beam can be shaped from the very beginning as a converging one [13, 14] by using a circularly curved ridge array (Fig. 4). Apparently, for such an array to produce a tightly focused spot, it should be entirely covered with an incident laser beam exciting the converging SPP beam. This requires

an increased laser-beam diameter, which leads to a decreased SPP excitation efficiency partially because of the incident field polarization no longer being strictly perpendicular to the ridges. In this case, we measured the efficiency to be $\eta = 0.06 \pm 0.01$ for the array with an internal radius of curvature $R = 28.8$ μm. Comparing the lateral sizes of the focused SPP beam [$\sim$ 1.7 μm, Fig. 4(b)] and the divergent one [$\sim$ 12 μm, Fig. 1(c)] at the same distance ($R \approx 30$ μm) from the excitation place, one can see that the focusing effect is practically balanced with the efficiency decrease with respect to the achieved field enhancement. It is though expected that the optimum parameters for curved and straight ridge arrays might be quite different. Reducing the array's radius of curvature helps to decrease SPP propagation loss [Fig. 4(c,d)], but somewhat decreases the efficiency of excitation because of the smaller array area. This can provide some flexibility in designing of structures for practical applications. Note that curved ridge arrays can also be found useful for efficient coupling of a SPP beam into waveguiding structures.

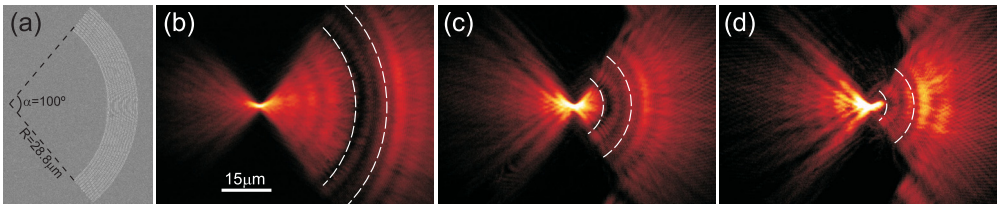

Fig. 4. (a) SEM image of a circularly curved 11-ridge array. (b–d) LRM images of SPP excitation and focusing at the laser wavelength of 816 nm. An approximate position of the arrays is shown with the dashed curves. Internal radii of curvature of the arrays are (b) 28.8 μm, (c) 9.6 μm, and (d) 4.8 μm.

In summary, we demonstrated an efficient unidirectional SPP excitation with a focused laser beam achieving the SPP excitation efficiency of 0.45 ± 0.06 at the resonant wavelength of 816 nm. We conducted numerical simulations accounting for the experimental results and estimated the field enhancement obtained near the gold surface due to the SPP excitation. Finally, we demonstrated curved ridge SPP couplers that tightly focus SPPs upon excitation. The presented approach to generation of enhanced electric fields may be an alternative to localized plasmons for achieving enhanced fluorescence and Raman scattering [15].

This work was supported by the Danish Technical Research Council (Contract No. 26-04-0158), the European Network of Excellence, Plasmo-Nano-Devices (Contract No. FP6-2002-IST-1-507879), the Spanish MCyT (Projects No. MAT2005-06608-C02, No. AP2005-55-185, and Consolider project "Nanolight.es"), and the NABIIT project (Contract No. 2106-05-033 from the Danish Research Agency).

Part III

Concluding remarks

Summary

The main purpose of this PhD study was to explore the possibilities of nanostructured metal surfaces to manipulate surface plasmons (SPs), particularly to investigate configurations for efficient light-plasmon conversion, develop structures for SP beam waveguiding, refracting, focusing, as well as enhancing incident electromagnetic field by means of SPs. All the considered components might be found useful in routing of SPs from the point of their efficient excitation towards field-enhancing structures or between any other plasmon-based devices in order to avoid multiple inter-conversions between light and SPs, opening hereby exciting perspectives for practical applications within integrated plasmonics as well as in bio- and molecular sensing, e.g. via the development of lab-on-chip concept.

Following a short introduction to the experimental techniques exploited in this PhD project — scanning near-field optical microscopy (SNOM) and leakage-radiation microscopy (LRM), — various metal nanostructures are investigated in Part II with the view to generate, guide, focus, and manipulate in other ways with SPs. Thus, in Chapter 1, propagation and interaction of SPs excited in the wavelength range 700–860 nm with periodic triangular arrays of gold bumps placed on a gold-film surface are investigated using a collection near-field microscope. The inhibition of SP propagation into the arrays within a certain wavelength range, i.e., the band-gap effect, is demonstrated. SP propagation along a 30° bent channel obtained by an adiabatic rotation of the periodic array of scatterers is also shown. Numerical simulations using the Lippmann-Schwinger integral equation method and performed by Thomas Søndergaard are found to be in reasonable agreement with the experimental results.

Chapter 2 demonstrates focusing of SP beams with parabolic chains of gold nanoparticles fabricated on thin gold films. SP focusing with different parabolic chains is investigated in the wavelength range of 700–860 nm. Mapping of SP fields is accomplished by making use of LRM, demonstrating robust and efficient SP focusing into submicron spots. Numerical simulations based on the Green's

tensor formalism, performed by Andrey B. Evlyukhin, show very good agreement with the experimental results, suggesting the usage of elliptical corrections for parabolic structures to improve their focusing of slightly divergent SP beams.

Chapter 3 deals with refraction of SPs by various structures formed by a 100-nm-period square lattice of gold nanoparticles on top of a gold film. SP refraction by a triangular-shaped nanoparticle array indicates that the SP effective refractive index increases inside the array by a factor of ~ 1.08 (for the wavelength 800 nm) with respect to the SP index at a flat surface. Observations of SP focusing and deflection by circularly shaped areas as well as SP waveguiding inside rectangular arrays are consistent with the SP index increase deduced from the SP refraction by triangular arrays. The SP refractive index is found to decrease slightly for longer wavelengths within the wavelength range of 700–860 nm. Modeling based on the Green's tensor formalism, performed by Andrey B. Evlyukhin, is in a good agreement with the experimental results, opening the possibility to design nanoparticle arrays for specific applications requiring in-plane SP manipulation.

A novel back-side slit-illumination method of SP excitation that incorporates a periodic array of grooves carved into the front side of a thick metal film is comprehensively investigated in Chapter 4. Bragg reflection enhances the propagation of SPs away from the array, enabling them to be unidirectionally launched from, and focused to, a localized point.

Chapter 5 presents experimental investigations of efficiency of local SP excitation on gold ridges of rectangular profile positioned on a gold film. The excitation is accomplished by illuminating the metal surface normally with a focused laser beam. Wavelength dependence and dependence of the efficiency on geometrical parameters of ridges are examined. Using LRM, the efficiency of 20% is demonstrated experimentally. Numerical simulations (performed by collaborators in Spain) based on Green's tensor approach are in good agreement with the experiment and allow suggesting an optimization of parameters for improving the efficiency of SP excitation.

Finally, Chapter 6 presents characterization of the efficiency of unidirectional surface-plasmon excitation with periodic (800 nm) arrays of 130-nm-high and 330-nm-wide gold ridges on a thin gold film illuminated with a focused (5-μm-wide) laser beam. It is shown, that at the resonant wavelength of 816 nm the excitation efficiency of > 0.4 can be obtained with ≥ 5 ridges by adjusting the beam position. Numerical simulations (produced by a Spanish group of collaborators), account for the experimental results and reveal the electric-field enhancement achieved near the gold surface.

Bibliography

References

[1] R. P. Feynman, "There's plenty of room at the bottom," *Engineering and Science (CalTech)* **23,** 22–36 (1960).

[2] N. Taniguchi, "On the basic concept of 'nano-technology'," *Proc. Intl. Conf. Prod. Eng. Tokyo, Part II,* Japan Society of Precision Engineering (1974).

[3] G. E. Moore, "Cramming more components onto integrated circuits," *Electronics (Intel)* **38** (1965).

[4] R. Chau, J. Brask, S. Datta, G. Dewey, M. Doczy, B. Doyle, J. Kavalieros, B. Jin, M. Metz, A. Majumdar, and M. Radosavljevic, "Application of high-κ gate dielectrics and metal gate electrodes to enable silicon and non-silicon logic nanotechnology," *Microelectronic Engineering* **80,** 1–6 (2005).

[5] R. H. Dennard, F. H. Gaensslen, H. N. Yu, V. L. Rideout, E. Bassous, and A. R. LeBlanc, "Design of ion-implanted MOSFETs with very small physical dimensions," *IEEE J. Solid-State Circuits* **SC-9,** 256–268 (1974).

[6] R. W. Keyes, "Fundamental limits of silicon technology," *Proc. IEEE* **89,** 227–239 (2001).

[7] J. D. Meindl, Q. Chen, and J. A. Davis, "Limits on silicon nanoelectronics for terascale integration," *Science* **293,** 2044–2049 (2001).

[8] Y. Taur, "CMOS design near the limit of scaling," *IBM J. Res. Dev.* **46,** 213–222 (2002).

[9] Internet resource at `http://www.itrs.net/Links/2007ITRS/Home2007.htm`

[10] V. V. Zhirnov, R. K. Cavin, J. A. Hutchby, and G. I. Bourianoff, "Limits to binary logic switch scaling — a Gedanken model," *Proc. IEEE* **91,** 1934–1939 (2003).

[11] S. E. Miller "Integrated optics: an introduction," *Bell Syst. Tech. J.* **48,** 2059–2069 (1969).

[12] J. D. Joannopoulos, P. R. Villeneuve, and S. Fan, "Photonic crystals: putting a new twist on light," *Nature* **386,** 143–149 (1997).

[13] International Telecommunication Union standard ITU-T G.694.1 (2002).

[14] M. Maier, *Optical switching networks* (Cambridge University Press, 2008).

[15] I. P. Kaminow, T. Li, and A. E. Willner (eds.), *Optical fiber telecommunications B: Systems and networks* (Academic Press, 2008).

[16] R. Zia, J. A. Schuller, A. Chandran, and M. L. Brongersma, "Plasmonics: the next chip-scale technology," *Mater. Today* **9,** 20–27 (2006).

[17] R. H. Ritchie, "Plasma losses by fast electrons in thin films," *Phys. Rev.* **106,** 874–881 (1957).

[18] C. J. Powell and J. B. Swan, "Effect of oxidation on the characteristic loss spectra of aluminium and magnesium," *Phys. Rev.* **118,** 640–643 (1960).

[19] W. L. Barnes, A. Dereux, and T. W. Ebbesen, "Surface plasmon subwavelength optics," *Nature (London)* **424,** 824–830 (2003).

[20] S. A. Maier and H. A. Atwater, "Plasmonics: Localization and guiding of electromagnetic energy in metal/dielectric structures," *J. Appl. Phys.* **98,** 1–10 (2005).

[21] J. Lambe and S. L. McCarthy, "Light emission from inelastic electron tunneling," *Phys. Rev. Lett.* **37,** 923–925 (1976).

[22] K. Takeuchi, Y. Uehara, S. Ushioda, and S. Morita, "Prism-coupled light emission from a scanning tunneling microscope," *J. Vac. Sci. Technol. B* **9,** 557–560 (1991).

[23] Y. De Wilde, F. Formanek, R. Carminati, B. Gralak, P.-A. Lemoine, K. Joulain, J.-P. Mulet, Y. Chen, and J.-J. Greffet, "Thermal radiation scanning tunnelling microscopy," *Nature (London)* **444,** 740–743 (2006).

[24] S. A. Maier, *Plasmonics: Fundamentals and applications* (Springer, New York, 2007).

[25] E. N. Economou, "Surface plasmons in thin films," *Phys. Rev.* **182,** 539–554 (1969).

[26] R. Zia, M. D. Selker, P. B. Catrysse, and M. L. Brongersma, "Geometries and materials for subwavelength surface plasmon modes," *J. Opt. Soc. Am. A* **21,** 2442–2446 (2004).

[27] T. Søndergaard and S. I. Bozhevolnyi, "Slow-plasmon resonant nanostructures: Scattering and field enhancements," *Phys. Rev. B* **75,** 073402 (2007).

[28] S. A. Maier, M. L. Brongersma, P. G. Kik, S. Meltzer, A. A. G. Requicha, and H. A. Atwater, "Plasmonics — a route to nanoscale optical devices," *Adv. Mater.* **13,** 1501–1505 (2001).

[29] S. Lal, S. Link, and N. J. Halas, "Nano-optics from sensing to waveguiding," *Nature Photonics* **1,** 641–648 (2007).

[30] K. A. Willets and R. P. Van Duyne, "Localized surface plasmon resonance spectroscopy and sensing," *Annu. Rev. Phys. Chem.* **58,** 267–297 (2007).

[31] J. N. Anker, W. P. Hall, O. Lyandres, N. C. Shah, J. Zhao, and R. P. Van Duyne, "Biosensing with plasmonic nanosensors," *Nature Mat.* **7,** 442–453 (2008).

[32] H. Raether, *Surface plasmons* (Springer, Berlin, 1988).

[33] D. Courjon and C. Bainier, "Near-field microscopy and near-field optics," *Rep. Prog. Phys.* **57,** 989–1028 (1994).

[34] D. W. Pohl, "Optics at the nanometer scale," *Phil. Trans. R. Soc. Lond. A* **362,** 701–717 (2004).

[35] D. Courjon, *Near-field microscopy and near-field optics* (Imperial College Press, London, 2003).

[36] J. W. Goodman, *Introduction to Fourier Optics* (McGraw-Hill, New York, 1996).

[37] J. C. Weeber, F. de Fornel, and J. P. Goudonnet, "Numerical study of the tip-sample interaction in the photon scanning tunneling microscope," *Opt. Commun.* **126,** 285–292 (1996).

[38] D. P. Tsai, Z. Wang, and M. Moskovits, "Estimating the effective optical aperture of a tapered fiber probe in PSTM imaging," in *Scanning Probe Microscopies II*, *Proc. SPIE* **1855,** 93–104 (1993).

[39] A. J. Meixner, M. A. Bopp, and G. Tarrack, "Direct measurement of standing evanescent waves with a photon-scanning tunneling microscope," *Appl. Opt.* **33,** 7995–8000 (1994).

[40] D. Van Labeke and D. Barchiesi, "Probes for scanning tunneling optical microscopy: A theoretical comparison," *J. Opt. Soc. Am. A* **10,** 2193–2201 (1993).

[41] R. Carminati and J.-J. Greffet, "2-Dimensional numerical-simulation of the photon scanning tunneling microscope — concept of transfer-function," *Opt. Commun.* **116,** 316–321 (1995).

[42] J. C. Weeber, E. Bourillot, A. Dereux, J. P. Goudonnet, Y. Chen, and C. Girard, "Observation of light confinement effects with a near-field optical microscope," *Phys. Rev. Lett.* **77,** 5332–5335 (1996).

[43] J. R. Krenn, A. Dereux, J. C. Weeber, E. Bourillot, Y. Lacroute, J. P. Goudonnet, G. Schider, W. Gotschy, A. Leitner, F. R. Aussenegg, and C. Girard, "Squeezing the optical near-field zone by plasmon coupling of metallic nanoparticles," *Phys. Rev. Lett.* **82,** 2590–2593 (1999).

[44] S. I. Bozhevolnyi and V. Coello, "Elastic scattering of surface plasmon polaritons: Modeling and experiment," *Phys. Rev. B* **58,** 10899–10910 (1998).

[45] A. G. Choo, H. E. Jackson, U. Thiel, G. N. De Brabander, and J. T. Boyd, "Near-field measurements of optical channel wave-guides and directional-couplers," *Appl. Phys. Lett.* **65,** 947–949 (1994).

[46] S. Bourzeix, J. M. Moison, F. Mignard, F. Barthe, A. C. Boccara, C. Licoppe, B. Mersali, M. Allovon, and A. Bruno, "Near-field optical imaging of light propagation in semiconductor waveguide structures," *Appl. Phys. Lett.* **73,** 1035–1037 (1998).

[47] S. I. Bozhevolnyi, B. Vohnsen, E. A. Bozhevolnaya, and S. Berntsen, "Self-consistent model for photon scanning tunneling microscopy: Implications for image formation and light scattering near a phase-conjugating mirror," *J. Opt. Soc. Am. A* **13,** 2381–2392 (1996).

[48] B. Vohnsen and S. I. Bozhevolnyi, "Optical characterization of probes for photon scanning tunnelling microscopy," *J. Microsc.* **194,** 311–316 (1999).

[49] S. I. Bozhevolnyi, B. Vohnsen, and E. A. Bozhevolnaya, "Transfer functions in collection scanning near-field optical microscopy," *Opt. Commun.* **172,** 171–179 (1999).

[50] J.-J. Greffet and R. Carminati, "Image formation in near-field optics," *Prog. Surf. Sci.* **56,** 133–237 (1997).

[51] I. P. Radko, S. I. Bozhevolnyi, and N. Gregersen, "Transfer function and near-field detection of evanescent waves," *Appl. Opt.* **45,** 4054–4061 (2006).

[52] L. Novotny, D. W. Pohl, and P. Regli, "Light propagation through nanometer-sized structures: The two-dimensional-aperture scanning near-field optical microscope", *J. Opt. Soc. Am. A* **11,** 1768–1779 (1994).

[53] B. Hecht, H. Bielefeldt, D. W. Pohl, L. Novotny, and H. Heinzelmann, "Influence of detection conditions on near-field optical imaging," *J. Appl. Phys.* **84,** 5873–5882 (1998).

[54] S. I. Bozhevolnyi, V. A. Markel, V. Coello, W. Kim, and V. M. Shalaev, "Direct observation of lacalized excitations on rough nanostructured surfaces," *Phys. Rev. B* **58,** 11441–11448 (1998).

[55] A. Nesci, R. Dändliker, M. Salt, and H. P. Herzig, "Measuring amplitude and phase distribution of fields generated by gratings with sub-wavelength resolution," *Opt. Commun.* **205,** 229–238 (2002).

[56] T. Grosjean and D. Courjon, "Polarization filtering induced by imaging systems: Effect on image structure," *Phys. Rev. E* **67,** 046611 (2003).

[57] S.I. Bozhevolnyi, M. Xiao, and O. Keller, "External-reflection near-field optical microscope with cross-polarized detection," *Appl. Opt.* **33**, 876–880 (1994).

[58] A. Roberts, E. Ampem-Lassen, A. Barty, K.A. Nugent, G.W. Baxter, N.M. Dragomir, and S.T. Huntington, "Refractive-index profiling of optical fibers with axial symmetry by use of quantitative phase microscopy," *Opt. Lett.* **27**, 2061–2063 (2002).

[59] S.I. Bozhevolnyi, O. Keller, and M. Xiao, "Control of the tip-surface distance in near-field optical microscopy," *Appl. Opt.* **32**, 4864–4868 (1993).

[60] H. Ditlbacher, J. R. Krenn, N. Felidj, B. Lamprecht, G. Schider, M. Salerno, A. Leitner, and F. R. Aussenegg, "Fluorescence imaging of surface plasmon fields," *Appl. Phys. Lett.* **80,** 404–406 (2002).

[61] F. López-Tejeira, S. G. Rodrigo, L. Martín-Moreno, F. J. García-Vidal, E. Devaux, J. Dintinger, T. W. Ebbesen, J. R. Krenn, I. P. Radko, S. I. Bozhevolnyi, M. U. González, J.-C. Weeber, and A. Dereux, "Modulation of surface plasmon coupling-in by one-dimensional surface corrugation," *New J. Phys.* **10,** 033035 (2008).

[62] B. Hecht, H. Bielefeldt, L. Novotny, Y. Inouye, and D. W. Pohl, "Local excitation, scattering, and interference of surface plasmons," *Phys. Rev. Lett.* **77,** 1889–1892 (1996).

[63] H. Ditlbacher, J. R. Krenn, A. Hohenau, A. Leitner, and F. R. Aussenegg, "Efficiency of local light-plasmon coupling," *Appl. Phys. Lett.* **83,** 3665–3667 (2003).

[64] E. Kretschmann, "Die Bestimmung optischer Konstanten von Metallen durch Anregung von Oberflächenplasmaschwingungen," *Z. Physik* **241,** 313–324 (1971).

[65] E. D. Palik, *Handbook of Optical Constants of Solids* (Academic, New York, 1985).

[66] P. B. Johnson and R. W. Christy, "Optical constants of the noble metals," *Phys. Rev. B* **6,** 4370–4379 (1972).

[67] U. Schröder, "Der einfluss dünner metallischer deckschichten auf die dispersion von oberflächenplasmaschwingungen in gold-silber-schichtsystemen," *Surf. Sci.* **102,** 118–130 (1981).

List of publications

Articles in peer-reviewed journals

1: I. P. Radko, V. S. Volkov, S. I. Bozhevolnyi, J. Henningsen, and J. Pedersen, "Near-field mapping of surface refractive-index distributions," *Laser Phys. Lett.* **2,** No.9, 440–444 (2005).

2: I. P. Radko and S. I. Bozhevolnyi, "Near-field detection of evanescent waves," *Phys. Stat. Sol.* **2,** No.12, 4101–4105 (2005).

3: I. P. Radko, T. Søndergaard, and S. I. Bozhevolnyi, "Adiabatic bends in surface plasmon polariton band gap structures," *Opt. Express* **14,** No.9, 4107–4114 (2006).

4: C. Reinhardt, S. Passinger, B. N. Chichkov, C. Marquart, I. P. Radko, and S. I. Bozhevolnyi, "Laser-fabricated dielectric optical components for surface plasmon polaritons," *Opt. Lett.* **31,** No.9, 1307–1309 (2006).

5: I. P. Radko, S. I. Bozhevolnyi, and N. Gregersen, "Transfer function and near-field detection of evanescent waves," *Appl. Opt.* **45,** No.17, 4054–4061 (2006).

6: F. López-Tejeira, S. G. Rodrigo, L. Martín-Moreno, F. J. García-Vidal, E. Devaux, T. W. Ebbesen, J. R. Krenn, I. P. Radko, S. I. Bozhevolnyi, M. U. González, J.-C. Weeber, and A. Dereux, "Efficient unidirectional nanoslit couplers for surface plasmons," *Nature Physics* **3,** 324–328 (2007).

7: I. P. Radko, S. I. Bozhevolnyi, A. B. Evlyukhin, and A. Boltasseva, "Surface plasmon polariton beam focusing with parabolic nanoparticle chains," *Opt. Express* **15,** No.11, 6576–6582 (2007).

8: J. Beermann, I. P. Radko, A. Boltasseva, and S. I. Bozhevolnyi, "Localized field enhancements in fractal shaped periodic metal nanostructures," *Opt. Express* **15,** No.23, 15234–15241 (2007).

9: I. P. Radko, A. B. Evlyukhin, A. Boltasseva, and S. I. Bozhevolnyi, "Refracting surface plasmon polaritons with nanoparticle arrays," *Opt. Express* **16,** No.6, 3924–3930 (2008).

10: F. López-Tejeira, S. G. Rodrigo, L. Martín-Moreno, F. J. García-Vidal, E. Devaux, J. Dintinger, T. W. Ebbesen, J. R. Krenn, I. P. Radko, S. I. Bozhevolnyi, M. U. González, J.-C. Weeber, and A. Dereux, "Modulation of surface plasmon coupling-in by one-dimensional surface corrugation," *New J. Phys.* **10,** 033035 (2008).

11: I. P. Radko, S. I. Bozhevolnyi, G. Brucoli, L. Martín-Moreno, F. J. García-Vidal, and A. Boltasseva, "Efficiency of local surface plasmon polariton excitation on ridges," *Phys. Rev. B* **78,** 115115 (2008).

12: I. P. Radko, V. S. Volkov, J. Beermann, A. B. Evlyukhin, T. Søndergaard, A. Boltasseva, and S. I. Bozhevolnyi, "Plasmonic metasurfaces for waveguiding and field enhancement," *Laser & Photon. Rev.,* DOI: 10.1002/lpor.200810071, published online (2009).

13: I. P. Radko, S. I. Bozhevolnyi, G. Brucoli, L. Martín-Moreno, F. J. García-Vidal, and A. Boltasseva, "Efficient unidirectional ridge excitation of surface plasmons," *Opt. Express* **17,** No.9, 7228–7232 (2009).

Miscellaneous

1: I. P. Radko, V. S. Volkov, S. I. Bozhevolnyi, J. Henningsen, and J. Pedersen, "Mapping of surface refractive-index distribution by reflection SNOM," in *Optical Metrology 2005,* H. Ottevaere, P. DeWolf, and D. S. Wiersma, eds., *Proc. SPIE* **5858,** 57–63 (2005).

2: I. P. Radko, V. S. Volkov, S. I. Bozhevolnyi, J. Henningsen, J. Pedersen, "High-resolution mapping of surface refractive-index distributions," *DOPSNYT* **1,** 15–19 (2006).

3: I. P. Radko, S. I. Bozhevolnyi, G. Brucoli, L. Martín-Moreno, F. J. García-Vidal, and A. Boltasseva, "Efficiency of local surface plasmon polariton excitation on ridges," in *Nanophotonics II,* D. L. Andrews, J.-M. Nunzi, and A. Ostendorf, eds., *Proc. SPIE* **6988,** 69880Q-1 (2008).

Presentations

1: I. P. Radko and S. I. Bozhevolnyi, "Near-field detection of evanescent waves". Poster presented at the 6th International Conference on *Optics of Surfaces and Interfaces (OSI-VI),* Aalborg, Denmark (2005).

2: I. P. Radko, V. S. Volkov, S. I. Bozhevolnyi, J. Henningsen, J. Pedersen, "Surface refractive index mapping by use of near-field optical microscopy". Talk given at the *SPIE International Symposium,* Munich, Germany (2005).

3: I. P. Radko, S. I. Bozhevolnyi, E. Devaux and J. Dintinger, "Surface Plasmon Polaritons excitation through slits," Poster presented at the 5th Research Workshop and Network Council Meeting within *Plasmo-nano-devices Project,* Barcelona, Spain (2006).

4: I. P. Radko and S. I. Bozhevolnyi, "Detection efficiency of near-field probes and transer function". Poster presented at the 9th International Conference on *Near-field Optics (NFO-9),* Lausanne, Switzerland (2006).

5: I. P. Radko, A. Boltasseva, and S. I. Bozhevolnyi, "Surface plasmon beam focusing and splitting by parabolic structures". Poster presented at the 3rd International Conference on *Surface Plasmon Photonics (SPP-3),* Dijon, France (2007).

6: I. P. Radko, A. E. Boltasseva, and S. I. Bozhevolnyi, "Efficient local excitation of surface plasmons". Invited talk given at the *SPIE Photonics Europe,* Strasbourg, France (2008).

7: I. P. Radko, A. E. Boltasseva, and S. I. Bozhevolnyi, "Plasmon based on-chip nanosensing". Talk given at the Second Workshop on *Nanobased Sensors,* Odense, Denmark (2008).

8: I. P. Radko, A. E. Boltasseva, and S. I. Bozhevolnyi, "Refracting surface plasmons with nanoparticle arrays". Talk given at the *Quantum Electronics and Laser Science Conference (QELS),* San Jose, USA (2008).

9: I. P. Radko, A. E. Boltasseva, and S. I. Bozhevolnyi, "Local excitation of surface plasmons on ridges". Poster presented at the 7th Research Workshop and Network Council Meeting within *Plasmo-nano-devices Project,* Göteborg, Sweden (2008).

10: I. P. Radko, S. I. Bozhevolnyi, G. Brucoli, L. Martín-Moreno, F. J. García-Vidal, and A. Boltasseva, "High-efficiency local light-plasmon conversion". Poster presented at the 2nd European Topical Meeting on *Nanophotonics and Metamaterials (Nanometa),* Seefeld, Austria (2009).

11: I. P. Radko, A. Boltasseva, and S. I. Bozhevolnyi, "Efficient Local Excitation and Focusing of Surface Plasmons". Poster presented at the *Material Research Society Meeting (MRS),* San Francisco, USA (Spring, 2009).